University of Nevada, Reno

3D-FAST: Three-Dimensional Fourier Analysis of Pavement Structures Under Transient Loading

A dissertation submitted in partial
fulfillment of the requirements for the
degree of Doctor of Philosophy in Civil and
Environmental Engineering

by
Seyed-Farzan Kazemi

Adam J.T. Hand;. Ph.D./Dissertation Advisor
May, 2018

UNIVERSITY OF NEVADA RENO **THE GRADUATE SCHOOL**

We recommend that the dissertation
prepared under our supervision by

Seyed-Farzan Kazemi

entitled

3D-FAST: Three-Dimensional Fourier Analysis of Pavement Structures Under Transient Loading

be accepted in partial fulfillment of the
requirements for the degree of

DOCTOR OF PHILOSOPHY

Adam J.T. Hand, Ph.D., Advisor

Elie Y. Hajj, Ph.D., Committee Member

Peter E. Sebaaly, Ph.D., Committee Member

Raj V. Siddharthan, Ph.D., Committee Member

Wanliang Shan, Ph.D., Graduate School Representative

David W. Zeh, Ph.D., Dean, Graduate School

May, 2018

ABSTRACT

3D-FAST is a finite-layer model to compute pavement mechanical responses under dynamic (i.e., time-variable) non-uniform load of any shape. Surface loads, including vertical load and braking shear loads are discretized into waves propagating in time domain and spatial domains employing three-dimensional (3-D) Fourier transform. This transformation allows 3D-FAST to integrate the frequency-dependent material characterization with the harmonics composing the surface loads. In the model formulation, the main unknowns are displacements, and all other responses (i.e. stresses, strains, velocities and accelerations) are determined based on the displacement field. Layer interface boundary conditions were incorporated into 3D-FAST and may be adjusted to account for interface slippage. The equilibrium equations are set to be satisfied for every wave in the frequency domain for a representative differential element and for each time step. Using inverse Fourier transform, the responses can be obtained at the desired depths for the full spatial domain, generating informative graphical 3-D surface plots animated with time. Some practical applications of 3D-FAST are modelling FWD with any pulse shape and pavement analysis for roughness-induced dynamic loads. The runtime of the model is considerably shorter compared to finite-element methods with no concern regarding mesh identification. The unique formulation of the model also allows for further computational efficiency by incorporation parallel processing into the model. 3D-FAST is a computationally efficient model for computing pavement responses, specifically in combination with mechanistic empirical (M-E) approaches. The

superposition principle represented by Boltzmann's equation can be effectively integrated with 3D-FAST because it simplifies to multiplication in frequency domain. The non-uniform Fourier transform was proposed as a means of reducing computational runtime, however, it should be noted that it introduces some approximation to the results. 3D-FAST was verified and validated, and a sample application was demonstrated. The 3D-FAST verification process was performed by investigating rheological model, specifically, Kelvin, Maxwell, and Burger models. The results obtained by 3D-FAST were compared to classical solutions derived for strain amplitude and phase angle of these models and were matched very well. 3D-FAST results were validated by one of the experiments conducted at the full-scale Box facility at the University of Nevada, Reno. The measured deflections from LVDTs and stresses from pressure cells were compared with 3D-FAST results in terms of response pulse shape and peak value. The comparison revealed a descent match between 3D-FAST results and data collected by the experiment instrumentation. As for the 3D-FAST application, the roughness-induced vehicle dynamic loading was investigated for a sample road profile. The dynamic load was obtained using quarter-car simulation, and was used as the load input for 3D-FAST. A variety of response types were computed for this example at different locations within pavement structure.

This dissertation is

dedicated to my beloved

family for their support

and encouragement.

ACKNOWLEDGMENTS

This research was certainly impossible without the support I have received by all of the members at the Pavement Engineering & Science (PES) program at the University of Nevada, Reno. I would like to deeply appreciate all the efforts of my advisor, Dr. Adam J.T. Hand, for his leadership, patience, and high moral qualities, as well as his advice during my PhD, which has been always the guide for my way.

I like to appreciate my co-advisor's efforts, Dr. Elie Y. Hajj, who has been always a role model for being a hard worker, and a quality researcher. Dr. Hajj was always available despite his busy schedule, and I continuously took advantage of his problem solving skills in my research. I am also very glad that I was working with him on other research projects that made my background very diverse. I appreciate him for giving me this opportunity.

I would also like to thank Dr. Peter E. Sebaaly for his support as the director of the PES program, and as a helpful and passionate person, particularly in challenging times during my research.

I have to highly appreciate Dr. Raj V. Siddharthan for his time and knowledge. Not only was this research founded on his previous work but also he was a very motivational person for me and I always benefited from his tremendous genius.

I appreciate Dr. Wanliang Shan's efforts for being on my committee. He gave me a desecent impression about continuum mechanics, and I effectively applied that to my research.

My special thanks to all of my colleagues and friends at PES program: Dario, Mohamed, Rami, Hadi, Johnny, Sarah, Alberto, Federico, Pratha, Mateo, Christopher, Elise, Habtamu, Sara, Lauren, Visctor, Jorge, JeyaKaran, Sandeep, Roshan and so on. I would like to also thank Murugaiyah Piratheepan, our lab manager, for always being a good help.

Last but not least, I would like to sincerely thank my parents and my younger brother for their endless support, motivation, encouragement, and love. This dissertation is dedicated to them!

TABLE OF CONTENTS

LIST OF TABLES

LIST OF FIGURES

CHAPTER 1 INTRODUCTION

Appropriate, timely, and precise estimation of pavement mechanical responses is of significance importance for modeling pavement behavior and predicting pavement performance. Calculations associated with these estimations are complex depending on different environmental and structural factors contributing to the problem of interest. With the evolution of mechanistic-empirical (ME) pavement design methods, the reliable estimation of pavement mechanical responses (i.e., stresses, strains and displacements) has become crucial in order to predict pavement performance. For instance, the mechanistic-empirical pavement design guide (MEPDG) employs mechanical responses, specifically strains, to predict pavement fatigue cracking and rutting life as performance measures (NCHRP, 2004). Therefore, any deviations in computing pavement responses adversely influences pavement performance prediction.

1.1 Pavement Mechanical Responses

Reliable estimation of pavement responses is of significant importance, especially when pavement mechanistic-empirical (M-E) models are to be used. Typically, M-E models use pavement responses to predict distresses such as fatigue cracking, rutting, and thermal cracking (DAGHIGHI & NAHVI, 2014; Wang, Keshavarzi, & Kim, 2018; Zhu, Dave, Rahbar-Rastegar, Daniel, & Zofka, 2017). These distresses adversely affect pavement performance. So a better estimation of pavement responses leads to better prediction of pavement distresses. In M-E models, pavement distresses are correlated to one or more pavement responses. For instance, fatigue cracking is correlated with tensile

strain at the bottom of asphalt concrete (AC) layer in MEPDG (NCHRP, 2004). Therefore, reliable estimation of pavement responses significantly contributes to realistic prediction of pavement performance.

In every ME design method, there are four critical factors influencing the results: traffic load levels, material characteristics, pavement structure, and environmental conditions. A pavement mechanical response analysis model should consider these factors and the variability of them in the process of estimating pavement responses (Bozorgzad, 2017; Hand & Epps, 2000). Traffic loads are critical inputs for the response analysis model that are defined by the shape of tire-pavement contact area and pressure amplitude. Many pavement response analysis models consider simplified conditions for traffic loads. However, it is ideal for a response analysis model to simulate actual tire-contact shape and contact stress amplitude as it is more rational. Furthermore, the effect of road surface conditions (i.e., road roughness) on the dynamic-induced tire loads should be considered in the model.

Material characteristics influence pavement responses primarily because of material mechanical behavior (e.g., linear elastic, stress-dependent, or viscoelastic) and associated material properties (Mokhtari & Nejad, 2012; Tirado, Gamez-Rios, Fathi, Mazari, & Nazarian, 2017). In flexible pavements, asphalt concrete (AC) used in the upper layers of the structure has viscoelastic properties, meaning that these properties are predominantly a function of temperature and loading frequency (Bazzaz, Darabi, Little, & Garg, 2018; Nemati & Dave, 2017).

Environmental conditions may influence pavement performance by means of

moisture diffusion in the form of water or evaporation, leading to moisture damage (Bozorgzad, Kazemi, & Moghadas Nejad, 2018; Bozorgzad, Kazemi, & Nejad, 2018). However, the environmental conditions (specifically air temperature, wind speed, and solar radiation) influence pavement temperature, which in turn influences the modulus of viscoelastic layers such as AC (Alavi, Pouranian, & Hajj, 2014; Arabzadeh, Ceylan, Kim, Gopalakrishnan, & Sassani, 2016; Y. H. Huang, 1993). An ideal pavement response analysis model not only should account for material characteristics, but also should address the effects of variation in environmental conditions on material properties, and subsequent computed responses (You, Kim, Rami, & Little, 2018).

In recent years, the operation of overweight (OW) vehicles and superheavy loads (SHLs) has increased substantially, leading to an increase in pavement damage and potential of premature failure (D. Batioja-Alvarez, Kazemi, Hajj, Hand, & Siddharthan; Hajj et al., 2018). According to U.S. Federal Government regulations, OW vehicles are defined as vehicles with a gross vehicle weight (GVW) between 80,000 lb and 250,000 lb (FHWA, February 5, 2017). A SHL is typically defined as a load with a GVW of 250,000 lb or higher, which may increase up to a few million pounds. The analysis of OW vehicles and SHLs needs special considerations which is different than the analysis of typical standard vehicles as used in current pavement design procedures. Batioja et al. developed a methodology to estimate pavement damage and its associated costs based on remaining life concept and Monte-Carlo simulations (D. D. Batioja-Alvarez, Kazemi, Hajj, Siddharthan, & Hand, 2018). This methodology uses AC critical responses to predict pavement design life. With respect to SHL, further investigations should be

performed to evaluate specific cases. These investigations may include, but not limited to, bearing capacity analysis, service limit analysis, and slope stability of pavement shoulders. All of these analyses again require specific pavement responses as input. Thus, it is essential to develop a pavement response model that can handle these elevated load levels in order to enhance pavement design process.

In special cases, a flexible pavement may include sloped shoulders, or there may exist buried utilities (e.g., pipes) at a certain depth from the pavement surface. These cases need special attention when a load, specifically a SHL, is expected to move on the pavement. For a pavement with sloped shoulders, shoulder slope stability is critical and needs to be evaluated. To conduct slope stability analysis for pavement shoulders, stress induced by moving vehicles is needed at certain points of the shoulder. Reliable estimation of these stresses leads to a reliable slope stability evaluation. In the special case of buried utilities, stress, strain, and displacement at the wall of buried utilities must be calculated to ensure that the utility does not fail. Furthermore, service limit analysis of a pavement may need vertical surface displacement checks which are an output of a pavement response analysis model. All of these cases reveal the significance of the need for reliable pavement response estimation.

1.2 Problem Statement

Pavement mechanical responses are essential to predict pavement performance and serviceability. For instance, mechanistic-empirical performance predictive models provided by MEPDG use pavement responses to predict pavement cracking and rutting. In another example, vertical surface deflection can be used as a measure of pavement

serviceability. A higher level of reliability in estimating pavement mechanical responses yields to a more reliable pavement performance prediction. This reliability is primarily related to the pavement mechanical model that is being used to estimate pavement mechanical responses. The most common pavement mechanical responses obtained by a response model are stresses (normal and shear), strains (normal and shear), and displacements. The secondary responses that may be of less application are velocities and accelerations. A pavement mechanical response analysis model should be able to estimate these responses considering different factors contributing to estimation of these parameters. As mentioned in the introduction, the main factors contributing to this estimation are traffic load levels, material characteristics, pavement structure, and environmental conditions. The problem to be addressed in this dissertation is defined as developing a framework (pavement mechanical model) to estimate pavement mechanical responses at a high level of reliability for dynamic loads applied at pavement surface so that these responses can be used as inputs for evaluation of pavement performance and serviceability. In the statement of problem, pavement structure is given including layer thicknesses and layer interface bonding conditions (i.e., fully-bonded, partially-bonded, or no bond). Furthermore, material characteristics constituting pavement layers are known (e.g., linear elastic, viscoelastic). The loading conditions is also known, which is generally a dynamic load. The loading conditions should be representative of real pavement loading conditions. Environmental conditions primarily influence responses by affecting pavement temperature, which in turn affects the dynamic modulus of viscoelastic layers, leading to change in pavement responses. The solution of the stated problem should be an estimation of pavement mechanical responses due to dynamic load

including stresses, strains, and deflections at a specific point within the pavement structure, as a function of time.

1.3 Research Motivation and Objectives

The objective of this dissertation was to develop a pavement mechanical model called 3D-FAST: ***3-D***imensional ***F***ourier ***A***nalysis of pavement ***S***tructures under ***T***ransient loading. The primary motivation for developing this model was to develop a model that could accurately analyze pavement responses under dynamic loading (i.e., load that varies with time) in a timely manner. Considering the factors mentioned earlier, this model should be capable of viscoelastic material characterization, as well as modeling axle loads and configurations with any tire-pavement contact shape and pressure distribution. Furthermore, the model was intended to be computationally efficient with shorter runtime compared to conventional counterpart methods (e.g. finite-element) so that it could conveniently be incorporated into ME design methods.

There are different features associated with 3D-FAST. **Figure 1.1** presents these features in a chart format. This chart basically demonstrates different objectives pursued with development of 3D-FAST. The following a summary of these features:

- Loading Conditions: One of the primary objectives of 3D-FAST development was allowing for *dynamic* pavement surface loading. Dynamic load (unlike static load) may vary with time. The variation of load may be either because of the loading protocol such as load applied by a falling-weight deflectometer (FWD), or due to pavement surface irregularities (i.e., pavement roughness)

which lead to dynamic load. 3D-FAST is capable of handling a wide range of loading times that can be as short as impact loads (such as that of FWD) all the way to loads applied by a vehicle travelling at slow speeds. Moreover, 3D-FAST allows for any tire-pavement contact shape which can be non-circular and/or non-uniform. Load representation will be discussed in **Chapter 3** and **Chapter 4**.

- Material Characteristics: One of significant issues with structural modeling of flexible pavements is the material characterization of viscoelastic layers. A viscoelastic layer typically has a deflection that varies with time. Typically, a viscoelastic material keeps deforming with time under constant loading (viscoelastic creep) and will have time-varying displacement characteristics, even if the load is not present (viscoelastic relaxation). In many software packages, viscoelastic layers are characterized as linear elastic for simplicity to reduce model runtime. In 3D-FAST, however, viscoelastic layers are considered using a linear viscoelastic (LVE) material characterization. A master curve can be defined for viscoelastic materials, or if the frequency-dependency of modulus is known (e.g., in forms of closed-form solutions) those can be used to characterize viscoelastic materials. The viscoelastic material characterization is due to the fact that 3D-FAST performs the associated calculations in the frequency domain. More details about viscoelastic material characterization will be provided in **Section 3.4.6** and **Section 4.2.3**.

- Pavement Structure: 3D-FAST is a finite-layer method meaning that it is capable of handling layered structures such as pavements. The robustness of 3D-FAST, in terms of model formulation and runtime, is due to the wave propagation feature of the model that is based on the layered structure assumption. The bonding conditions at layer interfaces can be either fully boded, partially bonded, or un-bonded. The bottom boundary can be rigid (e.g., bedrock) or semi-infinite conditions can be considered.

- Finite-Layer Model: 3D-FAST is a finite-layer model, which uses the concept of wave propagation. The wave propagation concept is based on the wave laws in physics that waves propagate into the pavement structure. While the amplitude of the waves changes as they propagate into the pavement, the frequency remains the same. A three-dimensional Fast Fourier Transform (FFT) was used to decompose pavement surface loads into the waves. More details about the finite-layer model provided in **Section 2.2**. The formulation based on the finite-layer solution is presented in **Chapter 3** (for constant-speed moving load) and **Chapter 4** (for a general dynamic load).

- Computation Runtime: The finite-layer solution for a pavement structure not only leads to valuable modeling features, such as viscoelastic material characterization, but it also allows for further optimization of the model runtime. The reason why this improvement of the model is possible is that waves obtained by FFT can be processed independently, and superposition principle can be used to obtain the desired response(s) from the individual

responses obtained for the waves. Parallel processing is an effective technique for reducing 3D-FAST runtime and can be efficiently integrated into the model since waves defining the load can be analyzed independently. The superposition principle can also be incorporated into the model using convolution integral. Convolution integral is used in the frequency domain calculations as a means of implementing the superposition principle. Details about the computational features of 3D-FAST are presented in **Chapter 5**.

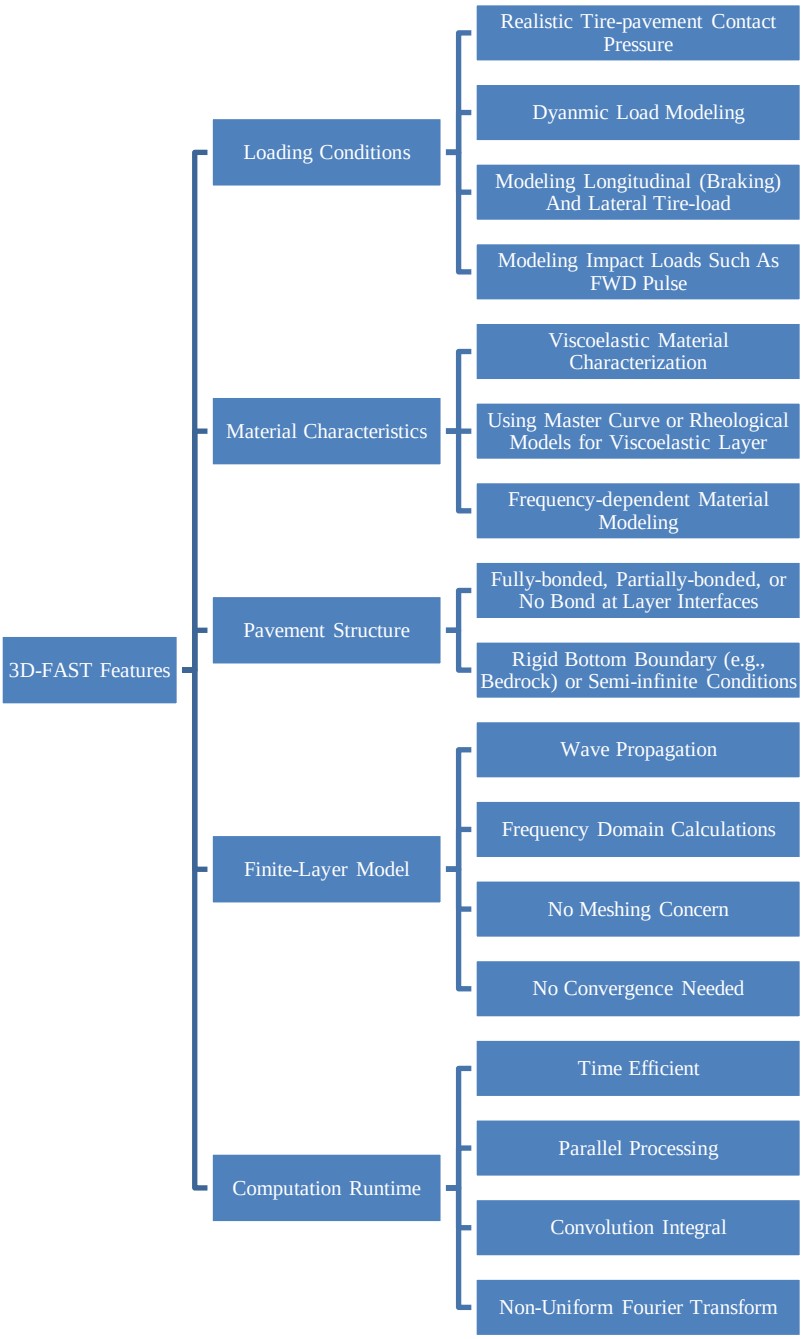

Figure 1.1. Chart. Different features of 3D-FAST.

1.4 Dissertation Outline

In **Chapter 1** the significance of pavement responses is described and 3D-FAST is introduced as a model to estimate pavement mechanical responses under dynamic loading for various loading conditions. Furthermore, the problem is stated along with research motivation and objectives. In **Chapter 2** the background of pavement structural modeling is presented by a brief review of past modeling research works. Finite-layer and finite-element models are presented and compared in this chapter.

Chapter 3 and **Chapter 4** focus on the model formulation. The formulation including load representation, forms of displacements, constitutive equations, boundary conditions, and material characterization are presented in these chapters. **Chapter 3** presents the finite-layer solution for loads moving at constant speed. **Chapter 4** extends the formulation and presents the 3D-FAST formulation applicable to arbitrary dynamic loading.

Chapter 5 summarizes the unique computational features of 3D-FAST including features for reducing model runtime, viscoelastic material characterization, and using inverse Fourier transform to obtain surface plots of responses. **Chapter 6** presents the verification, validation, and application of 3D-FAST using classical closed-form solutions, large-scale testing data, and investigation of roughness-induced dynamic loading, respectively. **Chapter 7** presents a summary of findings and conclusions collected through this dissertation, as well as recommendations for future research.

CHAPTER 2 BACKGROUND

2.1 Introduction

Early efforts to compute pavement responses using mechanistic models dates back to the 1960's (R. V. Siddharthan, Yao, & Sebaaly, 1998). At that timeframe, pavement engineers and researchers started criticizing the idea of using instrumented road test results for pavement design purposes (R. Siddharthan, Hajj, Sebaaly, & Nitharsan, 2015). The primary reason for the criticism was based on the fact that the obtained test results were only valid for the specific conditions under which the test was conducted. Since then, many mechanistic models have been developed and evolved to compute pavement mechanical responses. With simultaneous advances in computer hardware and software technologies, the researchers had the opportunity to develop computer software packages based on these mathematic models. The early pavement analysis software packages such as ELSYM5, WESLEA, and BISAR were based on multi-layered elastic theory (MLET) analysis (Ahlborn, 1972; De Jong, Peutz, & Korswagen, 1972). MLET analysis is based on linear elastic material properties with several simplifying assumptions such as uniform circular loading, weightless layers, and stationary loading conditions. One or more layers of flexible pavements are typically comprised of asphalt concrete (AC) which is a viscoelastic material, with its properties a function of temperature and loading frequency. The frequency dependent characteristics of viscoelastic materials is affected by dynamic loading conditions (e.g., vehicle speed). MLET does not account for viscoelastic material characterization or dynamic loading conditions. With time, models evolved to account for

viscoelastic material characterization. Some software packages addressing viscoelastic material characterization include CIRCLY, KENLAYER, ILLIPAVE, and MICHPAVE (Harichandran, Yeh, & Baladi, 1990; Y. H. Huang, 1993; Thompson, 1982; Wardle, 1977). These software packages address linear viscoelastic (LVE) material characterization, so that they are not able to account for damage.

2.2 Finite-Element vs. Finite-Layer

Today the analysis conducted by most commercial software packages for pavement mechanical response is based on the finite-element method (FEM). In FEM, the pavement layers are broken down into a substantially large number of elements and establishing the equilibrium and continuity equations for each element under given loading conditions. CIRCLY, KENLAYER, and ILLIPAVE are among the software that employ FEM (Y. H. Huang, 1993; Thompson, 1982; Wardle, 1977). Another approach for pavement mechanical response analysis is the finite-layer method. The finite-layer method is based on considering each pavement layer as a separate element by itself. Load is propagated into the pavement structure based on wave propagation concepts. **Figure 2.1** schematically presents the discretizing strategy for finite-element and finite-layer methods. The finite-layer method has the following advantages compared to the finite-element method:

- There is no need for meshing associated with the finite-layer method. With the finite-element method, the meshing strategy is critical. The finer the meshing element size used, the greater the computational time require, but convergence is

possibly guaranteed. If coarser meshing elements are used convergence will be jeopardized, while computational runtime will be decreased. Thus, there is a trade-off between fine meshing and computational runtime. With the finite-layer method, there is no such concern.

- The finite-element method requires high computational capacity due to the large number of unknowns associated with a particular problem. In contrary, the number of unknowns are significantly less with the finite-layer method which translates to more efficient computational runtime.

- Since most of the solving processes in finite-element models are iterative, only a small portion of calculations can be parallelized. Thus, parallel processing is not an effective technique for enhancing finite-element runtime. With the finite-layer method, load is decomposed into a number of waves through Fourier transform and each load can be analyzed independently. Thus, parallel processing can be easily incorporated with finite-layer method resulting in further computational time efficiency.

According to these characteristics, the finite-layer method was employed to develop 3D-FAST. Only a few pavement models have been developed based on the finite-layer method, specifically 3D-Move and Viscowave (ARC, 2013; Lee, 2014). 3D-Move was developed by Siddhartan et al. for analyzing pavement structures under non-stationary and constant speed moving loads (R. V. Siddharthan et al., 1998). A software package called 3D-Move Analysis®, available in the public domain with hundreds of

users worldwide, was developed based on this model (ARC, 2013). The 3D-Move model formulation is based on taking two-dimensional Fourier transform on the surface load and solving equilibrium and continuity equations for the entire pavement system for each and every wave. While many other models are limited to circular uniform tire-pavement contact pressure, there is no such limitation in 3D-Move, so that the contact pressure can be non-circular and/or non-uniform. Viscowave is another finite-layer analysis model which can also account for constant-speed moving load (Lee, 2014). Since Viscowave's formulation employs Hankel transform, it can only handle circular uniform tire-pavement contact pressure. 3D-Move and Viscowave both account for viscoelastic material characterization.

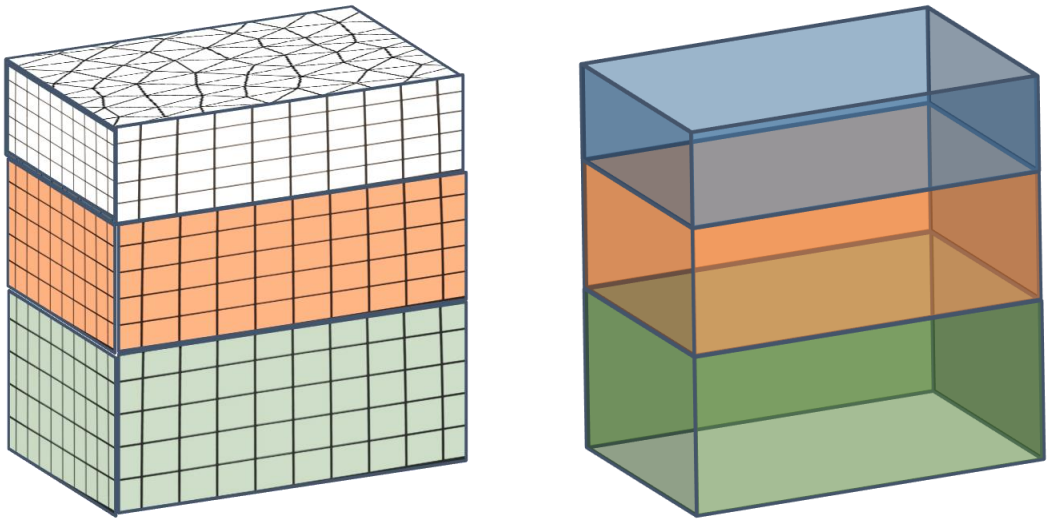

(a) (b)

Figure 2.1. Photo. Schematic presentation of discretization of elements: (a) finite-element method (FEM); and (b) finite-layer method.

3D-FAST is basically an extension to 3D-Move in order to consider dynamic pavement loading conditions. The formulation was modified to include the effect of time as a new Fourier variable, so that the dynamic loading (i.e., load that varies with time) can be considered. While analyzing pavement mechanical responses under dynamic load with 3D-FAST is an enhancement compared to 3D-Move, all the 3D-Move specific features including non-circular, non-uniform tire contact pressure and viscoelastic material characterization are included in 3D-FAST. The 3D-Move formulation is presented in **Chapter 3**. Following that, the 3D-FAST formulation is explained in detail in **Chapter 4**. In these chapters, the model overview including surface load representation, boundary conditions, material characterization, and finite-layer solution are presented. Specific features associated with 3D-FAST are presented in **Chapter 5**. Validation, verification, and application of 3D-FAST is presented in **Chapter 6**.

CHAPTER 3 FINITE-LAYER SOLUTION FOR LAYERED PAVEMENT STRUCTURE: CONSTANT-SPEED MOVING LOAD

As mentioned in the previous chapter, early pavement mechanical analysis models were based on multi-layer linear elastic theory (MLET). For instance, VESYS, BISAR and KENLAYER are among the popular software packages using this approach (De Jong et al., 1972; Y. Huang, 1993; Kenis, 1978). Some of the advantages of these software packages are that they are computationally efficient, and the mathematical formulation behind them is not very complex. Shortcomings of them are the inability in modeling non-circular moving load, lack of capability to model non-uniform stress distribution, limitation of tire contact pressure, non-symmetric interface shear stress, and viscoelastic material characterization. The finite-element method (FEM) has been employed to overcome some of the shortcomings associated with MLET. In this regard, ILLIPAVE, MICHPAVE, etc. were software packages developed based on FEM (Harichandran et al., 1990; Thompson, 1982).

3.1 3D-Move

Although, many of the shortcomings of MLET can be resolved using FEM, other specific issues such as influence of external boundaries, incorporation of damping, and element discretization still remain. Therefore, 3D-Move was developed as a robust pavement response analysis model for evaluation of a specific load case. The original formulation of 3D-Move was developed by Siddharthan et al. (R. V. Siddharthan et al., 1998). 3D-Move uses a finite-layer approach and accounts for viscoelastic material characterization.

Furthermore, the model is capable of analyzing loads of a moving vehicle at constant speed with non-uniform and/or non-circular load on its axles. The ability to model vehicle speed is particularly critical for superheavy load (SHL) vehicles, because they operate at notably low speeds which can cause significant pavement damage. Stresses induced by SHL vehicles are significantly higher than that of standard (or reference) 80,000 lb reference vehicle. This is because superheavy load vehicles typically have higher tire loads and they operate at very slow speeds. As a result, pavement serviceability may be subjected to risk and increased levels of rutting could be anticipated. A direct consequence of lower vehicle speed is lower effective modulus for layers (e.g., surface HMA layer) that exhibit viscoelastic behavior. This results in much larger stresses in the unbound pavement layers that support the surface layer. 3D-Move is capable of computing pavement responses under vehicles moving at constant speed on a specific pavement structure with known material properties.

Surface shear stresses in both horizontal and lateral direction can be modeled independently with 3D-Move with no limitation such as symmetry. This is very important when analysis of interface shear stresses from vehicle breaking are to be investigated. Though not included in the original formulation, 3D-Move formulation allows for providing three-dimensional (3-D) surface plots for a specific pavement response at a desired depth, where the distribution of critical pavement response at that depth is displayed. Additionally, it allows for layer interface conditions such as debonding or slippage can be modeled using 3D-Move. These unique features were added in the newer version of 3D-Move, called 3D-Move ENHANCED. The above-

mentioned features make 3D-Move a robust pavement response analysis model that is ideally appropriate for incorporation with M-E pavement design procedures.

Pavement responses obtained can also be used for further investigation of the pavement load-bearing characteristics. For instance, the bearing capacity of the subgrade layer can be evaluated using the vertical stress at the subgrade level, which is an output of 3D-Move.

3.2 3D-Move Analysis® Software

3D-Move Analysis software was developed at the University of Nevada, Reno based on the formulation developed by Siddharthan et al. (R. V. Siddharthan et al., 1998).The software is available for public use and was a product of the asphalt research consortium (ARC) projects. The core of 3D-Move Analysis® software was initially developed in FORTRAN in 1998. Later, a graphical user interface (GUI) was developed in C and C# programming languages to make 3D-Move Analysis® a stand-alone user-friendly software (El-Desouky, 2003). The most current available software version is 2.1. **Figure 3.1** presents a screenshot of this version of 3D-Move Analysis®. The software has been used by more than 750 users from 50 countries around the globe. **Figure 3.2** illustrates the countries with 3D-Move Analysis® software users (shown in red). 3D-Move Analysis® is capable of analyzing pavement structures under both stationary and constant-speed moving load.

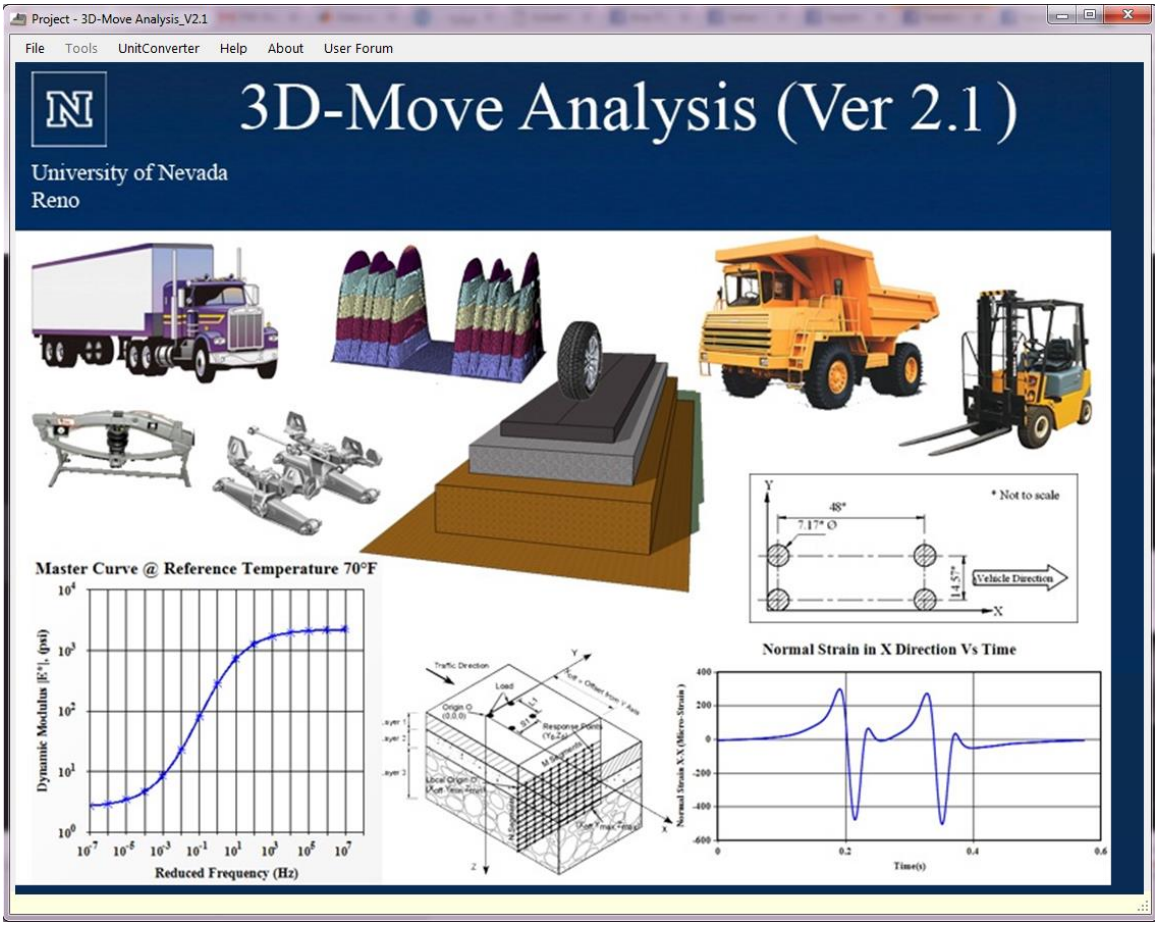

Figure 3.1. Screenshot. Main window of 3D-Move Analysis® software version 2.1.

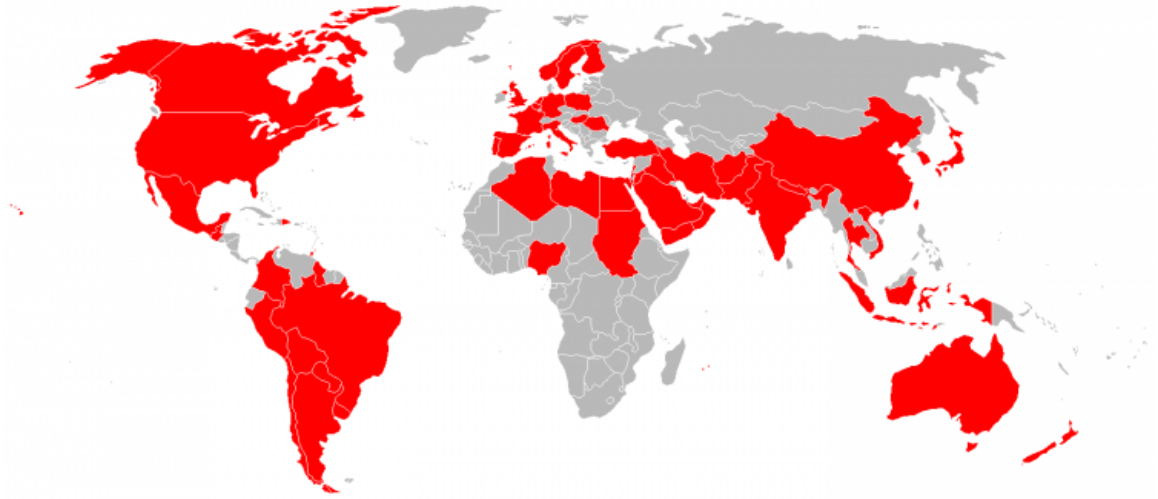

Figure 3.2. Photo. Countries with 3D-Move Analysis ® users (shown in red).

3.3 3D-Move ENHANCED

A newer version of 3D-Move Analysis® was developed to be incorporated with *SuperPACK*, a software designed for superheavy load (SHL) analysis. This newer version of 3D-Move is called **3D-Move ENHANCED.** From a computer programming prospective, the formulation of 3D-Move formulation is complex to be implemented. For instance, the formulation contains two-dimensional forward and inverse Fourier transform, as well as substantial matrix calculations. A number of different computer programming languages were scrutinized to evaluate if they support these features, as well as other features, such as stand-alone execution, graphical user interface, and capability to support convenient connection between SuperPACK components. Mathematical features offered by MATLAB such as forward and inverse Fourier transform and comprehensive support of matrix calculations serve the needs for implementing 3D-Move ENHANCED formulation. Thus, MATLAB was selected because it supports two-dimensional Fourier transform and handles large matrix manipulations very efficiently. Moreover, MATLAB supports GUI programming which was intended to be used by SuperPACK. In addition, one can compile a MATLAB code and publish it as a stand-alone software package.

3D-Move ENHANCED is basically the response analysis engine of SuperPACK and the model is based on the original formulation developed by Siddharthan et al. (R. V. Siddharthan et al., 1998). However, a number of enhancements were incorporated into 3D-Move ENHANCED. They are primarily with respect to method of calculating

responses, interface bond, and runtime improvement. These enhancements are investigated independently in **Section 3.5**.

3D-Move ENHANCED has a number of unique features inherited from its original formulation. It is of significant importance to note that 3D-Move ENHANCED performs all the associated calculations in the frequency domain using fast Fourier transform (FFT) algorithm. For instance, since 3D-Move ENHANCED employs two-dimensional Fourier transform to describe vehicle loading, tire loads can be non-uniform and of any shape. Furthermore, 3D-Move ENHANCED calculations are independent for different Fourier waves. Thus, a parallel processing scheme was incorporated into 3D-Move ENHANCED formulation in order to improve the runtime.(S. F. Kazemi & Shafahi, 2013). Furthermore, viscoelastic materials (e.g., hot-mix asphalt and HMA) could be characterized based on 3D-Move ENHANCED formulation. 3D-Move ENHANCED also considers the influence of pavement temperature and vehicle speed on the modulus of viscoelastic material(s) used in pavement layers that exhibit such characteristics.

3.4 Formulation

The finite-layer approach was employed in 3D-Move Analysis® and 3D-Move ENHANCED formulation (both called 3D-Move in this chapter), which is based on the wave propagation concept. In the finite-layer approach, each layer is modeled as a separate element, as opposed to the finite-element method where each layer is decomposed into many elements. In the finite-layer method, the load is decomposed into many waves represented in the frequency domain. Displacements are considered to be the

primary unknowns in 3D-Move. In finite-layer modeling, it is assumed that displacements have the same frequency as the load for every wave. However, their amplitudes vary within the pavement structure. This is the concept of wave propagation which is central to the finite-layer method. Details about 3D-Move formulation are presented in this section.

3.4.1 Surface Load Representation

A Pavement surface load is represented as a two-dimensional domain in *x*- and *y*-directions. As mentioned earlier, FFT algorithm is applied on the load to transform it to the frequency domain. The *x*-direction is the vehicle travel direction and *y*-direction is the horizontal direction perpendicular to it. **Figure 3.12** schematically shows the coordinates used in the presented formulation.

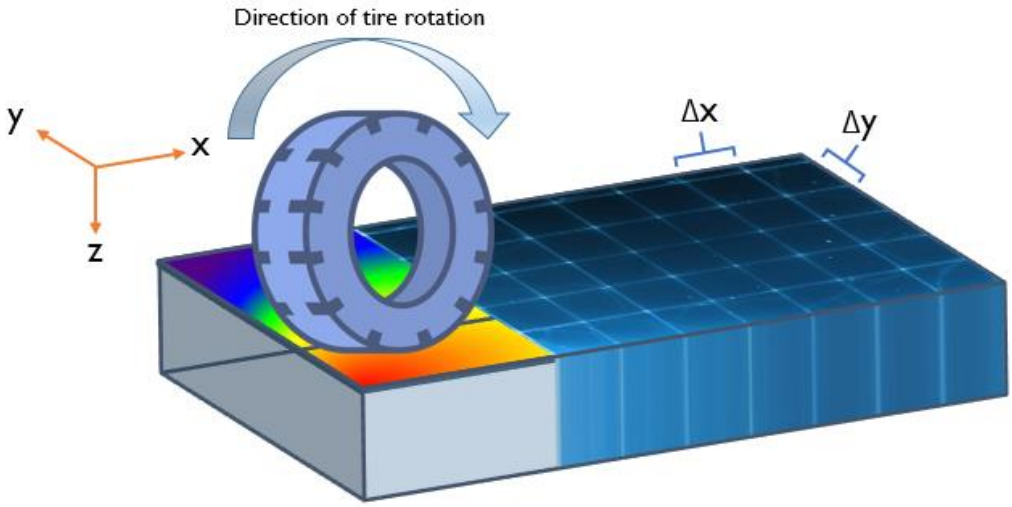

Figure 3.3. Photo. Schematic presentation of tire load and discretization of surface load to be used with Fast Fourier Transform (FFT).

The surface load can be of any shape with any contact stress distribution. Surface load representation would be the equation presented in **Figure 3.4**.

$$p(x,y) = \sum_{m=1}^{M}\sum_{n=1}^{N} A_{mn} e^{i\omega_x x} e^{i\omega_y y}$$

Figure 3.4. Equation. Surface load representation (stationary conditions).

Here, $p(x, y)$ is load stress for a point with coordinate of (x, y), and M and N are the total number of waves in x- and y-direction, respectively. Furthermore, m and n are wave numbers, and ω_x and ω_y are frequencies in the x- and y-directions, respectively. A_{mn} is the Fourier coefficient matrix, which is determined by applying a two-dimensional fast Fourier transform (FFT) algorithm on the load matrix (i.e., $p(x, y)$). Considering the loaded vehicle is travelling at constant speed V toward the x-direction, the modified load representation equation for speed is the equation presented in **Figure 3.5** where t is time.

$$p(x,y) = \sum_{m=1}^{M}\sum_{n=1}^{N} A_{mn} e^{i\omega_x (x-Vt)} e^{i\omega_y y} = \sum_{m=1}^{M}\sum_{n=1}^{N} A_{mn} e^{i(-V\omega_x)t} e^{i\omega_x x} e^{i\omega_y y}$$

Figure 3.5. Equation. Surface load representation modified for vehicle speed.

As an example, a tire load with 15 cm radius footprint and a uniform tire pressure of 900 kPa is presented in **Figure 3.6**, **Figure 3.7**, and **Figure 3.8**, for perspective, top, and side views, respectively, considering M = 512 and N = 512 as the number of waves representing the load. The Fourier coefficient for this sample tire load was obtained by

applying the two-dimensional FFT. The Fourier coefficients typically have a complex form with real and imaginary parts. The absolute value of Fourier coefficients corresponding to this tire load are presented in **Figure 3.9**, **Figure 3.10**, and **Figure 3.11** for perspective, top, and side views, respectively.

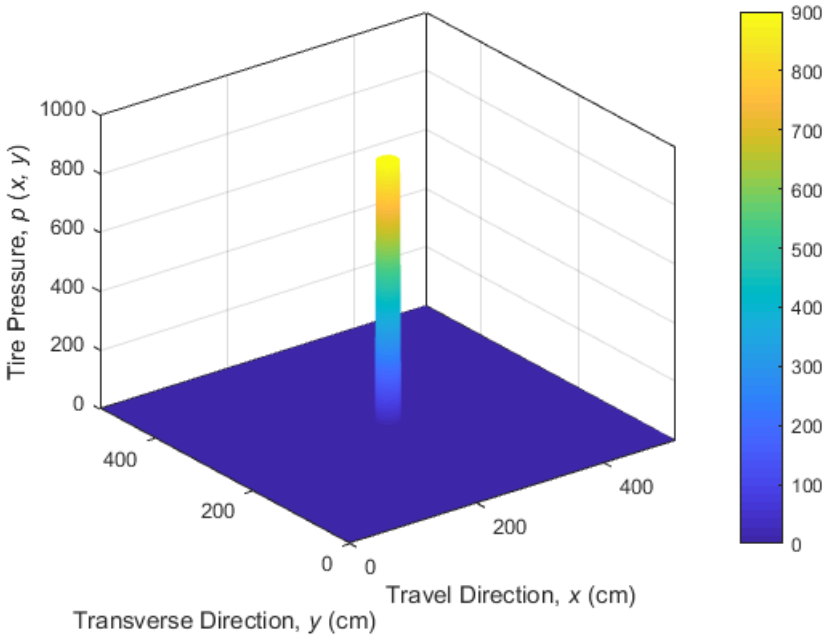

Figure 3.6. Plot. Schematic presentation of a tire load with 15 cm foot print radius and uniform 900 kPa uniform pressure (perspective view).

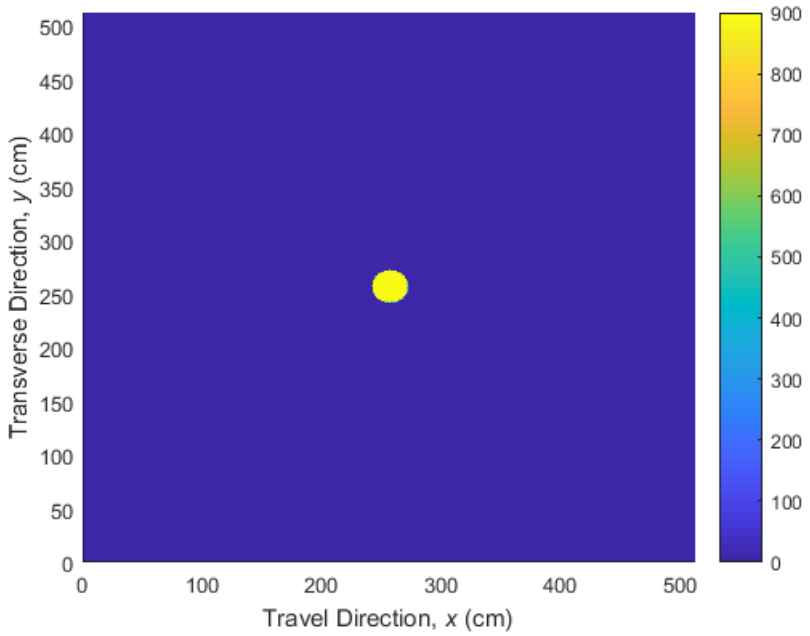

Figure 3.7. Plot. Schematic presentation of a tire load with 15 cm foot print radius and uniform 900 kPa pressure (top view).

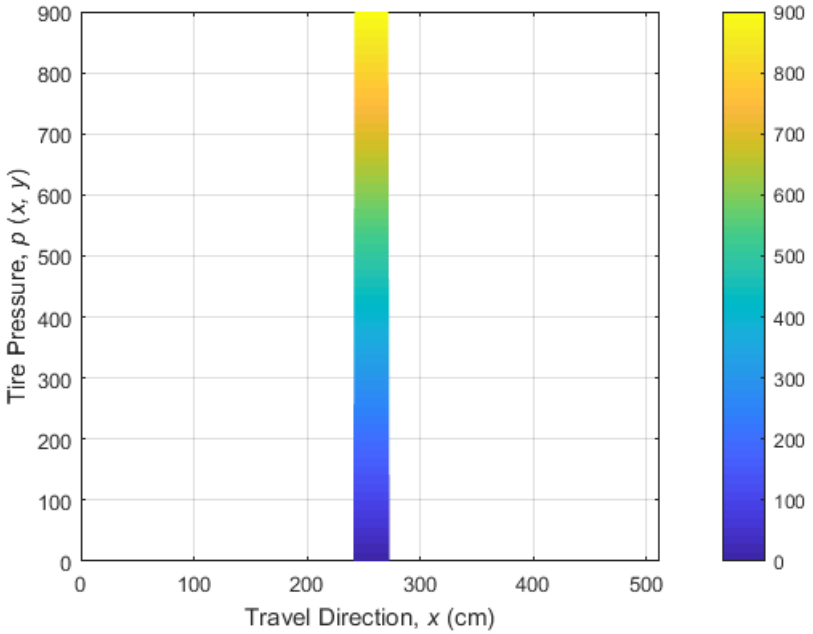

Figure 3.8. Plot. Schematic presentation of a tire load with 15 cm foot print radius and uniform 900 kPa pressure (side view).

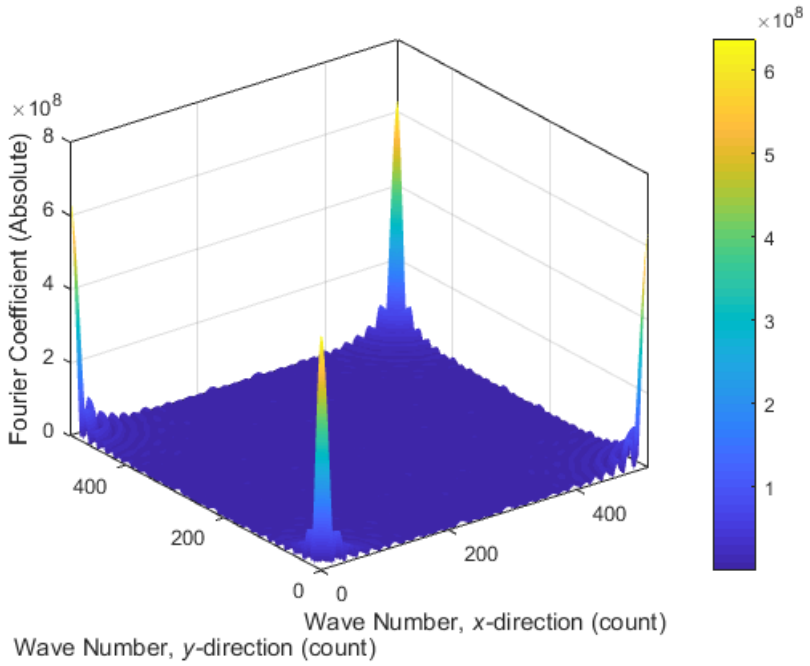

Figure 3.9. Plot. Absolute values of Fourier Coefficients of a tire load with 15 cm foot print radius and uniform 900 kPa pressure (perspective view).

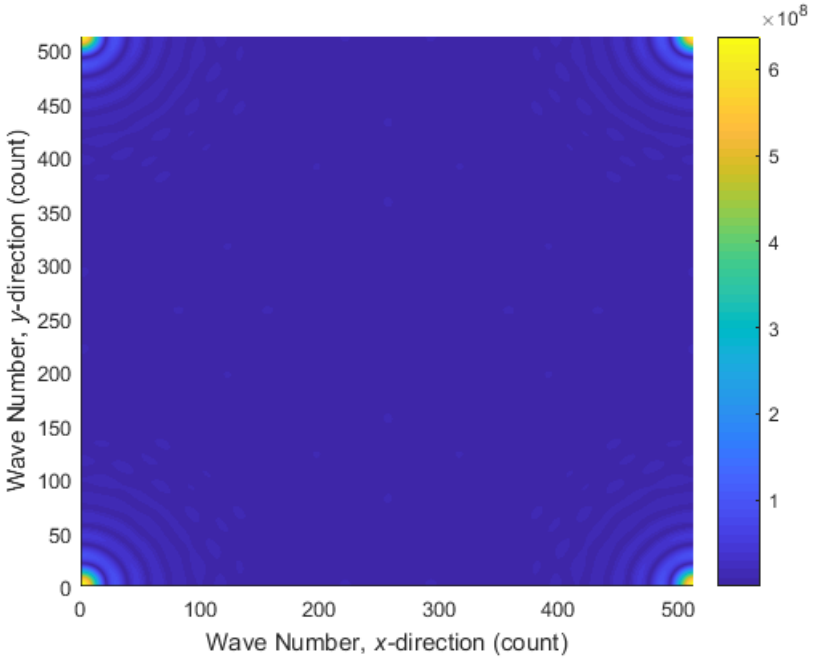

Figure 3.10. Plot. Absolute values of Fourier Coefficients of a tire load with 15 cm foot print radius and uniform 900 kPa pressure (top view).

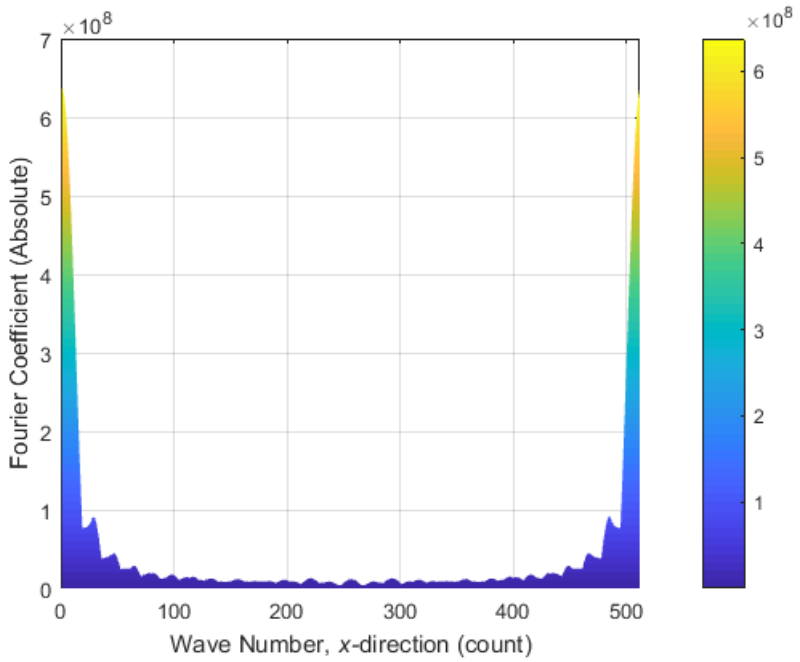

Figure 3.11. Plot. Absolute values of Fourier Coefficients of a tire load with 15 cm foot print radius and uniform 900 kPa pressure (side view).

3.4.2 General Forms of Displacements

As mentioned earlier, displacements are the main unknowns in the 3D-Move formulation. If the displacement field is known, then stress and strain fields are obtained by employing stress-displacement and strain-displacement constitutive equations, respectively. Denoting displacement in *x*-, *y*-, and *z*-directions with u_1, u_2, and u_3, respectively, the general form of displacements are presented in the equation in **Figure 3.12** for the three directions (j = 1, 2, 3).

$$u_j(x,y,z,t) = \sum_{m=1}^{M}\sum_{n=1}^{N} \tilde{u}_j(z) e^{i\omega_x(x-Vt)} e^{i\omega_y y}$$

Figure 3.12. Equation. General form of displacements.

In this equation, $\tilde{u}_j(z)$ is displacement amplitude at the depth of interest (z) in frequency domain. This equation is based on the wave propagation concept, in which $\tilde{u}_j(z)$ is a function of depth, as the waves propagate into the pavement structure.

3.4.3 Constitutive Equations

Constitutive equations are used to obtain stresses and strains from displacements. The normal strain-displacement constitutive equation is presented in **Figure 3.13**.

$$\varepsilon_{jj} = \frac{\partial uj}{\partial j}$$

Figure 3.13. Equation. Normal strain-displacement constitutive equation.

In this equation, ε_{jj} is normal shear strain in the j^{th} direction. The shear strain-displacement constitutive equation is presented in **Figure 3.14**.

$$\varepsilon_{jk} = \frac{1}{2}\left(\frac{\partial u_j}{\partial k} + \frac{\partial u_k}{\partial j}\right)$$

Figure 3.14. Equation. Shear strain-displacement constitutive equation.

In this equation, ε_{jk} is shear strain on the plane with normal in the *j* direction, and stretching in the *k* direction. The stress-displacement constitutive equations need more effort to be derived compared to strain-displacement equations. To obtain stress-displacement constitutive equations, stress-strain constitutive relationships should be developed first, and then combined with the strain-displacement equations. For the one-

dimensional case, the stress-strain relationship is simply represented by the well-known Hook's law. However, in the three-dimensional case, the normal stress-strain relationship is presented in **Figure 3.15**.

$$\sigma_{jj} = \lambda \cdot tr(\varepsilon) + 2G \cdot \varepsilon_{jj}$$

Figure 3.15. Equation. Normal stress-strain constitutive equation.

In this equation, λ and G are first and second Lamé parameters, respectively. It has been shown that the second Lamé parameter is equal to shear modulus. Furthermore, σ_{jj} is normal stress in the j^{th} direction, ε is the strain tensor, and $tr(.)$ is the trace function. In frequency domain, this equation is the equation presented in **Figure 3.16**.

$$\tilde{\sigma}_{jj} = \lambda \cdot tr(\tilde{\varepsilon}) + 2G \cdot \tilde{\varepsilon}_{jj}$$

Figure 3.16. Equation. Normal stress-strain constitutive equation (frequency domain version).

In this equation, ~ denotes the frequency domain equivalent for the parameter of interest. Applying strain-displacement derived earlier, one can develop normal stress-displacement constitutive equation. To derive shear stress-displacement constitutive equation, the shear strain-displacement equation developed earlier should be used coupled with shear stress-strain equation, which leads to the equation presented in **Figure 3.17**. All the parameters used in this equation are as previously defined.

$$\sigma_{jk} = G\left(\frac{\varepsilon_{jk}}{2} + \frac{\varepsilon_{kj}}{2}\right)$$

Figure 3.17. Equation. Shear stress-shear strain constitutive equation.

3.4.4 Solution Scheme

The equations of equilibrium of forces for an arbitrary element in a pavement structure and for a specific wave are presented in **Figure 3.18**.

$$\frac{\partial \sigma_{jk}}{\partial j} = \rho \frac{\partial^2 u_j}{\partial j^2}$$

Figure 3.18. Equation. Equilibrium equation.

In this equation, ρ is density and all parameters are as previously defined. Rearranging this equation using stress-displacement constitutive equations leads to a system of differential equations with three (3) equations and three (3) unknowns (i.e., displacements in the three (3) directions). By solving the system of equations, the solution presented in **Figure 3.19** is obtained for displacement in frequency domain for the specific wave of interest.

$$\tilde{u}_j = A_1 e^{n_1 z} + A_2 e^{n_2 z} + A_3 e^{-n_1 z} + A_4 e^{-n_2 z} + A_5 z \cdot e^{n_1 z} + A_6 z \cdot e^{n_2 z}$$

Figure 3.19. Equation. Solution for displacements in frequency domain.

This equation represents the displacement in the three (3) directions as the finite-layer solution of the pavement system, and is called the *displacement function*. In the displacement function, A_1 to A_6 are unknown coefficients for each layer, which are determined by boundary conditions. Furthermore, n_1 and n_2 are the eigenvalues for the pavement system, which are calculated using the equations presented in **Figure 3.20** and **Figure 3.21**. In these equations, all parameters are as previously defined.

$$n_1 = \sqrt{\omega_x^2 + \omega_y^2 - \frac{\rho(\omega_x \cdot V)^2}{\lambda + 2G}}$$

Figure 3.20. Equation. First eigenvalue for pavement system.

$$n_2 = \sqrt{\omega_x^2 + \omega_y^2 - \frac{\rho(\omega_x \cdot V)^2}{G}}$$

Figure 3.21. Equation. Second eigenvalue for pavement system.

After calculating displacements, stresses and strains would be calculated using their corresponding constitutive equations, which were presented earlier.

3.4.5 Boundary Conditions

Boundary conditions are employed to obtain the six (6) unknown coefficients (A_1 to A_6) of the displacement function (equation presented in **Figure 3.19)**. There are three (3) types of boundary conditions: 1) surface boundary, 2) interface boundary, and 3) bottom boundary. For a pavement structure composed of *C* layers, there are three (3) surface

boundary conditions, 6 × (*C*-1) interface boundary conditions, and three (3) bottom boundary conditions, for each individual wave. Therefore, there are 6*C* boundary conditions that may be used to find A_1 to A_6 appeared in the displacement function, for every layer (6*C* unknowns).

Based on 3D-Move formulation, surface boundary conditions are in terms of vertical normal stress and shear stresses (longitudinal and lateral) applied on the pavement surface. Load representation for surface normal stress can be found in the equation presented in **Figure 3.4**. The same representation could be used for longitudinal and lateral shear stresses. In general, normal stress and shear stress may be defined by the equation presented in **Figure 3.22** where $j = 1$, $j = 2$, and $j = 3$ correspond to *x*-, *y*-, and *z*-directions, respectively.

$$\sigma_{jz}(x,y) = \sum_{m=1}^{M}\sum_{n=1}^{N}\left(\hat{\sigma}_{jk}\right)_{mn} e^{i\omega_x(x-V\cdot t)} e^{i\omega_y y}$$

Figure 3.22. Equation. Surface load representation for normal stress and shear stresses.

In this equation, $\left(\hat{\sigma}_{jk}\right)_{mn}$ is the Fourier coefficient matrix and all the other parameters are as previously defined. The surface boundary conditions are the equations presented in **Figure 3.23**.

$$\tilde{\sigma}_{jk}(\omega_x, \omega_y, 0) = \hat{\sigma}_{jk}(\omega_x, \omega_y, 0)$$

Figure 3.23. Equation. Three (3) surface boundary conditions.

Recall that $\tilde{\sigma}_{jk}$ and $\hat{\sigma}_{jk}$ are frequency domain values for pavement stress responses and applied stress for a wave with spatial frequencies of ω_x and ω_y in *x*- and *y*-direction, respectively.

As for the interface boundary conditions, considering fully bonded conditions at layer interfaces, boundary conditions would be the equality of stresses and displacements for upper and lower layers at their interface. There are three (3) equilibrium equations and three (3) continuity equations at layer interfaces. Equations presented in **Figure 3.24** and **Figure 3.25** present equilibrium and continuity equations, respectively.

$$\tilde{\sigma}_{jz}^{-}(\omega_x, \omega_y, H) = \tilde{\sigma}_{jz}^{+}(\omega_x, \omega_y, 0)$$

Figure 3.24. Equation. Three (3) equilibrium equations for layer interface boundary conditions.

$$\tilde{u}_{j}^{-}(\omega_x, \omega_y, H) = \tilde{u}_{j}^{+}(\omega_x, \omega_y, 0)$$

Figure 3.25. Equation. Three (3) continuity equations for layer interface boundary conditions.

In this equation, $\tilde{\sigma}_{jz}^{-}(\omega_x, \omega_y, H)$ and $\tilde{\sigma}_{jz}^{+}(\omega_x, \omega_y, 0)$ are stress at the bottom of upper layer and at the top of lower layer, respectively, considering *H* is the thickness of the upper layer. Furthermore, $\tilde{u}_{j}^{-}(\omega_x, \omega_y, H)$ and $\tilde{u}_{j}^{+}(\omega_x, \omega_y, 0)$ are displacement in the j^{th} direction at the bottom of the upper layer and at the top of the lower layer,

respectively. All parameters used in this equation are in frequency domain for a specific wave with spatial frequencies of ω_x and ω_y in *x*- and *y*-directions, respectively.

The bottom boundary conditions are considered as no displacement at a certain depth of the last layer. The equation for the bottom boundary condition is presented in **Figure 3.28**.

$$\tilde{u}_j(\omega_x, \omega_y, H_N) = 0$$

Figure 3.26. Equation. Three (3) bottom boundary conditions.

In this equation, H_N is the location of the bottom boundary with respect to the last layer interface.

3.4.6 Viscoelastic Material Characterization

One of the unique features of 3D-Move is viscoelastic material characterization. Since the formulation is based on Fourier transform, the frequency of each wave can be used to obtain the corresponding elastic modulus of viscoelastic material such as asphalt concrete (AC). Based on the equation presented in **Figure 3.5**, time frequency of loading may be calculated using the equation presented in **Figure 3.27**.

$$\omega_t = -\omega_x \cdot V$$

Figure 3.27. Equation. Time frequency of loading for viscoelastic material characterization.

Recalling that in this equation, V is the speed of the vehicle and ω_x is the spatial frequency for the wave of interest in the x-direction. ω_t may be used with an AC shear modulus master curve or a rheological model (e.g., Kelvin model, Maxwell model, Burger model, etc.) to determine the viscoelastic material shear modulus for the wave of interest using its frequency. The equation presented **Figure 3.27** states that the time frequency of loading is a function of vehicle speed. Knowing that the effect of pavement temperature is included in dynamic modulus master curve, the pavement temperature and vehicle speed are taken into consideration in the formulation of 3D-Move.

3.5 Enhancements to 3D-Move Analysis®

In the previous section, the 3D-Move ENHANCED formulation was described. However, a number of additional enhancements were incorporated into this formulation, and they are discussed in this section. These enhancements include generating surface plots, interface bond conditions, and runtime improvement.

3.5.1 Surface Plots

In the original 3D-Move formulation, pavement mechanical responses were calculated for a specific point within pavement structure using an iteration process for all the waves in x- and y-directions. However, in the new formulation (i.e., 3D-Move ENHANCED), inverse Fourier transform was employed to obtain surface plots for pavement responses at a specific depth. In this method, the corresponding response for each wave is first calculated in frequency domain. Then, the response is transformed into spatial domain using inverse Fourier algorithm. These methods can be applied for all fifteen (15)

mechanical responses (i.e., three (3) displacements, six (6) stresses, and six (6) strains). It is worth mentioning that the surface plot of responses can be generated for a particular time step of analysis. As an example, the top and perspective view for a sample superheavy quad axle are presented in **Figure 3.28** and **Figure 3.29**. The vertical surface displacement under this superheavy quad axle traveling at climbing speeds is presented in **Figure 3.30** as a three-dimensional (3-D) surface plot.

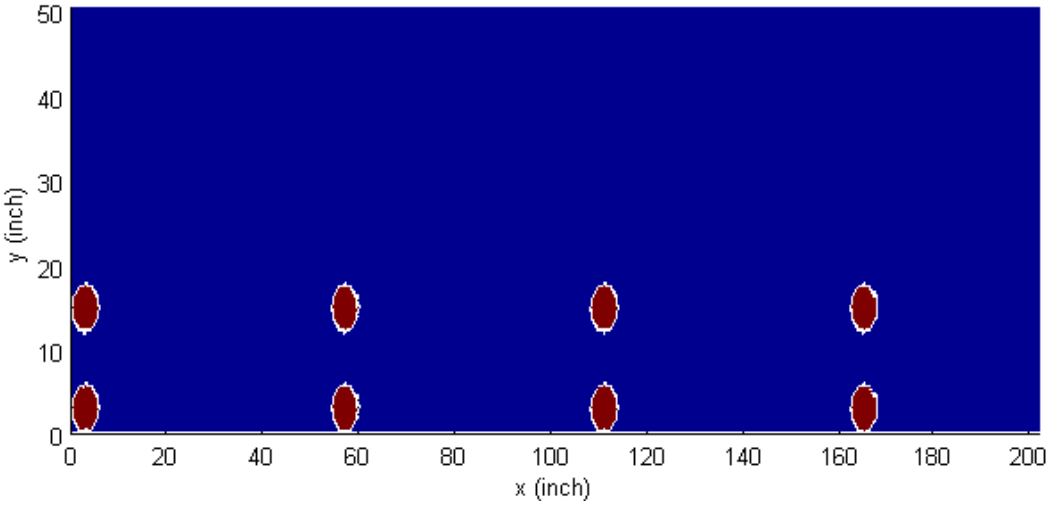

Figure 3.28. Illustration. A sample quad superheavy quad axle (top view).

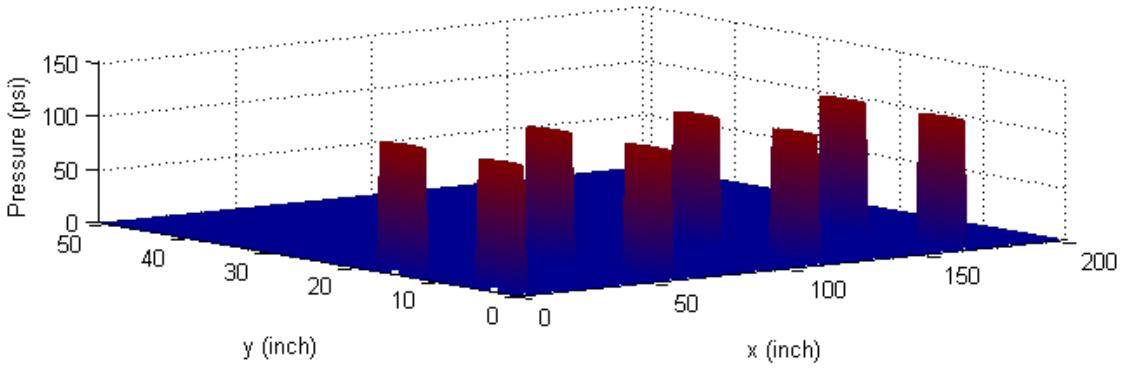

Figure 3.29. Illustration. A sample quad superheavy quad axle (perspective view).

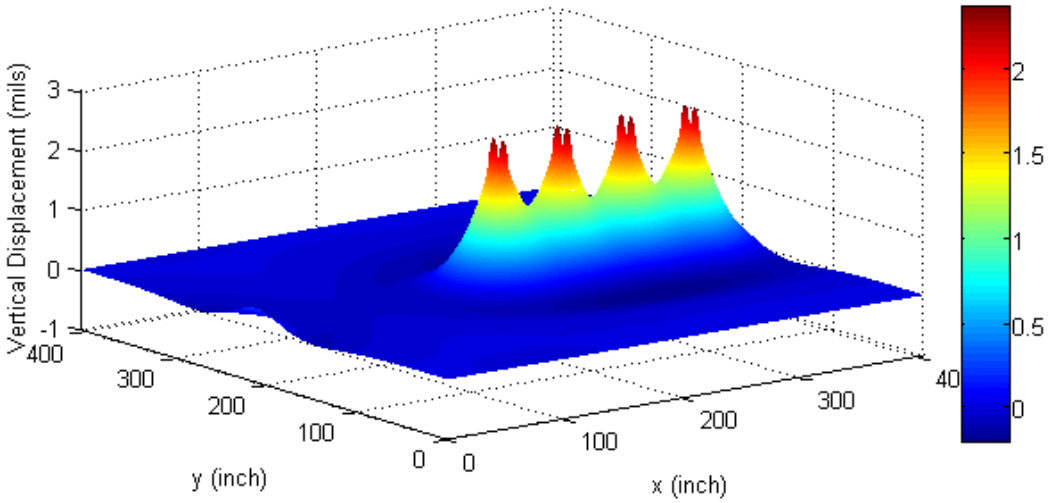

Figure 3.30. Illustration. Surface plot for vertical displacement at pavement surface under sample superheavy quad axle.

3.5.2 Interface Bond Conditions

Interface debonding is a significant issue in pavement construction because the only solution is to remove and replace the debonded AC areas (S.-F. Kazemi, Hand, Hajj, Sebaaly, & Siddharthan, 2017). This issue is particularly critical for pavements subjected to SHL, or airfield pavements that are constructed to carry large aircraft loadings (Arabali, Sakhaeifar, Freeman, Wilson, & Borowiec, 2017). Sometimes mitigation strategies such as steel plates are used to decrease the detrimental effects of overweight vehicle or superheavy load vehicle moves. In this case, the steel plates and existing

pavement surface layer do not represent a fully bonded condition. Therefore, proper modeling of layer bond condition is essential for flexible pavements experiencing SHL move. Layer interface debonding was incorporated into 3D-Move ENHANCED.

The analytical approach used in the 3D-Move ENHANCED formulation, specifically the formulation of interface boundary conditions allows for effective incorporation of various interface bond condition models. The equations employed in 3D-Move ENHANCED for interface boundary condition considering fully bonded conditions is presented in **Figure 3.24** and **Figure 3.25** for continuity and equilibrium criteria, respectively. These equations assume fully bonded conditions at the layer interface. There has been several methods suggested in the literature to model slippage or debonding at layer interfaces (De Jong et al., 1972; Maina, De Beer, & Matsui, 2007). The slippage model developed by Maiana et al. was used to model interface bond conditions. Based on this model, the layer interface boundary condition should be modified to account for layer interface debonding. The modified equation for interface layer boundary conditions, considering layer interface bond conditions are presented in **Figure 3.31** and **Figure 3.32** for *x*- and *y*-directions, respectively.

$$u_1^-(H_i) - \tilde{u}_1^+(0) = \frac{\tau_{xz}^i(H_i)}{K_{xx}}$$

Figure 3.31. Equation. Modified layer interface boundary conditions to include interface bond conditions in *x*-direction.

$$u_2^-(H_i) - \tilde{u}_2^+(0) = \frac{\tau_{yz}^i(H_i)}{K_{yy}}$$

Figure 3.32. Equation. Modified layer interface boundary conditions to include interface bond conditions in *y*-direction.

In these equations, the formulation is provided for the interface of i^{th} and $(i + 1)^{th}$ layer, noting that the closest layer to pavement surface is numbered as 1; and layer number increases with increasing depth. Also, K_{xx} and K_{yy} are slippage stiffness in *x*- and *y*- directions, respectively; $u_1^-(H_i)$ and $u_2^-(H_i)$ are displacements in *x*- and *y*-directions, respectively, at the bottom of i^{th} layer; $u_1^+(0)$ and $u_2^+(0)$ are displacements in *x*- and *y*-directions, respectively, on top of the $(i + 1)^{th}$ layer; and $\tau_{xz}^i(H_i)$ and $\tau_{yz}^i(H_i)$ are longitudinal and lateral shear stresses, respectively, at the interface of i^{th} and $(i + 1)^{th}$ layer. A schematic of modeling layer debonding in 3D-Move is presented in **Figure 3.33**.

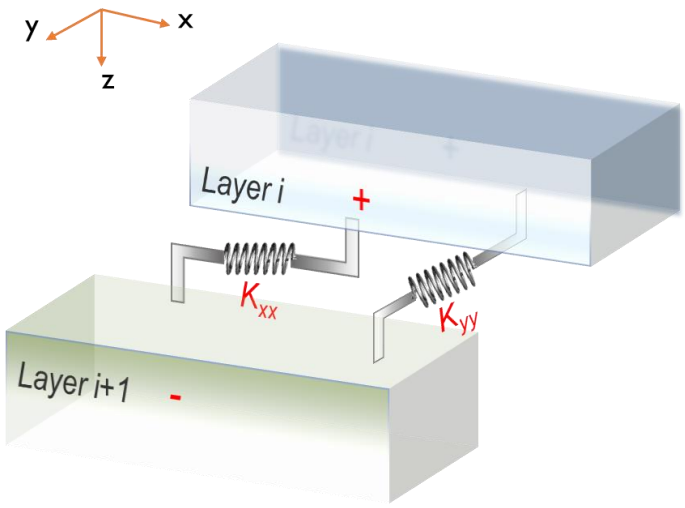

Figure 3.33. Illustration. Schematic of modeling layer debonding in 3D-Move.

3.5.3 Runtime Improvement

As previously mentioned, MATLAB was used to develop 3D-Move ENHANCED. Employing inverse Fourier transform was very effective in reducing 3D-Move ENHANCED runtime compared to the iteration method used in the original formulation, which is based on computing response(s) of interest at specific response points using summation of all responses over all waves. Not only is the new approach substantially faster than the original approach, but it also generates surface plots for different response types.

Another mechanism used to improve runtime was parallel processing (Rauber & Rünger, 2013). In fact, formulation of 3D-Move ENHANCED allows for using parallel processing, because the waves can be processed independently. Therefore, values for response(s) of interest could be determined by assigning waves to different processing units. Finally, responses in frequency domain are collected from all the processing units and assembled. Pavement responses are transformed into space domain using inverse Fourier transform. The speed up factor was close to 3.0 for a quad processor (75% speed up factor), showing that parallel processing could efficiently improve 3D-Move ENHACNED runtime. 3D-Move ENHANCED runtime for different number of pavement layers ranging from one (1) to 10 (ten) layers is presented in **Table 3.1**. The considered pavement structure was comprised of a surface layer with viscoelastic material, and elastic material for the rest of the layers.

Table 3.1. Runtime for 3D-Move ENHANCED Considering Parallel Processing Using Four (4) Processing Units.

Number of Layers	Runtime (second)
1 (one)	11
2 (two)	22
3 (three)	33
4 (four)	45
5 (five)	56
6 (six)	67
7 (seven)	79
8 (eight)	90
9 (nine)	102
10 (ten)	115

3.6 Summary

In this chapter, the formulation of 3D-Move was presented. First, the original formulation of 3D-Move was presented. This formulation was implemented in the 3D-Move Analysis ® software. Thereafter, the 3D-Move ENHANCED formulation along with its enhancement compared to the original 3D-Move formulation was presented. 3D-Move ENHANCED was used as the engine for calculating pavement mechanical responses in the SuperPACK software, a software for analyzing flexible pavements exposed to superheavy load moves. In both formulations (called the 3D-Move formulation), pavement mechanical responses are computed under a vehicle load that is traveling at a constant speed. The formulation is based on finite-layer approach, which implements the concept of wave propagation. The surface load is represented as a composition of waves traveling in *x*- and *y*- directions using a two-dimensional fast Fourier transform (FFT). Subsequently, all the calculations are performed in the frequency domain. The main unknowns of 3D-Move ENHANCED are displacements in the three (3) directions.

Stresses and strains are calculated based on displacements using stress-displacement and strain-displacement constitutive equations, respectively. The 3D-Move formulation is capable of modeling viscoelastic material behavior.

A number of enhancement were made to the original 3D-Move formulation in the development of 3D-Move ENHANCED. Modifications included characterization of surface loading, interface conditions that allow for slippage, and runtime improvement. Since inverse Fourier transform is employed in 3D-Move ENHANCED, surface plots for a particular response could be obtained at the desired depth(s). Parallel processing was incorporated into the formulation noting that waves could be processed independently.

CHAPTER 4 3D-FAST FORMULATION: FINITE-LAYER SOLUTION FOR DYNAMIC LOADING CONDITIONS

4.1 Introduction

3D-FAST (***3-D***imensional ***F***ourier ***A***nalysis of pavement ***S***tructures under ***T***ransient loading) is the model developed as the primary objective of this research. 3D-FAST is a finite-layer model to compute pavement mechanical response (i.e., stresses, strains, and displacements, velocities, and acceleration). There are different aspects associated with 3D-FAST including load characterization, wave propagation, displacement function, constitutive equation, frequency domain calculations, boundary conditions, viscoelastic material characterization, superposition principle, and model runtime. In this introduction, a general description is provided for these aspects.

Realistic pavement surface loading is a substantial feature of 3D-FAST. In many currently available software packages there are three limitations with surface loading: 1) surface load must be of uniform stress distribution, 2) surface load should be circular in shape, and 3) surface load should be symmetric. In particular, models that use multi-layer elastic theory (MLET) require the load to be circular with uniform stress distribution. The reason for that is MLET uses Hankel transform. With finite-element method (FEM) there is typically no limitation on load shape and stress distribution. However, appropriate meshing is an important issue since defining a fine mesh to represent the surface load increases the model runtime. If modeling dynamic load is the case, meshing becomes even a greater concern. With 3D-FAST formulation, however, since the model uses discrete Fourier transform, there is no concern with respect to model convergence. The

meshing should be fine enough so that the details of the loading is captured appropriately. Theoretically, the sampling frequency of load should be higher than the Nyquist frequency which is the minimum rate at which the loading signal should be sampled (Oppenheim, 1999). Siddharthan et al. investigated the sampling frequency of the load and concluded that a node spacing of $\Delta x = \Delta y = 0.01$ m meets the requirement for Nyquist frequency theorem (R. V. Siddharthan et al., 1998). The surface loading representation and associated formulation is discussed in **Section 4.2.1**.

The concept of wave propagation is central to the finite-layer method used in the development of 3D-FAST. In order to employ this concept, the loading should be transformed from spatial and time domains to the frequency domain. This transformation is carried out through a three-dimensional fast Fourier transform (3-D FFT) algorithm. The wave propagation concept considers that the waves obtained in the frequency domain propagate into the pavement structure. During the propagation process, the amplitude of the waves changes as a function of depth while the frequency remains constant. More details about the wave propagation concept and associated formulation is presented in **Section 4.2.2**.

Displacement function is the terminology used in this research to identify the displacement as a function of a series of input parameters. These inputs are layer unknowns, eigenvalues for the pavement system, and depth of interest. The displacement function in the finite-layer formulation of 3D-FAST has the same role as the shape functions in the finite-element method. This function is derived as a direct result of applying the wave propagation concept. The final step in the 3D-FAST formulation is

obtaining displacement function. The displacement functions are initially obtained in the frequency domain and will be transformed back to the spatial and time domains using a three-dimensional inverse fast Fourier transform (3-D IFFT) algorithm at the desired depth. The mathematical representation of displacement function is presented in **Section 4.2.5**.

The primary unknowns in 3D-FAST formulation are displacements. If the displacement field is known, all the other responses (e.g., stresses, strains.) can be obtained using the corresponding constitutive equations. For instance, stress-displacement constitutive equations are used to obtain the stress field based on the displacement field. While eventually all the responses are obtained in the spatial and time domain using IFFT, the derived constitutive equations are in the frequency domain since 3D-FAST formulation is in that domain. The derivation of constitutive equations is presented in **Section 4.2.4**.

Frequency domain calculation is a robust feature of 3D-FAST that incorporates a substantial flexibility into the model implementation. The frequency domain allows for a significant improvement of the model efficiency in terms of model runtime, implementation of superposition principle, using parallel processing, and material characterization. In **Chapter 5**, the unique computational features of 3D-FAST are discussed. These features are the direct outcome of using frequency domain for performing calculations.

Viscoelastic material characterization is a significant feature of 3D-FAST. A viscoelastic material exhibits both viscous and elastic deformation behavior as it

experiences loading. Generally speaking, viscoelastic materials have time-dependent deformation properties. There are two important aspects of viscoelastic material characterization in 3D-FAST formulation. First, this characterization is based on the assumption that the complex modulus of viscoelastic material is a function of loading frequency. Second, the linear viscoelastic material characterization conditions exist. For the first assumption, if complex modulus of the viscoelastic material is frequency dependent then it can be incorporated into 3D-FAST formulation. For instance, for asphalt concrete (AC) the results of dynamic modulus test can be used to characterize the complex modulus as a function of loading frequency. Typically, AC master curve is employed for this purpose. Viscoelastic rheological models (e.g., Kelvin, Maxwell, Burgers, and Zener) can also be used to characterize viscoelastic materials since the material complex modulus can be related to loading frequency using these models.

As for the second aspect of viscoelastic material characterization, linearity is the assumption. The linear viscoelastic assumption allows for the use of superposition principle presented by the Boltzmann's principle. The Boltzmann's principle is defined as the equation presented in **Figure 4.1**.

$$\sigma(t) = \int_{-\infty}^{t} E(t - t') \frac{d\varepsilon(t)}{dt'} d\, t'$$

Figure 4.1. Equation. Boltzmann's principle representing the superposition of loads for viscoelastic material characterization.

In this equation, $\sigma(t)$ and $\varepsilon(t)$ are the stress and strain at time *t*, *E* is the modulus, and *t*' is the integral variable. The interesting note is that the Boltzmann's principal is technically a convolution integral. By taking Fourier transform of both sides of this equation, the integral will be reduced to a simple multiplication in the frequency domain.

$$\sigma(\omega) = E(\omega) \cdot \varepsilon(\omega)$$

Figure 4.2. Equation. The representation of superposition in the frequency domain.

In this equation, $\sigma(\omega)$, $\varepsilon(\omega)$, and $E(\omega)$ are stress, strain, and modulus in the frequency domain, respectively. Though this equation is valid for one-dimensional uniaxial loading, it can be extended to accommodate three-dimensional conditions.

The equation presented in **Figure 4.2** is significantly practical as it is the key to use superposition principal in order to obtain a specific response under different loading scenarios without the need to perform additional analysis (i.e., additional 3D-FAST runs). Details about viscoelastic material characterization and associated formulation is presented in **Section 4.2.3**. Furthermore, details about using the superposition principle in 3D-FAST is presented in **Section 5.4**.

The boundary conditions are very critical in the solving process in the 3D-FAST formulation, which are used to obtain the unknowns of displacement function. These conditions include surface boundary conditions, layer interface boundary conditions, and bottom boundary conditions. There are six unknowns per layer per wave in the 3D-FAST formulation. These unknowns are obtained by employing boundary conditions. The

boundary conditions are applied for each and every wave obtained by the application of FFT on the load. The surface boundary conditions are based on the equilibrium of forces considering both vertical stress (e.g., tire load) and shear stresses (longitudinal and lather). Thus, one can model shear forces applied on the pavement surface based on the surface boundary conditions. Interestingly, these forces can be a function of time. Layer interface boundary conditions are based on the equilibrium of stresses and continuity equations. The layer interface boundary conditions are flexible in order to accommodate for layer debonding conditions. The bottom boundary condition is based on the zero displacement at a certain depth due to the rigid boundary (e.g., a bedrock layer) or can be modified to represent the semi-infinite boundary conditions for zero displacement at a relatively large depth. Details about the mathematical formulation of boundary conditions are presented in **Section 4.2.6**.

Runtime is an important aspect of every numerical model. An efficient computational runtime may not be achieved until processing units are employed efficiently and the computational tasks are assigned to those units at a highly optimized level. In general, model runtime for 3D-FAST is shorter compared to finite-element models. Furthermore, since associated calculations are conducted in the frequency domain, further improvement can be achieved. Use of parallel processing as well as non-uniform Fourier transforms are two means of reducing 3D-FAST runtime. Parallel processing is an efficient technique to reduce the runtime by assigning the computational tasks to different processing units considering that the tasks are fully or partially independent. For instance, parallel processing can effectively incorporated with Monte-

Carlo simulation as simulation steps are independent (D. Batioja-Alvarez, Kazemi, Hajj, Siddharthan, & Hand, 2017; D. D. Batioja-Alvarez et al., 2018). In the 3D-FAST formulation, since linear viscoelastic material characterization is the case, and superposition principle is applicable, therefore waves can be processed independently to obtain displacement function. Once all the waves are processed, the results can be superposed to assemble the response in the frequency domain, and consequently in the spatial and time domains using IFFT. Another approach to reduce model runtime is to use non-uniform Fourier transform. The uniform Fourier transform is based on equal mesh spacing leading to arithmetic progression of wave frequencies after applying FFT. However, the non-uniform FFT is based on processing part of the waves which the frequency of them does not necessarily form an arithmetic progression. The certain waves chosen to be processed using non-uniform Fourier transform should be ideally the waves that have the most contribution to the response of interest. Then, the corresponding response can be interpolated for the other waves, or those waves can be ignored. The non-uniform Fourier transform significantly decreases model runtime but does not analyze the entire spectrum of the waves, so it introduces some approximation to the results. Details about mathematical presentation of parallel processing and non-uniform Fourier transform, and associated interaction of them with the 3D-FAST formulation are presented in **Chapter 5**.

4.2 Formulation

The mathematical formulation of 3D-FAST is presented in this section. This formulation is performed in the frequency domain by initially transforming the load through fast

Fourier transform (FFT) algorithm. The load is basically a three-dimensional (3-D) matrix as a function of spatial coordinates *x* and *y* (*x* is travel direction and *y* is the horizontal direction perpendicular to it) and the time coordinate (denoted by *t*). Then, the general form of displacements (called displacement function in this research) are derived in the frequency domain which contains six unknowns per wave per layer based on the derived solution for displacement function. As previously mentioned in this chapter, the displacement function is derived based on the wave propagation concept using constitutive equations. The unknowns in the displacement function are calculated using the boundary conditions for each and every wave traveling in the spatial domains (*x* and *y*) and time domain (*t*). Once the displacement field is derived in the frequency domain, other responses (e.g., stresses, strains) can be derived using the corresponding constitutive equations. After processing all the waves, the responses in the spatial and time domains are obtained using inverse fast Fourier transform (IFFT). These responses are presented as three-dimensional matrices, and dimensions of them correspond to *x*, *y*, and *t*.

4.2.1 Surface Load Representation

In the developed formulation, pavement surface load is represented as a function of longitudinal direction (*x*-direction), transverse direction (*y*-direction), and time (*t*). **Figure 4.3** schematically presents the loading under an arbitrary load of any shape and stress distribution. The load needs to be discretized in *x*-, *y*-, and *t*-directions with evenly spaced nodes denoted by Δx, Δy, and Δt, respectively, so that a Fourier transform algorithm can be applied on the load matrix in order to transform it to the frequency domain.

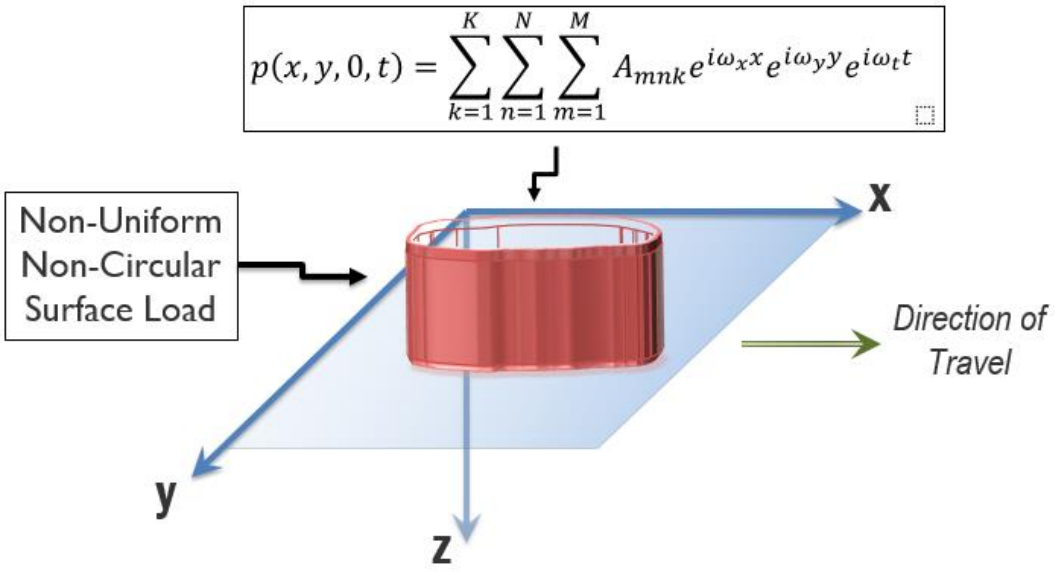

Figure 4.3. Photo. Schematic of non-uniform non-circular dynamic load in 3D-FAST.

Fast Fourier transform (FFT) is a common variant of Fourier transformation algorithms, which is considerably time efficient. A three-dimensional fast Fourier transform (3-D FFT) is applied on the dynamic load. The dynamic load representation employed in the 3D-FAST formulation is presented in **Figure 4.4**.

$$p(x,y,t) = \sum_{k=1}^{K}\sum_{n=1}^{N}\sum_{m=1}^{M} A_{mnk}e^{i\omega_x x}e^{i\omega_y y}e^{i\omega_t t}$$

Figure 4.4. Equation. Surface load representation (dynamic loading conditions).

In this equation, $p(x, y, t)$ is the loading (e.g., tire load) contact pressure which can be vertical normal stress (σ_{zz}), longitudinal shear stress (τ_{xz}), or transverse shear stress (τ_{yz}). The three-dimensional matrix of Fourier coefficients, A_{mnk}, is determined by

applying FFT on the load. The wave numbers corresponding to *x*-, *y*-, and *t*-directions are denoted by *m*, *n*, and *k*, respectively. The total number of waves in *x*-, *y*-, and *t*-directions are denoted by *M*, *N*, and *K*, respectively. Spatial frequency in the *x*-direction, *y*-direction, and time frequency are denoted by ω_x, ω_y, and ω_t, respectively. The imaginary unit is demonstrated as *i*.

4.2.2 Wave Propagation

The formulation of 3D-FAST is based on the finite-layer method, and wave propagation is central to this method. In general, each wave is characterized by three parameters: amplitude, frequency, and phase angle. As described in the load representation section, the dynamic loading applied on the pavement surface can be decomposed into a series of waves in the *x*-, *y*-, and *t*-direction using FFT. Waves are basically identified by elements of the A_{mnk} matrix. Each wave can be processed independently which allows for employing parallel processing. Additionally, different waves do not necessarily have the same contribution to a certain response at a specific response point. As a specific wave propagates into the pavement structure, the frequency of the wave does not change, however, the wave amplitude changes as a function of depth. **Figure 4.5** presents the concept of wave propagation schematically.

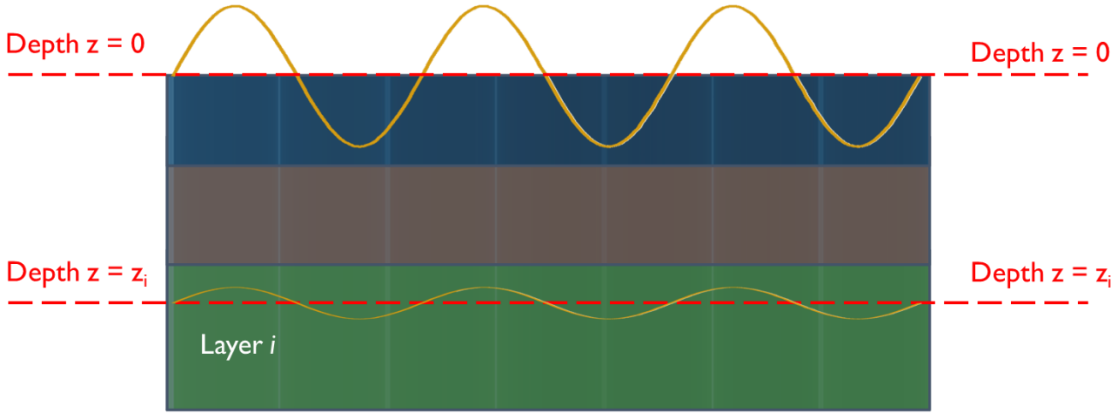

Figure 4.5. Illustration. Wave propagation concept in the finite-layer method.

Based on **Figure 4.5**, if the displacement at the pavement surface is represented by a wave, the displacement at an arbitrary depth of $z = z_i$ would be a wave that maintains the original load spatial and time frequencies (ω_x, ω_y, and ω_t) but with a different amplitude, which is a function of z_i. The mathematical equation obtained based on the wave propagation concept is called displacement function and is presented in **Figure 4.6**.

$$u_j(x,y,z,t) = \sum_{k=1}^{K}\sum_{n=1}^{N}\sum_{m=1}^{M} \tilde{u}_j(z) e^{i\omega_x x} e^{i\omega_y y} e^{i\omega_t t}$$

Figure 4.6. Equation. Displacement function representing general form of displacements.

In this equation, $u_j(x,y,z,t)$ is displacement and j = 1, 2, and 3 correspond to the displacement in x-, y-, and z-directions, respectively (see **Figure 4.3**). For instance, u_1 represents the displacement in the x-direction. The amplitude of the displacement is $\tilde{u}_j(z)$ in the frequency domain, which is a function of desired depth (z). All the other

parameters are as previously defined.

In the 3D-FAST formulation, the primary unknowns of the model are displacements, which is similar to FEM. While displacements in FEM are typically determined by the shape functions and element type, in the finite-layer method (e.g., 3D-FAST) displacements are a function of depth of interest and harmonics characteristics (i.e., amplitude, frequency, and phase sift) corresponding to the Fourier variables (*x*, *y*, and *t*). Displacement function is the terminology used for this function in the current study. The displacement function will be derived later as the solution of finite-layer method.

4.2.3 Viscoelastic Material Characterization

One of the exceptional features of 3D-FAST is the capability to accommodate for viscoelastic material characterization. According to the equation presented in **Figure 4.4**, dynamic load is decomposed into waves that travel in three directions (*x*, *y*, and *t*). The time frequency of loading (ω_t) can be used to obtain corresponding dynamic complex modulus for each wave for a viscoelastic layer such as AC. This frequency can be calculated using the equation presented in **Figure 4.7**.

$$\begin{cases} \omega_t = 2\pi \dfrac{k}{K.\Delta t} & k \le K/2 \\ \omega_t = -2\pi \dfrac{k}{K.\Delta t} & k > K/2 \end{cases}$$

Figure 4.7. Equation. Angular frequency of loading for the time Fourier variable.

In this equation, *k* is the wave number, *K* is the total number of waves in the time domain, and Δt is the load sampling interval in the time domain. The frequency used in this equation is the angular frequency of loading time. Typically, the frequency of loading time is used for dynamic modulus master curve to incorporate viscoelastic material characterization. The equation presented in **Figure 4.8** is used to convert angular frequency to frequency. In this equation, f_t is the frequency of loading time.

$$f_t = \omega_t / 2\pi$$

Figure 4.8. Equation. Conversion of angular frequency of loading time to frequency of loading time.

4.2.4 Constitutive Equations

As noted earlier, displacements are the primary unknowns in the 3D-FAST formulation. Strain-displacement and stress-displacement constitutive equations are employed to compute strains (normal and shear) and stresses (normal and shear) from the displacements, respectively. The derivation of constitutive equations for 3D-FAST is similar to that of 3D-Move as presented in **Section 3.4.3**.

Strain-displacement constitutive equations are presented in **Figure 4.9** using index notation.

$$\varepsilon_{jk} = \frac{1}{2}\left(\frac{\partial u_j}{\partial k} + \frac{\partial u_k}{\partial j}\right)$$

Figure 4.9. Equation. Strain-displacement constitutive equation.

In this equation, ε_{jk} is strain with *j* and *k* representing direction, which either of these two parameters can correspond to *x*-, *y*-, and *z*-directions, respectively (see **Figure 4.3**). If *j* and *k* refer to the same directions, then ε_{jk} represents normal strain. Otherwise, it represents shear strain.

Stress-strain constitutive relationships should be developed in order to derive stress-displacement constitutive equations. The normal stress-strain relationship in three-dimensional case is presented in **Figure 4.10**.

$$\sigma_{jj} = \lambda \cdot tr(\varepsilon) + 2G \cdot \varepsilon_{jj}$$

Figure 4.10. Equation. Normal stress-strain constitutive equation.

In this equation, λ and *G* are first and second Lamé parameters, respectively, noting that the second Lamé parameter is equal to shear modulus (Shames, 1997). Furthermore, σ_{jj} is normal stress in the j^{th} direction, ε is the strain tensor, and *tr*(.) is the trace function. In frequency domain, this equation is presented in **Figure 4.11**.

$$\tilde{\sigma}_{jj} = \lambda \cdot tr(\tilde{\varepsilon}) + 2G \cdot \tilde{\varepsilon}_{jj}$$

Figure 4.11. Equation. Normal stress-strain constitutive equation (frequency domain version).

In this equation, the ~ symbol represents the frequency domain equivalent of the parameter of interest. The normal stress-displacement constitutive equations are derived

by combining normal stress-strain constitutive equations (the equation presented in **Figure 4.11**) and strain-displacement constitutive equations (the equation presented in **Figure 4.9**).

Shear stress-displacement constitutive equations are derived by combining the shear stress-shear strain constitutive equations and shear strain-displacement constitutive equations. In this equation, all the parameters are as previously defined. The shear stress-shear strain constitutive equations are presented in **Figure 4.12**. The shear strain-displacement constitutive equations are previously presented in **Figure 4.9**.

$$\sigma_{jk} = G\left(\frac{\varepsilon_{jk}}{2} + \frac{\varepsilon_{kj}}{2}\right)$$

Figure 4.12. Equation. Shear stress-shear strain constitutive equation.

4.2.5 Solution Scheme

The first step of obtaining the solution of the finite-layer model for a pavement structure is employing the equilibrium equation (i.e., Newton's second law) in differential form for an arbitrary element of the pavement. The mathematical representation of this equation is presented in **Figure 4.13** using index notation.

$$\frac{\partial \sigma_{jk}}{\partial j} = \rho \frac{\partial^2 u_j}{\partial j^2}$$

Figure 4.13. Equation. Equilibrium equation in differential form.

In this equation, ρ is density and all the other parameters are as previously defined. Constitutive equations are employed to rewrite equation presented in **Figure 4.13** in terms of displacements. By replacing equation presented in **Figure 4.9** into the equation presented in **Figure 4.10** the normal stress-displacement constitutive equation is derived. Furthermore, by replacing presented in **Figure 4.9** in **Figure 4.12**, the shear stress-displacement constitutive equation is obtained. Using these two displacement-based constitutive equations, one can rewrite **Figure 4.13** in terms of displacement only without any stress or strain parameters. Solving the system of partial differential equations corresponding to Equation (8) leads to the following form for displacement function in the j^{th} direction:

$$\tilde{u}_j = A_1 e^{n_1 z} + A_2 e^{n_2 z} + A_3 e^{-n_1 z} + A_4 e^{-n_2 z} + A_5 z \cdot e^{n_1 z} + A_6 z \cdot e^{n_2 z}$$

Figure 4.14. Equation. Displacement function obtained as the solution of finite-layer solution for the pavement system.

In this equation, z is the depth of interest and A_1 to A_6 are unknown coefficients specific to each layer and for the specific wave of interest. These unknowns are determined by surface, interface and bottom boundary conditions. The first and second eigenvalues for the pavement system, n_1 and n_2, are calculated using the equations presented in **Figure 4.15** and **Figure 4.16**, respectively.

$$n_1 = \sqrt{\omega_x^2 + \omega_y^2 - \frac{\rho \cdot \omega_t^2}{\lambda + 2G}}$$

Figure 4.15. Equation. First eigenvalue for pavement system.

$$n_2 = \sqrt{\omega_x^2 + \omega_y^2 - \frac{\rho \cdot \omega_t^2}{G}}$$

Figure 4.16. Equation. Second eigenvalue for pavement system.

The equations presented in **Figure 4.14**, **Figure 4.15**, and **Figure 4.16** are of significant importance in the 3D-FAST formulation. These equations represent the finite-layer solution for the displacement function. Recall that the displacement function in finite-layer method acts the same as the shape functions in FEM. However, it should be noted that the displacement function is in frequency domain and has to be transformed into spatial and time frequencies using an inverse Fourier transformation algorithm. Once displacements are derived using the equation presented in **Figure 4.14**, one can calculate other pavement mechanical responses such as stresses, strains, velocities, and acceleration using respective constitutive equations. Similar equations to **Figure 4.14** can be derived for these responses. All these similar equations will have six unknowns (A_1 to A_6) which are determined through boundary conditions as presented next.

4.2.6 Boundary Conditions

The boundary conditions are used to determine the unknowns that appear in the displacement function (A_1 to A_6) for a specific wave. Based on the formulation developed for 3D-FAST, there are $M \times N \times K$ waves in total. Based on the equation presented in **Figure 4.14**, there are six (6) unknowns per layer per wave. Therefore, considering that the pavement consists of C layers, the total number of unknowns would be $M \times N \times K \times C$ for a specific pavement system.

The unknowns of the displacement function can be identified by employing boundary conditions. Theoretically, the number of boundary conditions should be equal to number of unknowns so that the unknowns can be uniquely identified. Waves obtained by taking Fourier transform on the load are uniquely distinguished by their frequencies in the space and time domains (i.e., by ω_x, ω_y, and ω_t).

Totally, there are $6C$ boundary conditions for the layered pavement systems that can be applied for every wave out of the total $M \times N \times K$ waves. There are three (3) surface boundary conditions, $6(C\text{-}1)$ layer interface boundary conditions, and three (3) bottom boundary conditions.

In the 3D-FAST formulation, the three (3) surface boundary conditions are equality of vertical normal stress (σ_{zz}), longitudinal shear stress (σ_{xz}), and lateral shear stress (σ_{yz}) applied on the pavement surface to that of respective pavement responses at the surface. The load representation of surface normal stress was already presented in the equation presented in **Figure 4.4**. The same presentation can be made for longitudinal

and lateral shear stresses by generalizing the equation presented in **Figure 4.4**. The results would be the equation presented in **Figure 4.17**, which accounts for shear stresses applied on the pavement surface.

$$\sigma_{jz}(x,y,t) = \sum_{k=1}^{K}\sum_{n=1}^{N}\sum_{m=1}^{M}\left(\widehat{\sigma_{jz}}\right)_{mnk} e^{i\omega_x x} e^{i\omega_y y} e^{i\omega_t t}$$

Figure 4.17. Equation. Representation of vertical and shear surface loads in 3D-FAST formulation.

In these equations, j may correspond to *x*-, *y*-, or *z*-direction, thus, $\sigma_{xz}(x,y,t)$, $\sigma_{yz}(x,y,t)$, and $\sigma_{zz}(x,y,t)$ represent applied dynamic surface longitudinal shear stress, dynamic surface lateral shear stress, and dynamic surface vertical normal stress, respectively. The three-dimensional Fourier coefficient matrix is denoted by $\left(\widehat{\sigma_{jz}}\right)_{mnk}$ and all the other parameters are as previously defined. Using this notation, the surface boundary conditions can be represented by the equation presented in **Figure 4.18**.

$$\tilde{\sigma}_{jz}(\omega_x, \omega_y, \omega_t, z=0) = \hat{\sigma}_{jz}(\omega_x, \omega_y, \omega_t, z=0)$$

Figure 4.18. Equation. Surface boundary condition representation for 3D-FAST formulation.

In these equations, $\tilde{\sigma}_{jz}$ and $\hat{\sigma}_{jz}$ are frequency domain values of pavement stress response and applied stress, respectively, for a wave represented by spatial frequencies of ω_x and ω_y for *x*- and *y*-directions, respectively, and time frequency of ω_t.

The interface layer boundary conditions are based on the equilibrium and continuity criteria. The equilibrium conditions of stresses acting on the horizontal plane (*xy* plane) lead to three (3) layer interface boundary conditions. On the other hand, the continuity conditions lead to another three (3) equations based on the equality of displacements in three (3) perpendicular directions. Therefore, there are six (6) boundary conditions for each layer interface. These layer interface boundary conditions should be satisfied for every wave obtained by the equation presented in **Figure 4.17**. For a pavement structure with *C* layers, there are *C* - 1 interfaces, leading to 6 (*C* - 1) interface boundary conditions.

A mathematical representation should be derived for layer interface boundary conditions so that they can be incorporated into the 3D-FAST formulation. The first three (3) boundary conditions are based on the equality of stresses (vertical normal stress, longitudinal shear stress, and lateral shear stress; or σ_{zz}, σ_{xz}, and σ_{yz}) for the upper and the lower layers at the layer interface to ensure that equilibrium is satisfied. The layer interface boundary conditions based on the equilibrium criteria is formulated by the equation presented in **Figure 4.19**.

$$\tilde{\sigma}_{jz}^{-}(\omega_x, \omega_y, \omega_t, z = H) = \tilde{\sigma}_{jz}^{+}(\omega_x, \omega_y, \omega_t, z = 0)$$

Figure 4.19. Equation. Layer interface boundary conditions based on the equilibrium criteria.

This notation equation basically refers to three (3) equilibrium equations (corresponding to σ_{zz}, σ_{xz}, and σ_{yz}) where $\tilde{\sigma}_{jz}^{-}(\omega_x, \omega_y, \omega_t, z = H)$ and $\tilde{\sigma}_{jz}^{+}(\omega_x, \omega_y, \omega_t, z = 0)$ are frequency values of stress at the bottom of the upper layer and at the top of the lower layer, respectively, considering H is the thickness of the upper layer. In the finite-layer formulation, local coordinates are used for each layer in the z-direction. It worth mentioning that as previously mentioned in **Chapter 2**, each layer is considered as an element by itself in the finite-layer method. Therefore, a local coordinate is used to identify the depth (z in the equation presented in **Figure 4.19**). A schematic presentation of global and local z coordinates are presented in **Figure 4.20** again noting that 3D-FAST uses local coordinates.

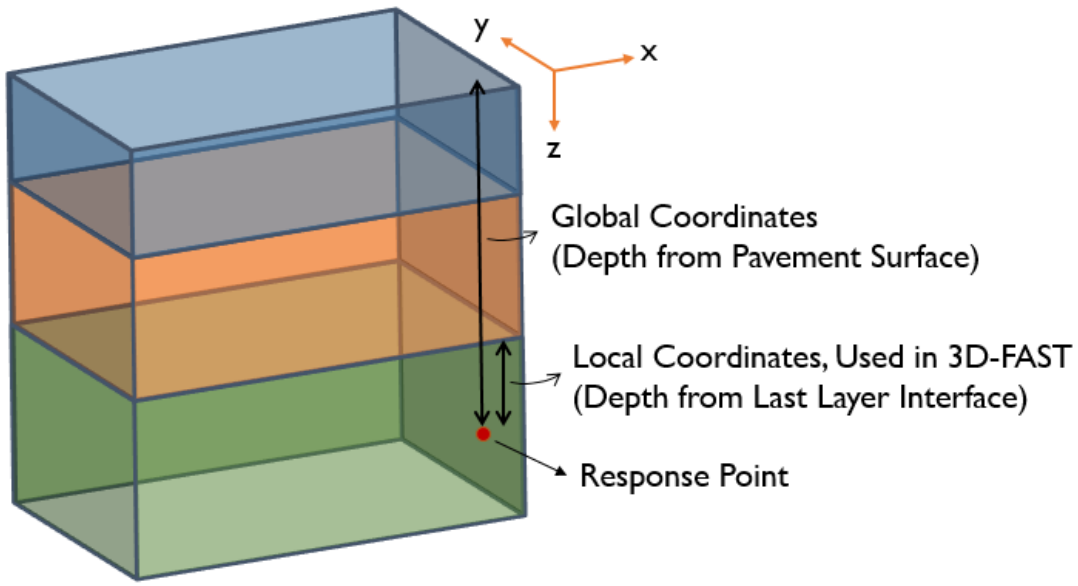

Figure 4.20. Illustration. Displaying the global and local coordinate for depth of interest (vertical or *z*-direction).

For fully bonded conditions at layer interfaces, there are three boundary conditions associated with continuity criteria based on the displacement equality of upper and lower layers. There are three continuity equations which can be summarized into one equation as presented in **Figure 4.21** using index notation.

$$\tilde{u}_j^-(\omega_x, \omega_y, \omega_t, z = H) = \tilde{u}_j^+(\omega_x, \omega_y, \omega_t, z = 0)$$

Figure 4.21. Equation. Layer interface boundary conditions based on the continuity criteria.

In these continuity equations, $\tilde{u}_j^-(\omega_x, \omega_y, \omega_t, z = H)$ and $\tilde{u}_j^+(\omega_x, \omega_y, \omega_t, z = 0)$ are displacements in the j^{th} direction at the bottom of the upper layer and at the top of the lower layer, respectively.

The displacement function presented in **Figure 4.14** contains six unknowns per layer per wave. Assuming that the pavement is consisted of *C* layers, a total of 6*C* unknowns per wave exist for this function. For the pavement system to be structurally determinate, there should be 6*C* boundary conditions so that the unknowns can be uniquely identified. A pavement system with *C* layers has *C* – 1 interfaces, thus there are 6 (*C* – 1) layer interface boundary conditions per wave. Considering three (3) surface boundary conditions based on the stress equilibrium, the total number of surface and layer interface boundary conditions would be 3 + 6 (*C* – 1) = 6*C* – 3 for a specific wave. Therefore, another three (3) boundary conditions are needed so that the total number of boundary conditions per wave are equal to the total number of unknowns in the

displacement function. These three (3) additional boundary conditions are derived based on the zero displacement at the bottom boundary.

The bottom boundary conditions are zero displacement in three (3) perpendicular directions at a certain depth. If semi-infinite conditions are to be modeled, the thickness of the last layer may be considered relatively large. Otherwise, if a stiff layer exists as the last layer (e.g., bedrock), the bottom boundary can be considered at the top of that stiff layer so that displacements are equal to zero at that interface. The mathematical representation of the bottom boundary would be as the equation presented in **Figure 4.22** using the index notation.

$$\tilde{u}_j(\omega_x, \omega_y, \omega_t, H_N) = 0$$

Figure 4.22. Equation. Bottom boundary conditions based on the zero displacement criteria.

The equation presented in **Figure 4.22** is representative for three (3) bottom boundary conditions, where H_N is the location of the bottom boundary with respect to the last layer interface. To model semi-infinite conditions for the thickness of the last layer, H_N can be considered a relative large number. Based on these three (3) bottom boundary conditions, the total number of surface, layer interface, and bottom boundary conditions would be $3 + 6\,(C - 1) + 3 = 6C$ per wave, considering pavement structure contains C layers. Thus, the number of boundary conditions will be equal to the number of unknowns in the displacement function (equation presented in **Figure 4.14**) so that all of

these 6*C* unknowns can be determined by solving for all of the boundary conditions at the same time represented by a system of equations for each and every $M \times N \times K$ waves. **Figure 4.23** schematically presents the surface and bottom boundary conditions, as well as interface boundary conditions for one of the pavement layer interfaces.

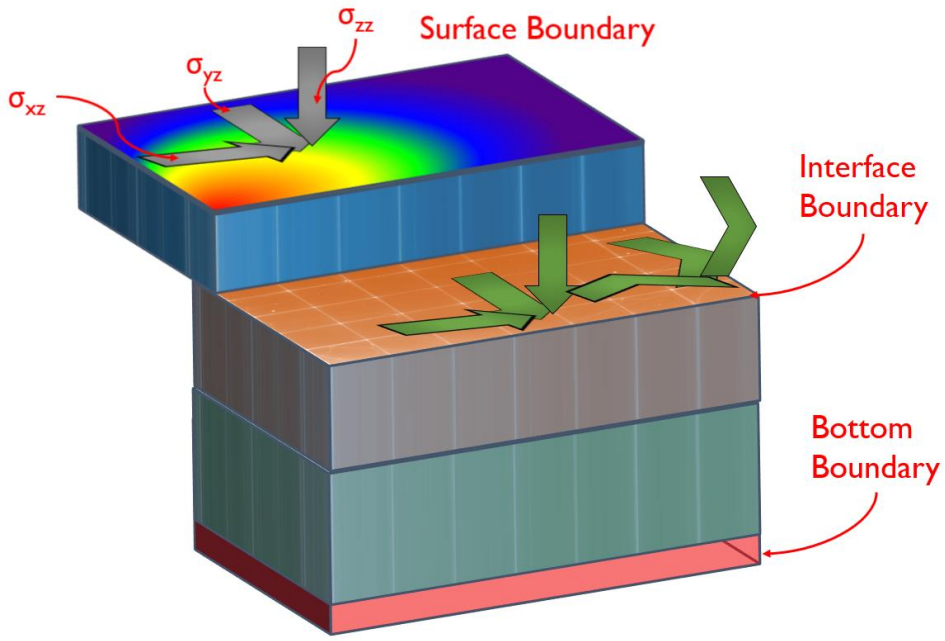

Figure 4.23. Illustration. Representation of surface, layer interface, and bottom boundary conditions.

CHAPTER 5 3D-FAST UNIQUE COMPUTATIONAL FEATURES

5.1 Introduction

The formulation of 3D-FAST was presented in detail in **Chapter 4**. This formulation was based on the finite-layer approach and covered different aspects that 3D-FAST considers in the modeling of pavement structure. First and foremost, 3D-FAST carries out all the associated calculations by taking the Fourier transform of the dynamic load and this transformation is made on the two spatial variables defining the horizontal plane (i.e., *x*- and *y*-directions) and the time dimension (i.e., *t*) so that these calculations will be conducted in the frequency domain. Performing calculations in the frequency domain results in a various number of advancements to 3D-FAST, which are the direct consequence of using this domain. These advancements are introduced in the following:

- Viscoelastic material characterization is a significant aspect of using frequency domain for 3D-FAST formulation. This property is significantly important because asphalt concrete (AC) modulus is substantially a function of loading frequency. If a dynamic load is applied on the pavement surface, different harmonic components of the load will excite different frequencies with different respective amplitudes so that each harmonic has its specific modulus depending on the function relating dynamic modulus to the time frequency of the loading (e.g., AC dynamic modulus master curve).

- Inverse fast Fourier transform (IFFT) allows for obtaining the animated surface plots at a specific depth. In the original 3D-Move formulation, an

iteration scheme was used to transform back the responses from frequency domain to spatial domains. In 3D-FAST formulation (as well as 3D-Move ENHANCED), inverse Fourier transform was employed as a means to obtain responses for the entire loading domain in a substantially short period of time (typically less than a second). The application of IFFT not only provides a faster means for calculating pavement mechanical responses, but also provides responses for all the nodes at a specific depth, rather than only at a limited number of response points. In other words, responses are obtained for a larger number of nodes ($M \times N$ spatial nodes and for all the K time steps; see equation presented in **Figure 4.4**) at a substantially faster computational runtime. This approach is significantly faster compared to the original iteration scheme used in 3D-Move formulation. Details about using IFFT and obtaining surface plots are presented in **Section 5.2**.

- The frequency domain calculation feature of 3D-FAST allows for a number of enhancements in terms of computational runtime. Furthermore, since 3D-FAST considers linear viscoelastic (LVE) conditions, then superposition principle is applicable to the formulation meaning that different waves can be processed independently, and then the results of the process can be superposed in order to account for the contribution of waves to a particular response at the point (or depth) of interest. Since harmonic components of the load (identified by the equation presented in **Figure 4.4**) can be processed independently, parallel processing technique can be used to further speed-up 3D-FAST

computational runtime. Depending on the number of available processing units, the speed-up factor varies noting that typically higher number of processing units leads to a higher speed-up factor. Details about implementing parallel processing in 3D-FAST and its effect on the model runtime are described in **Section 5.3**. Measures used to evaluate the efficiency of implementing parallel processing technique are also presented in that section.

- Linear time-Invariant property (LTI) is a property of the pavement system which is satisfied based on the 3D-FAST formulation as long as linear viscoelastic (LVE) material characteristics is the case. The LTI property of the pavement system coupled with the frequency domain calculations allows for using the superposition principal. In fact, the superposition principle (as defined by the Boltzmann's equation presented in **Figure 4.1**) simplifies to a multiplication in the frequency domain (see the equation presented in **Figure 4.2**). Details about the LTI property of the pavement system and how that incorporates into the superposition principle is presented in **Section 5.4**.

- Non-uniform Fourier transform is another aspect of 3D-FAST formulation. The node spacing should be equal and it should satisfy the criteria presented by the Nyquist theorem in order to apply FFT algorithm on the dynamic loading. However, for the analysis of the waves comprising the load, only certain number of waves can be processed and the contribution of the other waves can be estimated based on the contribution of the processed waves using an interpolation scheme. Typically, the process is based on the analysis

of certain waves considering the unit (Dirac delta function) load. Responses are computed for the processed waves in frequency domain, noting that the unit load excites all the waves equally (i.e., with the same amplitude) in frequency domain. Then, responses for other (not processed) waves are obtained by employing an estimation method such as interpolation. Responses of interest are obtained using the convolution integral explained in **Section 5.4**, which is the direct application of LTI property of the pavement system. The use of non-uniform Fourier transform significantly reduces 3D-FAST runtime but introduces some approximation into the model. Details about implementing the non-uniform Fourier transform is presented in **Section 5.5**.

5.2 Inverse Fast Fourier Transform (IFFT) and Surface Plots

To bring back the responses to the spatial and time domains, an inverse transformation is needed. 3D-Move uses a two-dimensional Fourier transform because time, *t*, and longitudinal direction, *x*, are interconnected due to the assumption that load moves at constant speed. Therefore, for a specific response point, summations over response contributions of waves corresponding to *x*-direction (longitudinal direction towards which the load moves) and *y*-direction (horizontal direction perpendicular to the travel direction) is performed to obtain the response(s) of interest. In 3D-FAST formulation, however, since a general dynamic load is modeled (which does not necessarily have constant moving speed) a three-dimensional Fourier transform is applied, so summations are made over response contributions of waves corresponding to *x*-, *y*-, and *t*-directions at a particular location and time. if a similar 3D-Move iteration scheme is used in 3D-

FAST, it will be computationally time consuming, and if the response(s) are needed at multiple locations within pavement structure, the runtime will be substantially high.

In the current study, employing the inverse Fourier Transform algorithm was proposed to transform the responses from the frequency domain to the corresponding spatial and time domains. Inverse Fast Fourier Transform (IFFT) is a time-efficient variant of inverse Fourier transform that can be used to carry out this transformation. Since a three-dimensional (3-D) Fourier transform was employed in 3D-FAST formulation for forward transform to the frequency domain, a 3-D IFFT should be employed for backward transform noting that x, y, and t are the Fourier variables. This inverse transform can be used to obtain the pavement mechanical responses at a specific depth of $z = z_i$. For a specific mechanical responses, say vertical displacement (u_3 or displacement in z-direction), the three-dimensional matrix of frequency contribution values can be generated for each and every wave using the equation presented in **Figure 4.6**. The size of the response matrix in frequency domain will be $M \times N \times K$ where M, N, and K are the number of waves representing the load in x-, y-, and t-directions, respectively. Then IFFT algorithm must be applied on this frequency response matrix to obtain responses in the spatial and time domains as a function of x, y, and t at the depth of $z = z_i$. The computed matrix obtained by the application of IFFT algorithm will be again a three-dimensional matrix. As a result, a surface plot can be generated for the response of interest at each time step. **Figure 5.1** presents a sample surface plot of pavement surface vertical displacement under a quad axle load at a specific time step.

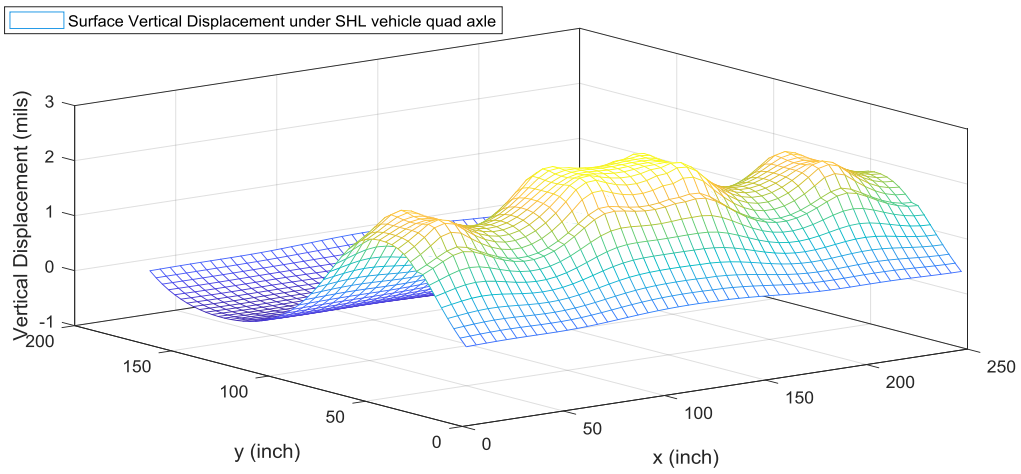

Figure 5.1. Illustration. Sample surface plot of pavement surface vertical displacement under a quad axle load obtained using Inverse Fast Fourier Transform (IFFT).

5.3 Parallel Processing

Parallel processing is a mechanism to improve runtime by assigning computational tasks to different processing units (Rauber & Rünger, 2013). Since 3D-FAST formulation is based on the decomposition of the dynamic load into waves and processing them independently, parallel processing can be used effectively to improve the model runtime. Therefore, (frequency) values of the response(s) of interest could be determined by assigning waves to different processing units. Finally, these responses are collected from all the processing units and assembled so that IFFT algorithm can be applied on the assembled matrix.

There are two general schemes associated with parallelization of an algorithm: *synchronous* parallelization and *asynchronous* parallelization. In a synchronous

parallelization, different tasks are assigned to the processors in a way that certain computational tasks are attributed to each and every processor. At the end of each iteration of the algorithm, the processed computational tasks are collected from all the processors, which will be used in the next algorithm iteration. Depending on the processing capacity of different processing units and the computational load assigned to them, some processors may need to wait for other processors until all processors complete their assigned computational tasks. The synchronous parallelization is of significant use if the output of the algorithm in one step is the input for the next step. Generally speaking, synchronous parallelization is used when the algorithm is seeking convergence through iterations but at each iteration, the computational tasks are parallelizable.

In asynchronous parallelization, a portion of overall computational tasks are initially assigned to the processing units. Thereafter, once a processing unit is done with the assigned computational tasks, additional tasks will be assigned to that processing unit regardless of the status of other processing units. The asynchronous parallelization is an efficient parallelization scheme if the iteration (or sometimes simulation) steps are completely independent. In other words, the results of one iteration is not prerequisite for any other iterations, and all the iteration steps are computationally independent. One tangible example for efficiently using the asynchronous parallelization is the Monte-Carlo simulations (D. D. Batioja-Alvarez et al., 2018; Coleri & Harvey, 2011; Hand & Epps, 2000). In this simulation technique, all the simulation (iteration) steps are

computationally independent so that an asynchronous parallelization can be effectively incorporated.

In 3D-FAST formulation, all the waves can be processed independently since the *linear* viscoelastic conditions are assumed to be the case. This means that it is legitimate to apply the superposition principle in the 3D-FAST formulation. It worth mentioning that while in the time domain the behavior of a viscoelastic material at a certain time step is dependent on its loading history (see equation presented in **Figure 4.1**) but in frequency domain, this dependency is vanished since the convolution integral is replace with simple multiplication (see equation presented in **Figure 4.2**). This is the key to the independency of waves in frequency domain from a computational standpoint (as described by the equation presented in **Figure 4.4**). Therefore, *asynchronous* parallelization can be effectively incorporated into 3D-FAST formulation which is the direct result of conducting calculations in frequency domain.

A number of measures can be used to evaluate the efficiency of parallel computing. The speed-up factor is a measure which is calculated based on the equation presented in **Figure 5.2** assuming that *n* processing units are used to be incorporated in 3D-FAST implementation using parallel computing.

$$S(n) = \frac{T(1)}{T(n)}$$

Figure 5.2. Equation. Speed-up factor of parallel computing.

In this equation, $T(1)$ is the runtime using one processing unit (i.e., no parallel computing), $T(n)$ is the runtime considering *n* processing units are contributing in a parallelized algorithm, and *S*(*n*) is the speed-up factor.

The parallel efficiency is the speed-up factor divided by the number of processors calculated by the equation presented in **Figure 5.3**. If an algorithm is theoretically fully parallelizable, a parallel efficiency of 100% will be achieved.

$$E(n) = \frac{S(n)}{n} \times 100$$

Figure 5.3. Equation. Parallel efficiency in parallel computing.

In this equation, $E(n)$ is the parallel efficiency in percent. While a 100% parallel efficiency is not feasible in practice, one can obtain the portion of an algorithm (e.g., 3D-FAST model algorithm) that is serial (i.e., non-parallelizable) using Amdahl's law (Rauber & Rünger, 2013). Based on this law, one can assume that *B* is the portion of the algorithm that is non-parallelizable and does not benefit from using additional computational resources in a parallel computing architecture. If *B* = 0, then the algorithm is fully serial, and parallel efficiency (*E*) would be equal to (100 / *n*) percent. If *B* = 1, then the algorithm is fully parallelizable and *E* would be 100%. However, in practice *B* is between 0 and 1 for most of the algorithms. Assuming $T(1)$ is the runtime of the algorithm on one processing unit (i.e., no parallel computing included), the runtime can be considered as sum of serial and parallel portions as presented in **Figure 5.4**.

$$T(1) = \underbrace{B \times T(1)}_{Serial} + \underbrace{(1 - B) \times T(1)}_{Parallel}$$

Figure 5.4. Equation. Decomposing the algorithm runtime into serial and parallel portions.

All the parameters used in this equation are as previously defined. If *n* processing units are used in a parallel computing architecture, the algorithm runtime can be estimated by using the equation presented in **Figure 5.5**.

$$T(n) = B \times T(1) + \frac{(1 - B) \times T(1)}{n}$$

Figure 5.5. Equation. Estimating algorithm runtime using *n* processing units.

All the parameters in this equation are as previously defined. This equation is basically the mathematical representation of the Amdahl's law and can be used to identify the portion of the algorithm that is parallelizable or serial. Furthermore, if additional processing units are questioned to be used, the runtime can be estimated by employing this equation.

5.4 Linear Time-Invariant (LTI) Property

3D-FAST is a linear viscoelastic (LVE) model so that the superposition principal can be applied considering the effect of time on pavement mechanical responses. The superposition principal for a linear time-invariant (LTI) system is represented by

convolution integral (see the equation presented in **Figure 4.1**). The convolution integral simplifies to multiplication in the frequency domain (see the equation presented in **Figure 4.2**). The unit load (Dirac delta function) has the important property of equally (i.e., with the same amplitude) exciting all the frequencies. Thus, the pavement mechanical response(s) of interest can be obtained for the unit load, and then convolved with the desired load to obtain the response of interest under that load. If $\tilde{R}^*(\omega, z_i)$ is the arbitrary response of the pavement system at a depth of $z = z_i$, and $\tilde{H}_R(\omega)$ is the pavement response under Dirac delta function for the same response type and depth, then the pavement response under the actual vehicle load ($\hat{\sigma}_{jz}(\omega)$) can be calculated using the equation presented in **Figure 5.6**. In this equation, ω in parentheses represents the frequency and emphasizes that this equation is in the frequency domain.

$$\tilde{R}^*(\omega, z_i) = \tilde{H}_R(\omega, z_i) \cdot \hat{\sigma}_{jz}(\omega)$$

Figure 5.6. Equation. The superposition principle in frequency domain.

The equation presented in **Figure 5.6** simply states that the superposition of the load in frequency domain is based on the multiplication of the response under unit load by the applied surface load. Another important conclusion derived from this equation is that if the response of the pavement at a certain depth (say z_i) is known for a certain dynamic load, the pavement response for the same response type under unit load can be obtained using this equation. Thereafter, the pavement response at that specific depth can be calculated for the same response type using this equation but for another surface

dynamic load in question. It is essential that both dynamic loading cases must have the same frequencies for all the Fourier variables (i.e., *x*, *y*, and *t*) so that the sampling rate and the number of waves describing the load are the same, which allows for using the equation presented in **Figure 5.6**. It should be noted that since $\tilde{R}^*(\omega)$ is in frequency domain, an inverse transformation is needed to obtain the response in the spatial and time domains for the response of interest at a specific depth of z_i. As explained in detail in **Section 5.2**, IFFT is a time efficient and practical approach for this objective.

The superposition principal characterized by the equation presented in **Figure 5.6** is highly effcient since the pavement structure can be analyzed only once under Dirac delta (unit) load. This analysis is basically comprised of calculating the unknown coefficients of the displacement function (see the equation presented in **Figure 4.14**) for all the harmonics obtained by the decomposition of the unit load, and subsequently computing the contribution of those harmonics to the response of interest in frequency domain in order to assemble the $\tilde{H}_R(\omega, z_i)$ matrix. Once this matrix is assembled, the pavement response under each arbitrary load can be determined in a substantially short period of time (typically few seconds) with no need to run the 3D-FAST analysis again.

5.5 Non-uniform Fourier transform

Parallel processing was introduced as a means of improving runtime. While parallel processing does not influence the obtained results whatsoever (compared to no parallel computing architecture) it can substantially decrease 3D-FAST runtime depending on the number of processing units used in the analysis procedure. Another method to reduce the

runtime is using non-uniform Fourier transform method which may be integrated with parallel processing and the LTI property of the pavement system. In this method, the unit load (Dirac delta function) is considered as the pavement surface loading. Waves with select frequencies are processed meaning that the unknowns of displacement function (equation presented in **Figure 4.14**) are derived for only those select waves instead of the entire spectra, and consequently the response(s) of interest are calculated for these (processed) waves at the desired depth of $z = z_i$ under the unit dynamic load. Consequently, responses in frequency domain are estimated for other waves (i.e., waves that are not processed). This analysis can be integrated with parallel processing to further reduce the runtime. The application of non-uniform Fourier transform introduces some approximation to the obtained pavement mechanical responses.

After pavement structure is analyzed for select frequencies and frequency values of the response(s) of the interest are determined, a three-dimensional interpolation scheme (e.g., 3-D spline interpolation) could be used to obtain the responses in frequency domain for other waves to fill out the $\widetilde{H}_R(\omega, z_i)$ matrix in the equation presented in **Figure 5.6**. Then, this equation is used to obtain the responses in frequency domain under actual load, and consequently in spatial and time domains using inverse Fourier transform. It is crucial to select representative select frequencies upon which the non-uniform Fourier transform is applied. In the current study, a number of different scenarios were examined and eventually it was concluded that if the waves corresponding to wave number 1, 2, 4, 8, and so on (i.e., 2^n) are selected in all the directions (i.e., for spatial

domains and time domain) then the approximation introduced to pavement mechanical responses due to non-uniform Fourier transform would be minimal.

Another forms of improvements can be made to further speed-up the runtime. For instance, a neural network can be trained and responses associated to a specific wave can be obtained by using the network (Ashtiani, Little, & Rashidi, 2018; Khodabandehlou & Fadali, 2017; Khodabandehlou & Fadali, 2018; Khodabandehlou, Pekcan, Fadali, & Salem, 2018). Metaheuristic algorithms such as particle swarm optimization (PSO) and genetic algorithm (GA) can also be used to obtain the responses for the waves that are not processed when using non-uniform Fourier transform (Hasany, Shafahi, & Kazemi, 2013; Tousi & Aznavi, 2015).

In **Chapter 6**, a number of 3D-FAST runs are presented for verification, validation, and application purposes. The unique computational aspects of 3D-FAST are investigated for those cases and results are reported in order to show 3D-FAST is time efficient, and the model runtime could be further reduced by using the methods presented in this chapter.

CHAPTER 6 VERIFICATION, VALIDATION, AND APPLICATION OF 3D-FAST

6.1 Introduction

In the past two chapters, 3D-FAST formulation was explained along with unique computational features associate with this formulation, which are primarily due to the frequency domain calculation of the model. 3D-FAST is basically an extension to 3D-Move with the introduction of time (t) as a separate Fourier variable, which accounts for dynamic loading. 3D-Move formulation is based on the two-dimensional Fourier transform which was explained in **Chapter 3**. In 3D-FAST formulation, however, the dynamic load, and consequently, pavement mechanical responses are represented as *three*-dimensional matrices in frequency domain. Each element of these matrices corresponds to a harmonic with specific spatial and time frequencies. 3D-FAST formulation was explained in detail in **Chapter 4**, and a number of unique computational features resulted directly from employing the frequency domain were presented in **Chapter 5**.

In the current chapter, 3D-FAST is verified and validated. Furthermore, a sample application of 3D-FAST is presented. The verification of 3D-FAST is carried out by comparing the results obtained by 3D-FAST with common rheological (mechanical) models for which a theoretical closed-form solution can be derived. These rheological models are Kelvin's model, Maxwell's model, and Burger model. While these models are generally used for one-dimensional viscoelastic modeling, appropriate modifications

were applied in order to address three-dimensional conditions. Therefore, a comparison can be made between the classical solution for these models and 3D-FAST results. The verification of 3D-FAST is performed in **Section 6.2**.

For validating 3D-FAST, the results of a full-scale test conducted at the University of Nevada Reno were used. The facility is called *Box*, which was used to conduct experiments as part of Federal Highway Administration (FHWA) project contract no. DTFH61-13-c-00014, as well as other research projects. That research project was entitled *Analysis Procedures for Evaluating Superheavy Load Movement on Flexible Pavements*. Experiment No. 3 carried out in that project was used for 3D-FAST validation purposes. 3D-FAST validation process is presented in **Section 6.3**.

The application of 3D-FAST is presented for a roughness-induced dynamic loading. Road roughness induces dynamic load depending on the level of road roughness (irregularities on the pavement surface), vehicle speed, and vehicle suspension system characteristics. A quarter-car simulation was implemented using Simulink® in the MATLAB environment to obtain dynamic load. The dynamic load was then converted into a three-dimensional matrix consistent with 3D-FAST input. A sample pavement was analyzed under the roughness-induced dynamic vehicle load in **Section 6.4**.

6.2 3D-FAST Verification: Rheological Models

The rheological models are used primarily to characterize viscoelastic material properties. Typically, these models are used for one-dimensional cases and are a combination of spring and dashpots in series and/or parallel. In a spring element, the fully

elastic conditions exist and stress-strain relationship is according to Hook's law. For a dashpot element, force is equal to the dashpot constant (η) multiplied by the rate of displacement with respect to time. In this section, 3D-FAST results are compared to the results obtained from rheological models noting that the spring coefficient and dashpot coefficients must be modified for three-dimensional loading conditions according to P-wave or constrained modulus. The constrained modulus is defined as the ratio of stress to strain in the uniaxial strain state. Equation presented in **Figure 6.1** shows the stress-strain relationship considering constrained conditions for uniaxial loading conditions.

$$\sigma_{zz} = M\varepsilon_{zz}$$

Figure 6.1. Equation. Constrained (P-wave) modulus.

In this equation, σ_{zz} is the axial stress, ε_{zz} is the axial strain, and *M* is the constrained modulus. The relationship between *M* and other fundamental mechanical properties of a certain material is presented in **Figure 6.2**.

$$M = \frac{E(1-\upsilon)}{(1+\upsilon)(1-2\upsilon)}$$

Figure 6.2. Equation. Relationship between constrained modulus, Young's modulus, and Poisson's ratio.

In this equation, E is the Young's modulus and ν is Poisson's ratio. While Young's modulus is employed for one-dimensional loading conditions, the constrained modulus is used for three-dimensional conditions but uniaxial loading. Therefore, if the results of the classical solutions for a rheological model are to be compared with 3D-FAST results, the spring and dashpot elements of the model should be modified through multiplying them by the adjustment factor presented in **Figure 6.3**, where *AF* is the adjustment factor.

$$AF = \frac{M}{E} = \frac{(1-\upsilon)}{(1+\upsilon)(1-2\upsilon)}$$

Figure 6.3. Equation. Adjustment factor for application of rheological models to three-dimensional conditions.

In the rest of this section, 3D-FAST results are verified with Kelvin model, Maxwell model, and Burger's model. A mechanical schematic of these models are presented in **Figure 6.4**. In the verification process, a harmonic load with a certain angular frequency is applied on the model. A single layer system is assumed with its viscoelastic characteristics represented by the corresponding rheological model.

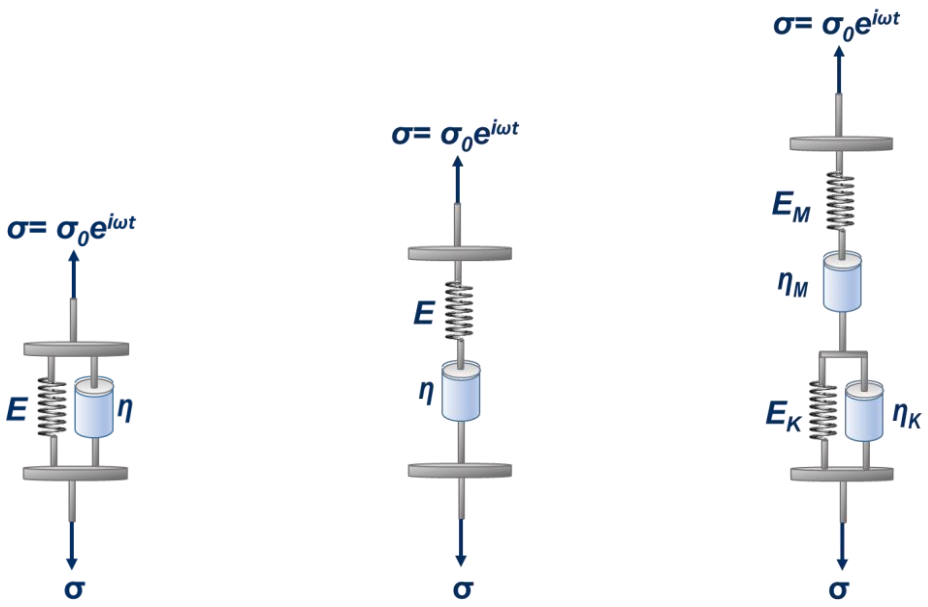

Figure 6.4. Illustration. Schematic of common rheological models: (a) Kelvin, (b) Maxwell, and (c) Burger's.

6.2.1 Kelvin Model

Kelvin model is comprised of a spring element and a dashpot element in parallel. The mechanical schematic of a Kelvin rheological model is presented in **Figure 6.4(a)**. Assuming that a load that varies harmonically with time but is uniform in spatial domain, one can write the stress equation as presented in **Figure 6.5**.

$$\sigma(x, y, t) = \sigma_0 e^{i\omega t}$$

Figure 6.5. Equation. Stress equation applied on a single layer characterized by Kelvin model.

In this equation, $\sigma(x, y, t)$ is the stress function, σ_0 is the stress amplitude, and ω is the angular frequency of the loading time. Longitudinal and transverse directions are denoted by *x* and *y*, respectively (see **Figure 4.3**). Assuming a phase angle of φ, one can write the strain equation for the Kelvin model as presented in **Figure 6.6**.

$$\varepsilon(x, y, t) = \varepsilon_0 e^{i(\omega t - \varphi)}$$

Figure 6.6. Equation. Strain equation assumed for a single layer characterized by Kelvin model.

In this equation, $\varepsilon(x, y, t)$ is the strain function and ε_0 is the strain amplitude. Stress induced by Kelvin model characterization is the sum of stress induced in the spring element and dashpot element, which is mathematically presented in **Figure 6.7**.

$$\sigma(x, y, t) = E \cdot \varepsilon(x, y, t) + \eta \cdot \dot{\varepsilon}(x, y, t)$$

Figure 6.7. Equation. Stress function for Kelvin model as sum of stress induced in the spring and dashpot elements.

In this equation, $\dot{\varepsilon}(x, y, t)$ is the rate of strain change with time. Furthermore, *E* and η are spring constant and dashpot constant, respectively (see **Figure 6.4(a)**). By replacing equation presented in **Figure 6.6** in the equation presented in **Figure 6.7**, the equation presented in **Figure 6.8** will be derived.

$$\sigma_0 \cdot e^{i\varphi} = \eta\varepsilon_0(i\omega) + E\varepsilon_0$$

Figure 6.8. Equation. Relationship between stress and strain amplitude.

If the corresponding real and imaginary parts of the equation presented in this figure are put equal, two equalities are derived as presented in **Figure 6.9**, noting that according to the Euler's formula, $e^{i\varphi} = cos\varphi + i \cdot sin\varphi$.

$$\begin{cases} \sigma_0 \cdot cos\varphi = E\varepsilon_0 \\ \sigma_0 \cdot i \cdot sin\varphi = \varepsilon_0(i\omega) \end{cases}$$

Figure 6.9. Equation. Equalities obtained from equilibrium of real and imaginary parts of stress using Kelvin model.

By dividing these two equalities, the phase angle of the Kelvin model under harmonic loading can be derived, which is presented in **Figure 6.10**. Furthermore, if these two equalities are squared and then summed, the strain amplitude can be derived, which is presented in **Figure 6.11**.

$$\tan(\varphi) = \frac{\eta\omega}{E} \rightarrow \boxed{\varphi = tan^{-1}\left(\frac{\eta\omega}{E}\right)}$$

Figure 6.10. Equation. Phase angle for Kelvin model under harmonic loading.

$$\sigma_0^2 = E^2\varepsilon_0^2 + \eta^2\varepsilon_0^2\omega^2 \rightarrow \boxed{\varepsilon_0 = \frac{\sigma_0}{\sqrt{E^2 + (\eta\omega)^2}}}$$

Figure 6.11. Equation. Strain amplitude for Kelvin model under harmonic loading.

The equations presented in **Figure 6.10** and **Figure 6.11** are basically the theoretical solutions for phase angle and strain amplitude, respectively, when Kelvin model is used for viscoelastic material characterization. These values are compared against those obtained from 3D-FAST for verification purposes. In the 3D-FAST run, the dynamic modulus associated with Kelvin model is calculated using the equation presented in **Figure 6.12** noting that adjusted (constrained) values must be used for spring constant and dashpot constant in this equation.

$$E^*(\omega) = E + i\eta\omega$$

Figure 6.12. Equation. Strain amplitude for Kelvin model under harmonic loading.

In this equation, $E^*(\omega)$ is the dynamic modulus as a function of angular frequency of the loading time and all the other parameters are as previously defined. In order to verify 3D-FAST with Kelvin model, a single layer was assumed with its material characterized by a Kelvin model. The spring constant of the Kelvin model was considered to be constant (E = 300 MPa) while the dashpot constant was assigned values of decades in the range of $\eta = 10^6$ Pa.s to $\eta = 10^{13}$ Pa.s. **Table 6.1** summarizes the

parameters used in the verification process of 3D-FAST using Kelvin model. The verification is conducted for a single wave (i.e., harmonic). However, since any arbitrary dynamic loading can be decomposed into a set of harmonics using discrete Fourier transform, the verification can be conducted for one wave, and then generalized to the set of waves constituting the actual load. The strain amplitude and phase angles are presented in **Figure 6.13** for both results obtained by 3D-FAST and theoretical solution, using the equations presented in **Figure 6.10** and **Figure 6.11**, respectively. This figure demonstrates a perfect match between 3D-FAST and theoretical results. Based on this figure, as the dashpot constant increases, the phase angle increases as well. The adjustment factor for spring and dashpot constants is 4.33 using the equation presented in **Figure 6.3**. Therefore, the *constrained* values for spring and dashpot constants must be used in the equations presented in **Figure 6.10** and **Figure 6.11** to calculate phase angle (φ) and strain amplitude (ε_0), respectively. The data used to produce **Figure 6.13** is presented in **Table 6.2**. This data also includes a no dashpot scenario for which the Kelvin model reduces to a spring element which is representative of a linear elastic layer with a phase angle of $\varphi = 0°$ (fully elastic conditions). The phase angle asymptotically reaches to $\varphi = 90°$ (fully viscous conditions) as the dashpot constant increases towards infinity. The strain amplitude decreases by increasing dashpot constant, and this increase is substantial for higher values of dashpot constant. Based on the data presented in **Table 6.2** and the graph presented in **Figure 6.13**, 3D-FAST was successfully verified using Kelvin rheological model.

Table 6.1. 3D-FAST Parameters for Verification Using Kelvin Model.

Parameter	Symbol	Context	Value	Unit
Stress Amplitude	σ_0	Loading	700	kPa
Load Angular Frequency	ω	Loading	1.0	rad/s
Spring Constant	E	Kelvin Model	300 MPa	MPa
Dashpot Constant	η	Kelvin Model	10^6 to 10^{13}	Pa.s
Poisson's ratio	ν	Pavement Structure	0.35	-
Layer Thickness	H	Pavement Structure	1.0	m
Number of waves in x-direction	M	3D-FAST modeling	512	-
Number of waves in y-direction	N	3D-FAST modeling	512	-
Number of waves in t-direction	K	3D-FAST modeling	512	-

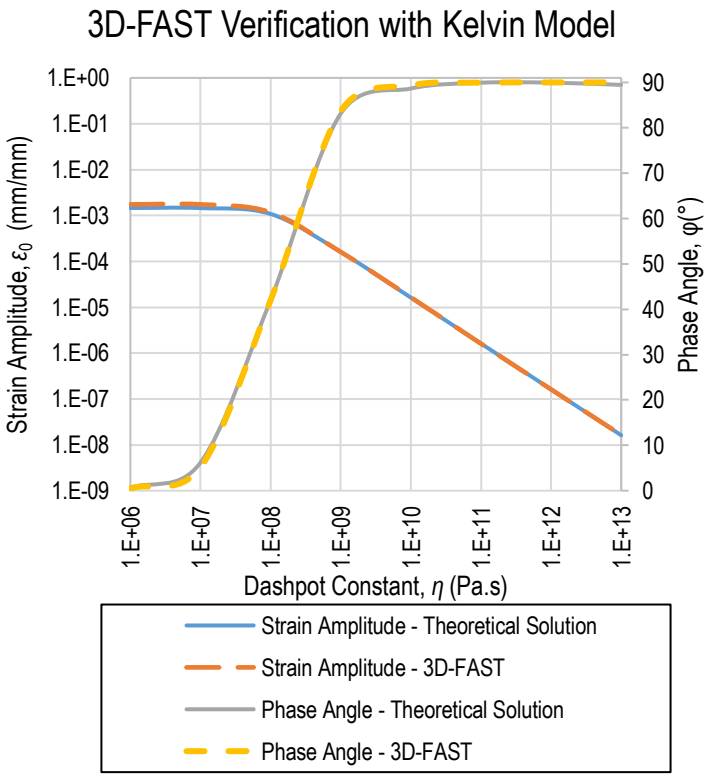

Figure 6.13. Graph. 3D-FAST verification with Kelvin model by comparing strain amplitude and phase angle under harmonic loading of a single wave.

Table 6.2. 3D-FAST Verification Data Using Kelvin Model.

					3D-FAST		Theoretical Solution for Kelvin Model	
Spring Constant, E (Pa)	**Dashpot Constant, η (Pa.s)**	**Poisson's Ratio, ν**	**Constraint Spring Constant (Pa)**	**Constraint Dashpot Constant (Pa.s)**	**Strain Amplitude, ε_0 (mm/mm)**	**Phase Angle, φ ($^\circ$)**	**Strain Amplitude, ε_0 (mm/mm)**	**Phase Angle, φ ($^\circ$)**
3.00E+08	0.00E+00	0.35	4.81E+08	0.00E+00	1.7030E-03	0.00	1.4538E-03	0.00
3.00E+08	1.00E+06	0.35	4.81E+08	4.33E+06	1.7409E-03	0.61	1.4537E-03	0.52
3.00E+08	1.00E+07	0.35	4.81E+08	4.33E+07	1.7438E-03	6.18	1.4479E-03	5.14
3.00E+08	1.00E+08	0.35	4.81E+08	4.33E+08	1.1698E-03	42.04	1.0806E-03	41.99
3.00E+08	1.00E+09	0.35	4.81E+08	4.33E+09	1.6014E-04	83.13	1.6055E-04	83.66
3.00E+08	1.00E+10	0.35	4.81E+08	4.33E+10	1.6501E-05	88.65	1.6152E-05	89.36
3.00E+08	1.00E+11	0.35	4.81E+08	4.33E+11	1.5989E-06	89.93	1.6153E-06	89.94
3.00E+08	1.00E+12	0.35	4.81E+08	4.33E+12	1.6134E-07	89.95	1.6153E-07	89.99
3.00E+08	1.00E+13	0.35	4.81E+08	4.33E+13	1.6365E-08	89.46	1.6153E-08	90.00

6.2.2 Maxwell Model

Maxwell model is comprised of a spring element and a dashpot element in series. A mechanical schematic of the Maxwell model is presented in **Figure 6.4(b)**. Assuming a load that varies harmonically with time but is uniform in spatial domain, one can write the stress equation as previously presented in **Figure 6.5**. In a similar approach as presented in **Section 6.2.1** for Kelvin model, the strain equation can be defined in the same way as the equation presented in **Figure 6.6**. While in the Kelvin model, stress amplitude is sum of stress induced in the spring and dashpot elements, in the Maxwell model, the strain amplitude would be sum of the strains induced in those elements, which is mathematically presented in **Figure 6.14**.

$$\varepsilon(x,y,t) = \varepsilon_S(x,y,t) + \varepsilon_D(x,y,t)$$

Figure 6.14. Equation. Strain amplitude describe as the summation of spring element strain and dashpot element strain using Maxwell model.

In this equation, ε_S and ε_D are strain induced in the spring element and dashpot element, respectively. By differentiating both side of this equation with respect to time and employing stress-strain relationship for spring and dashpot elements, the equation presented in **Figure 6.15** will be derived.

$$\dot{\varepsilon}(x,y,t) = \dot{\varepsilon}_S(x,y,t) + \dot{\varepsilon}_D(x,y,t) = \frac{\dot{\sigma}(x,y,t)}{E} + \frac{\sigma(x,y,t)}{\eta}$$

Figure 6.15. Equation. Strain rate as a function of applied stress and model parameters for Maxwell model.

In this equation, the dot symbol presents derivation with respect to time (rate of change) and all the other parameters are as previously defined. By replacing the equations presented in **Figure 6.5** and **Figure 6.7** in the equation presented in **Figure 6.15**, one can obtain the stress amplitude. The detailed calculations for deriving strain amplitude of the Maxwell model is presented in **Figure 6.16**.

$$\varepsilon_0(i\omega)\cdot e^{i\omega t}\cdot e^{-i\varphi} = \frac{\sigma_0(i\omega)\cdot e^{i\omega t}}{E} + \frac{\sigma_0\cdot e^{i\omega t}}{\eta} \rightarrow \varepsilon_0(i\omega) = \frac{\sigma_0(i\omega)}{E}\cdot e^{i\varphi} + \frac{\sigma_0}{\eta}\cdot e^{i\varphi}$$

$$\rightarrow \varepsilon_0(i\omega) = \frac{\sigma_0(i\omega)}{E}(cos\varphi + i\cdot sin\varphi) + \frac{\sigma_0}{\eta}(cos\varphi + i\cdot sin\varphi)$$

$$\rightarrow \varepsilon_0(i\omega) = \underbrace{\left[\frac{\sigma_0(i\omega)}{E}cos\varphi + \frac{\sigma_0}{\eta}i\cdot sin\varphi\right]}_{Imaginary} + \underbrace{\left[\frac{-\sigma_0\omega}{E}sin\varphi + \frac{\sigma_0}{\eta}cos\varphi\right]}_{Real}$$

Figure 6.16. Equation. Obtaining the strain amplitude for Maxwell model.

If the real and imaginary parts of both sides in the last equation presented in **Figure 6.16** are put equal, the phase angle and strain amplitude of a Maxwell model under harmonic loading can be derived. Noting that the left hand side of this equation does not have a real part, the real part of the right hand side of this equation must be equal to zero. Thus, the Maxwell model phase angle is as presented in **Figure 6.17**. The cosine and sine values of the phase angle can also be calculated using the equations presented in **Figure 6.18** and **Figure 6.19**, respectively.

$$\frac{\sigma_0\omega}{E} = \frac{\sigma_0}{\eta} \rightarrow \tan(\varphi) = \frac{E}{\eta\omega} \rightarrow \boxed{\varphi = tan^{-1}\left(\frac{E}{\eta\omega}\right)}$$

Figure 6.17. Equation. Phase angle for Maxwell model under harmonic loading.

$$\cos(\varphi) = \frac{\eta\omega}{\sqrt{E^2 + (\eta\omega)^2}}$$

Figure 6.18. Equation. Cosine of phase angle for Maxwell model under harmonic loading.

$$\sin(\varphi) = \frac{E}{\sqrt{E^2 + (\eta\omega)^2}}$$

Figure 6.19. Equation. Sine of phase angle for Maxwell model under harmonic loading.

If the imaginary parts of the sides of the last equation presented in **Figure 6.16** are put equal, the strain amplitude of Maxwell model can be derived, which is presented in **Figure 6.20**.

$$\varepsilon_0\omega = \frac{\sigma_0\omega}{E}cos\varphi + \frac{\sigma_0}{\eta}sin\varphi \rightarrow \boxed{\varepsilon_0 = \frac{\sigma_0}{\sqrt{E^2 + (\eta\omega)^2}}\left(\frac{\eta\omega}{E} + \frac{E}{\eta\omega}\right)}$$

Figure 6.20. Equation. Strain amplitude for Maxwell model under harmonic loading.

The equations presented in **Figure 6.17** and **Figure 6.20** can be used as the theoretical solutions for phase angle and strain amplitude, respectively, for Maxwell model viscoelastic material characterization under harmonic loading. It should be noted that the constrained values for spring constant and dashpot constant must be used when using these equations. These constrained values are obtained by applying the adjustment factor introduced by the equation presented in **Figure 6.3**.

The stress-strain relationship for a Maxwell model can also be represented by an ordinary differential equation (ODE). ODE corresponding to a Maxwell rheological model is presented in **Figure 6.21** where all the parameters are as previously defined. The ODE representation of a Maxwell rheological model is useful if appropriate resources are available to solve it.

$$\sigma + \frac{\eta}{E}\dot{\sigma} = \eta\dot{\varepsilon}$$

Figure 6.21. Equation. ODE representation of stress and strain for a Maxwell model.

In order to verify 3D-FAST with Maxwell model, the dynamic modulus of Maxwell model is as presented in **Figure 6.22**. In this equation, the elastic (real) part and viscous (imaginary) part of the dynamic modulus are demonstrated.

$$E^*(\omega) = \underbrace{\frac{E\eta^2\omega^2}{\eta^2\omega^2 + E^2}}_{Elastic\ Modulus} + i \cdot \underbrace{\frac{\eta E^2\omega}{\eta^2\omega^2 + E^2}}_{Viscous\ (Loss)\ Modulus}$$

Figure 6.22. Equation. Dynamic modulus of a material characterized by Maxwell rheological model

3D-FAST verification with Maxwell model was conducted using the parameters presented in **Table 6.3**. The load was assumed to change harmonically with time, and uniform in the spatial domain for a certain time. A single layer was considered for the pavement structure with a thickness of 1.0 m. All the other parameters used in the verification process are presented in **Table 6.3**.

Table 6.3. 3D-FAST Parameters for Verification Using Maxwell Model.

Parameter	Symbol	Context	Value	Unit
Stress Amplitude	σ_0	Loading	700	kPa
Load Angular Frequency	ω	Loading	10.0	rad/s
Spring Constant	E	Maxwell Model	300	MPa
Dashpot Constant	η	Maxwell Model	10^6 to 10^{13}	Pa.s
Poisson's ratio	ν	Pavement Structure	0.35	-
Layer Thickness	H	Pavement Structure	1.0	m
Number of waves in *x*-direction	M	3D-FAST modeling	512	-
Number of waves in *y*-direction	N	3D-FAST modeling	512	-
Number of waves in *t*-direction	K	3D-FAST modeling	512	-

The results of 3D-FAST verification with Maxwell model are presented in **Figure 6.23**. In this figure, the theoretical strain amplitude and phase angles are presented, which are calculated by using the equation presented in **Figure 6.17** and **Figure 6.20**, respectively. In addition, the 3D-FAST results are also presented. The results shows a perfect match between 3D-FAST and theoretical solution. **Table 6.4** summarizes the data used to generate **Figure 6.23**. Based on the presented results, 3D-FAST was successfully verified using Maxwell model under harmonic loading. As can be seen in **Figure 6.23**, the strain amplitude and phase angle decrease by increasing dashpot constant of the Maxwell rheological model.

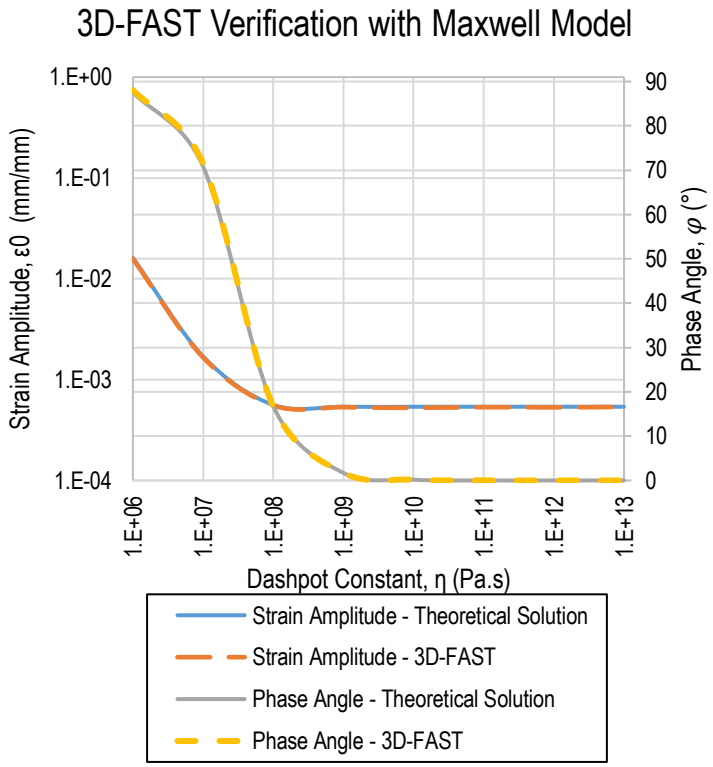

Figure 6.23. Graph. 3D-FAST verification with Maxwell model by comparing strain amplitude and phase angle under harmonic loading of a single wave.

Table 6.4. 3D-FAST Verification Data Using Maxwell Model.

					3D-FAST		Theoretical Solution for Maxwell Model	
Spring constant *E* (Pa)	**Dashpot constant *η* (Pa.s)**	**Poisson's ratio**	**Constraint spring constant (Pa)**	**Constraint dashpot constant (Pa.s)**	**Strain Amplitude, ε_0 (mm/mm)**	**Phase Angle, φ (°)**	**Strain Amplitude, ε_0 (mm/mm)**	**Phase Angle, φ (°)**
300E+08	1.00E+06	0.35	1.30E+09	4.33E+06	0.015777656	87.58	1.616282E-02	88.09
300E+08	1.00E+07	0.35	1.30E+09	4.33E+07	0.001665049	70.85	1.702765E-03	71.57
300E+08	1.00E+08	0.35	1.30E+09	4.33E+08	0.000555179	16.79	5.621704E-04	16.70
300E+08	1.00E+09	0.35	1.30E+09	4.33E+09	0.000532748	1.71	5.387038E-04	1.72
300E+08	1.00E+10	0.35	1.30E+09	4.33E+10	0.000525427	0.17	5.384640E-04	0.17
300E+08	1.00E+11	0.35	1.30E+09	4.33E+11	0.000533281	0.00	5.384616E-04	0.02
300E+08	1.00E+12	0.35	1.30E+09	4.33E+12	0.000530952	0.00	5.384615E-04	0.00
300E+08	1.00E+13	0.35	1.30E+09	4.33E+13	0.000536199	0.00	5.384615E-04	0.00

6.2.3 Burger Model

Burger model is comprised of a Kelvin model and a Maxwell model, connected in series. A mechanical schematic of Burger model is presented in **Figure 6.4(c)**. Burger model has been used in the literature for viscoelastic characterization of asphalt mixtures and mastics (Abbas, Masad, Papagiannakis, & Harman, 2007). The derivation of strain amplitude and phase angle for Burger model needs more effort compared to Kelvin model and Maxwell model. The ODE representation of Burger model stress-strain relationship is presented in **Figure 6.25**.

$$\sigma + p_1\dot{\sigma} + p_2\ddot{\sigma} = q_1\dot{\varepsilon} + q_2\ddot{\varepsilon}$$

Figure 6.24. Equation. ODE representation of stress and strain for the Burger model.

Here, the dot accent represents rate of change with time and the double dot accent is the second derivation with respect to time. p_1, p_2, q_1, and q_2 are function of Burger model properties, which are calculated using the equations presented in **Figure 6.25**.

$$\begin{cases} p_1 = \dfrac{\eta_M}{E_M} + \dfrac{\eta_K}{E_K} + \dfrac{\eta_M}{E_K}, & p_2 = \dfrac{\eta_M \cdot \eta_K}{E_M \cdot E_K} \\ q_1 = \eta_M, & q_2 = \dfrac{\eta_M \cdot \eta_K}{E_K} \end{cases}$$

Figure 6.25. Equation. Calculating Burger model parameters: p_1, p_2, q_1, and q_2.

In these equations, E_M and η_M are spring constant and dashpot constant of the Maxwell component of the Burger model, respectively. Furthermore, E_K and η_K are spring constant and dashpot constant of the Kelvin component of the Burger model, respectively. These constants are also presented in **Figure 6.4(c)**. Assuming the general harmonic form presented in **Figure 6.5** for stress function applied to a single layer characterized by Burger model, the associated strain function would be as presented in **Figure 6.6**. Details for calculating the phase angle is as presented in **Figure 6.26**.

$$\sigma_0 + p_1(i\omega)\sigma_0 + p_2(i\omega)^2\sigma_0 \cdot e^{i\omega t} =\cdot e^{-i\varphi} q_1(i\omega)\varepsilon_0 +\cdot e^{-i\varphi} q_2(i\omega)^2\varepsilon_0$$

$$\rightarrow e^{i\varphi} \cdot \sigma_0(1 + p_1 i\omega - p_2\omega^2) = (q_1 i\omega - q_2\omega^2)\varepsilon_0$$

$$\rightarrow \sigma_0(cos\varphi + i \cdot sin\varphi)(1 + p_1 i\omega - p_2\omega^2) = (q_1 i\omega - q_2\omega^2)\varepsilon_0$$

$$\rightarrow \sigma_0(cos\varphi + p_1 i\omega \cdot cos\varphi - p_2\omega^2 \cdot cos\varphi + i \cdot sin\varphi - p_1\omega \cdot sin\varphi - p_2\omega^2 i \cdot sin\varphi)$$

$$= (q_1 i\omega - q_2\omega^2)\varepsilon_0$$

Figure 6.26. Equation. Calculations associated with obtaining the phase angle for Burger model.

Based on the last equation presented in **Figure 6.26**, if the real and imaginary parts of either sides of the equation are put equal, the set of equations presented in **Figure 6.27** is derived.

$$\begin{cases} \sigma_0(cos\varphi - p_2\omega^2 \cdot cos\varphi - p_1\omega \cdot sin\varphi) = -q_2\omega^2\varepsilon_0 \\ \sigma_0(p_1\omega \cdot cos\varphi + sin\varphi - p_2\omega^2 \cdot sin\varphi) = q_1\omega\varepsilon_0 \end{cases}$$

Figure 6.27. Equation. Obtaining the phase angle for Burger model.

By dividing these two equations, the stress amplitude and strain amplitude can be omitted so that phase angle would be the only unknown. The calculations are followed in the equations presented in **Figure 6.28**.

$$\frac{cos\varphi - p_2\omega^2 \cdot cos\varphi - p_1\omega \cdot sin\varphi}{p_1\omega \cdot cos\varphi + sin\varphi - p_2\omega^2 \cdot sin\varphi} = \frac{-q_2\omega}{q_1}$$

$$\rightarrow \frac{1 - p_2\omega^2 - p_1\omega \cdot tan\varphi}{p_1\omega + tan\varphi - p_2\omega^2 \cdot tan\varphi} = \frac{-q_2\omega}{q_1}$$

$$\rightarrow tan\varphi = \frac{p_2q_1\omega^2 - q_1 - p_1q_2\omega^2}{q_2\omega + p_2q_2\omega^3 - p_1q_1\omega} \rightarrow \boxed{\varphi = tan^{-1}\left(\frac{p_2q_1\omega^2 - q_1 - p_1q_2\omega^2}{q_2\omega + p_2q_2\omega^3 - p_1q_1\omega}\right)}$$

Figure 6.28. Equation. Phase angle for Burger model.

The strain amplitude can be derived by using either of the equations presented in **Figure 6.27**. If the first equation presented in that figure is used, the strain amplitude can be derived as a function of Burger model rheological parameters (p_1, p_2, q_1, and q_2), frequency of loading time, and phase angle. The strain amplitude derivation based on this approach is presented in **Figure 6.29**.

$$\sigma_0(1 - p_2\omega^2 - p_1\omega \cdot tan\varphi) \cdot cos\varphi = -q_2\omega^2\varepsilon_0$$

$$\rightarrow \boxed{\varepsilon_0 = \sigma_0 . cos\varphi \left(\frac{p_1\omega \cdot tan\varphi + p_2\omega^2 - 1}{q_2\omega^2}\right)}$$

Figure 6.29. Equation. Strain amplitude for Burger model.

Alternatively, the second equation presented in **Figure 6.27** could be used to obtain strain amplitude. The creep compliance was used in 3D-FAST verification process as this parameter is available for Burger model in the literature. The creep compliance is the inverse of dynamic modulus in frequency domain. The equation presented in **Figure 6.30** represents the mathematical relationship between creep compliance and dynamic modulus.

$$E^*(\omega) = \frac{1}{J^*(\omega)}$$

Figure 6.30. Equation. Relationship between dynamic modulus and creep compliance in frequency domain.

The creep compliance (same as dynamic modulus) has real and imaginary parts, which are shown in the equation presented in **Figure 6.31**. The equations presented in **Figure 6.31** and **Figure 6.32** correspond to the real and imaginary parts of creep compliance for Burger model, respectively.

$$J^*(\omega) = \underbrace{J_1(\omega)}_{Real\ Part} + i \cdot \underbrace{J_2(\omega)}_{Imaginary\ Part}$$

Figure 6.31. Equation. The real and imaginary parts of creep compliance.

$$J_1(\omega) = \frac{(p_1 q_1 - q_2) + p_2 q_2 \omega^2}{q_1^2 + q_2^2 \omega^2}$$

Figure 6.32. Equation. The real part of creep compliance for Burger model.

$$J_2(\omega) = -\frac{q_1 + (q_2 p_1 - p_2 q_1)\omega^2}{(q_1^2 + q_2^2 \omega^2) \cdot \omega}$$

Figure 6.33. Equation. The imaginary part of creep compliance for Burger model.

All the parameters used in these equations are as previously defined. To verify 3D-FAST with Burger model, a set of nine (9) RTFO-aged mastics were used based on a past study (Abbas et al., 2007). The Burger model parameters for these mastics are presented in **Table 6.5**. The parameters used for loading, pavement structure, and number of waves are presented in **Table 6.6**. Finally, the results obtained by 3D-FAST and theoretical solutions are presented in **Table 6.7** for strain amplitude and phase angle. For theoretical solution, the strain amplitude and phase angle were calculated based on the equation presented in **Figure 6.28** and **Figure 6.29**, respectively. The verification results shows a descent match between 3D-FAST and theoretical solutions, thus, 3D-FAST is successfully verified using Burger model.

Table 6.5. Burger Model Parameters for Nine (9) RTFO-Aged Asphalt Mastics.

Mastic Type	R_M (Pa)	η_M (Pa.s)	R_K (Pa)	η_K (Pa.s)
PG 64-28 (Unmodified)	1354280.5	13408.4	59376.5	21612.9
PG 70-22 (Unmodified)	2255403.6	27454.6	93244.3	34261.7
Elvaloy	587236.4	14988.4	22151.1	9344.4
SBS Linear	764279.5	22813.3	34379.1	12086.5
SBS Linear Grafted	631716.1	26846.7	28567.1	10842.0
SBS Radial Grafted	739829.6	21955.4	29356.2	11240.5
EVA	722214.4	41863.2	33516.7	13479.1
EVA Grafted	800962.7	49063.4	37851.7	15014.4
CMCRA	1480667.2	63408.8	72346.2	26576.0

Table 6.6. Parameters Used for 3D-FAST Verification Using Burger Model.

Parameter	Symbol	Context	Value	Unit
Stress Amplitude	σ_0	Loading	700	kPa
Load Angular Frequency	ω	Loading	6.28	rad/s
Spring Constant of Maxwell Component	E_M	Burger Model Parameter	Varies based on **Table 6.5**	Pa
Spring Constant of Maxwell Component	η_M	Burger Model Parameter	Varies based on **Table 6.5**	Pa.s
Spring Constant of Kelvin Component	E_K	Burger Model Parameter	Varies based on **Table 6.5**	Pa
Spring Constant of Kelvin Component	η_K	Burger Model Parameter	Varies based on **Table 6.5**	Pa.s
Poisson's ratio	v	Pavement Structure	0.35	-
Layer Thickness	H	Pavement Structure	1.0	m
Number of waves in *x*-direction	M	3D-FAST modeling	512	-
Number of waves in *y*-direction	N	3D-FAST modeling	512	-
Number of waves in *t*-direction	K	3D-FAST modeling	512	-

Table 6.7. 3D-FAST Verification Data Using Burger Model.

	3D-FAST		Theoretical Solution for Burger Model	
Mastic type	**Strain Amplitude, ε_0 (mm/mm)**	**Phase Angle, φ (˚)**	**Strain Amplitude, ε_0 (mm/mm)**	**Phase Angle, φ (˚)**
PG 64-28 (Unmodified)	1.0936E-03	66.59	1.12E-03	66.76
PG 70-22 (Unmodified)	5.6174E-04	66.92	5.75E-04	66.94
Elvaloy	1.0223E-03	69.70	1.03E-03	69.66
SBS Linear	6.7615E-04	65.59	6.61E-04	66.03
SBS Linear Grafted	5.3847E-04	67.94	5.26E-04	67.64
SBS Radial Grafted	7.3797E-04	67.77	7.24E-04	67.77
EVA	3.2004E-04	69.07	3.13E-04	68.82
EVA Grafted	2.6398E-04	68.22	2.66E-04	68.55
CMCRA	2.1715E-04	66.68	2.12E-04	67.00

6.3 3D-FAST Validation: The Full-Scale Box Experiment (Experiment No. 3)

As part of the Federal Highway Administration (FHWA) project contract no. DTFH61-13-c-00014, a comprehensive experimental plan was carried out to verify and calibrate the procedures developed for analyzing superheavy load (SHL) vehicle move on flexible pavements. The verification and calibration process of that study was conducted through a total of five (5) experiments using the full-scale pavement/soil testing facility (called *Box* from now on) at the University of Nevada, Reno (UNR) considering typical pavement structures. The details about these experiments are presented in **Table 6.8**. The UNR full-scale test facility is shown in **Figure 6.34**. A three-dimensional (3-D) schematic of this test facility is presented in **Figure 6.35** which includes the dimensions of the Box, as well as the design of walls. The cross section of the Box is a square with a dimension of 124 inch by 124 inch, with a height of 72 inch by default.

Table 6.8. Details about Large-Scale Box Experiment.

Experiment No.	Description[a]	Loading Protocol[b]
1	• SG only (No AC or CAB). • Apply loads on top of SG.	• Apply dynamic loads of different amplitudes simulating the FWD loading for low number of cycles. • Apply increasing static load until failure using 11.9 inch circular steel plate.
2	• Unbound materials only (CAB and SG) • Apply loads on top of the CAB.	• Apply dynamic loads of different amplitudes simulating the FWD loading for low number of cycles. • Apply increasing static load until failure using 11.9 inch circular steel plate.
3	• Control section (full pavement structure: AC, CAB, and SG). • Apply loads on top of the AC layer.	• Apply dynamic loads of different amplitudes simulating the FWD loading for low number of cycles. • Apply increasing static load until failure using 11.9 inch circular steel plate.
4	• Impact of sloped shoulder (Full pavement structure: AC, CAB and SG with 1:1.5 side slope). • Apply loads on top of the AC layer.	• Apply dynamic loads of different amplitudes simulating the FWD loading at three locations: 12, 24 and 36 inch from the edge of the slope. • Apply increasing static load until failure using 11.9 inch circular steel plate.
5	• Impact of loading on two buried utilities (Full pavement structure: AC, CAB and SG). • Apply loads on top of the AC layer at three different locations.	• Apply dynamic loads of different amplitudes simulating the FWD loading for low number of cycles. • Apply increasing static load until failure using 11.9 inch circular steel plate.

[a] AC, CAB, and SG denotes Asphalt Concrete, Crushed Aggregate Base, and Subgrade, respectively.
[b] FWD denotes Falling Weight Deflectometer.

Figure 6.34. Photo. The full-scale pavement/soil testing facility at the University of Nevada Reno.

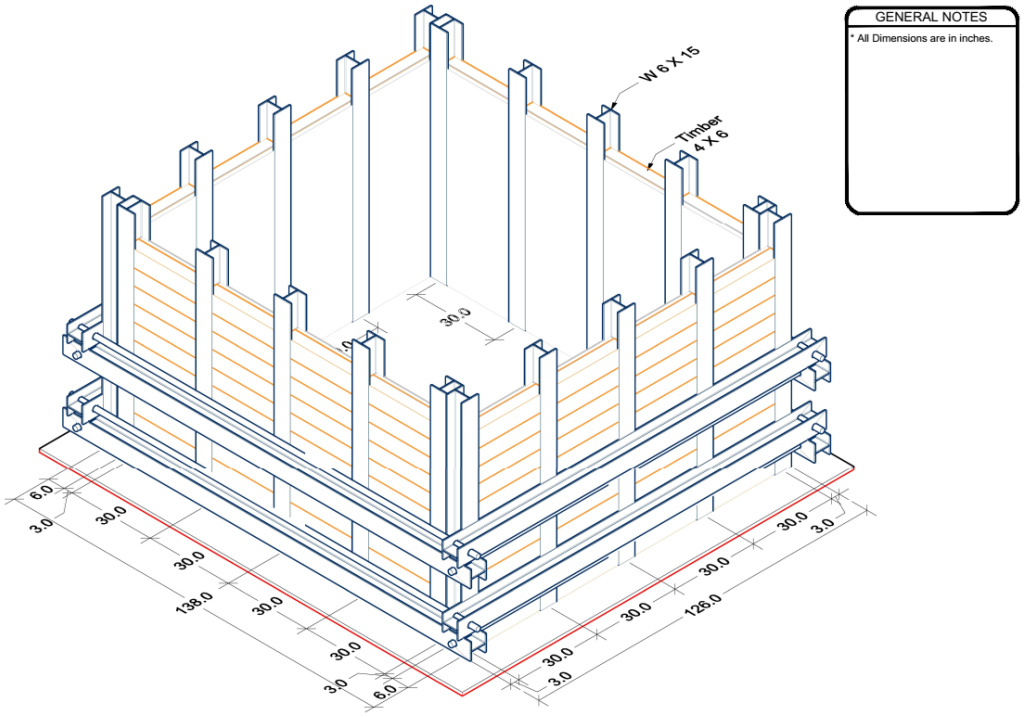

Figure 6.35. Illustration. Three-dimensional (3-D) schematic of the full-scale pavement/soil testing facility at the University of Nevada Reno.

In all the five (5) experiments, a dynamic load was applied on the pavement surface using a hydraulic ram. The dynamic loading protocol was consisted of 0.1 second of loading pulse followed by 0.9 second of resting period, applied on a falling weight deflectometer (FWD) plate. The experiments were instrumented by measuring pavement surface vertical deflection using linear variable differential transformers (LVDTs) at typical FWD measured radial distances. Total Earth Pressure Cells (TEPC) and accelerometers (ACC) were also used to record vertical normal stress and acceleration, respectively, at certain locations of crushed aggregate base (CAB) and subgrade (SG).

According to **Table 6.8**, typical pavement structures were constructed in experiment no. 1, 2, and 3, noting that experiment no. 3 included the full set of typical layers considered in a flexible pavement design (i.e., asphalt concrete or AC, CAB and SG). The objective of conducting experiment no. 4 and no. 5 was to scrutinize the influence of sloped-shoulder and buried utilities, respectively, upon the move of SHL. Therefore, experiment no. 3 was considered as the control experiment. This experiment was used for validation of 3D-FAST. Noting that 3D-FAST is capable of modeling layered structures under dynamic loading, experiments no. 4 and no. 5 are not appropriate candidates for 3D-FAST validation purposes as experiment no. 4 is not layered (i.e., all the interfaces are not horizontal) and experiment no. 5 violates the medium continuity criteria dictated by 3D-FAST formulation (due to buried utility). Therefore, experiment no. 3 was selected for the purpose of validating 3D-FAST. In the rest of this section, this experiment is briefly described, associated instrumentation is presented, and 3D-FAST results are compared and validated with the results obtained by the instrumentation.

6.3.1 Box Experiment No. 3

A full pavement structure was fabricated in the Box experiment no. 3 consisted of 5 inch of asphalt concrete (AC), on top of 6 inch of CAB, on top of 66 inch of SG soil. **Figure 6.36** provides a close view of this experiment. The loading protocol was 25 cycles of dynamic load (0.1 second loading plus followed by 0.9 second rest period), applied on an 11.9 inch Dynatest FWD loading plate. Details about the loading protocol is presented in **Table 6.9**. The load levels were 9000, 12000, 16000, 21000, and 27000 pound. **Table 6.10** presents pavement structure, material characterization, and parameters needed for modeling the experiment in 3D-FAST. A PG64-22 dense graded hot-mix asphalt (HMA) was used as the AC layer. The dynamic modulus test was performed on AC layer specimen at temperatures of 40, 70, 100, and 130°F, and at frequencies of 0.1, 0.5, 1, 5, 10, and 25 Hz. The dynamic modulus and phase angle values for this mixture are presented in **Table 6.11** and **Table 6.12**, respectively. The dynamic modulus (E^*) master curve along with its elastic (E') and viscous (E'') components are presented in **Figure 6.37**.

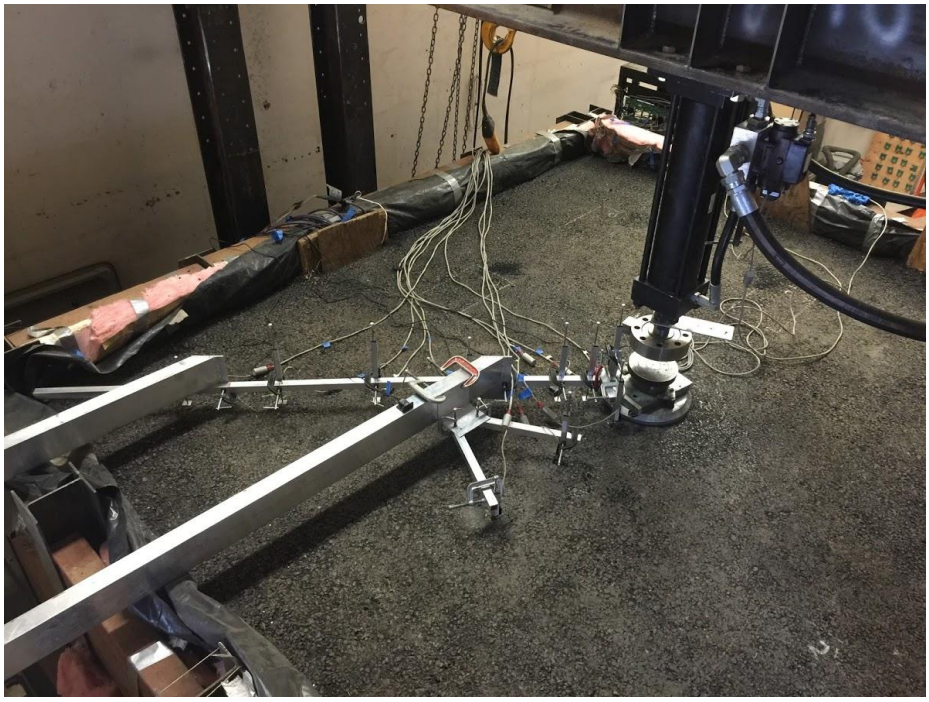

Figure 6.36. Photo. A close view of experiment no. 3 performed at the University of Nevada Reno.

Table 6.9. Loading Protocol for Experiment No. 3 (Full Pavement Structure).

Load Type	Target Load Amplitude (lb)	Loading Cycles	Load Plate Diameter (inch)	Rest Period Between Load Levels
Dynamic Load (0.1 second Loading plus 0.9 second Rest Period)	9,000	25 Cycles	11.9 (Dynatest FWD Loading Plate)	2 Minutes

Table 6.10. Material Characterization and Parameters Needed for 3D-FAST Modeling of Experiment No. 3.

Layer	Thickness, h (inch)	Material Characterization	Poisson's Ratio	Unit Weight, γ (pcf)
Asphalt Concrete (AC)	5	Viscoelastic	0.30	148
Crushed Aggregate Based (CAB)	6	Elastic	0.35	138.2
Subgrade (SG) Soil	66	Elastic	0.40	125.5

Table 6.11. Dynamic Modulus Values for a Typical Dense-Grade HMA with PG64-22 Asphalt Binder.

Temperature (°F)	Dynamic Modulus, *E** (psi)					
	0.1 Hz	0.5 Hz	1 Hz	5 Hz	10 Hz	25 Hz
40	693,889	1,012,294	1,163,463	1,530,813	1,690,524	1,898,005
70	141,296	262,736	334,941	554,052	670,382	842,418
100	21,439	45,076	61,705	123,984	164,420	233,925
130	4,025	7,934	10,801	22,592	31,147	47,465

Table 6.12. Phase Angle Values for a Typical Dense-Grade HMA with PG64-22 Asphalt Binder.

Temperature (°F)	Phase Angle (Degrees)					
	0.1 Hz	0.5 Hz	1 Hz	5 Hz	10 Hz	25 Hz
40	22.1	19.0	17.3	15.5	15.9	18.1
70	31.2	29.8	30.1	27.8	27.4	26.3
100	28.5	29.9	31.3	35.0	35.5	36.8
130	23.2	26.8	27.0	33.9	34.1	40.1

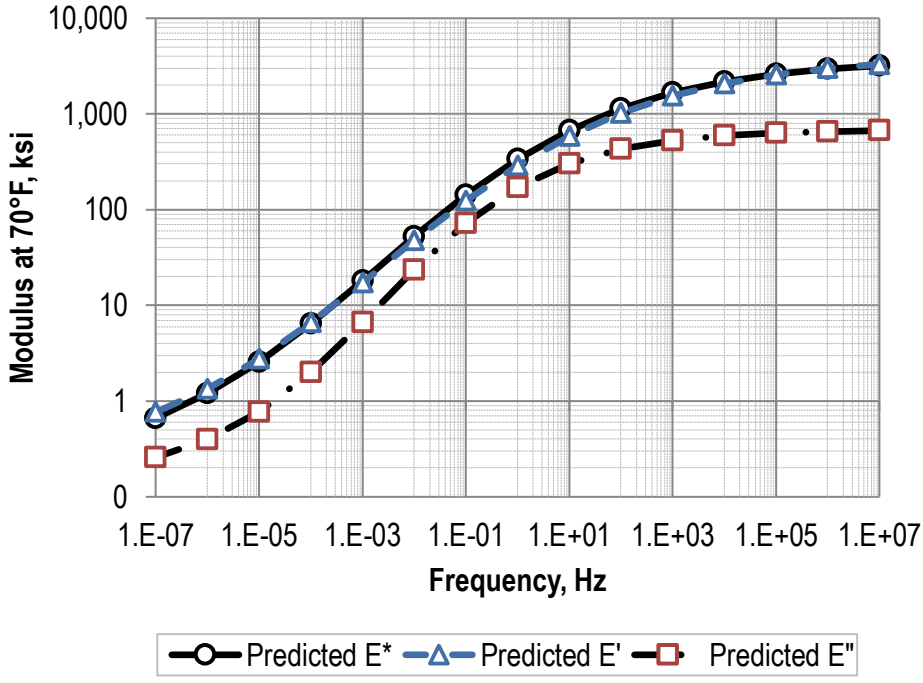

Figure 6.37. Graph. Dynamic modulus master curve (*E) along with its elastic (*E'*) and viscous (*E"*) parts.**

6.3.2 Instrumentation

An extensive instrumentation plan was implemented for Box experiment no. 3. The details about the instrumentation for this test is graphically presented in **Figure 6.38**. The origin of the Cartesian system was located at the bottom of the Box with the positive *z*-direction heading to the pavement surface (see **Figure 6.38**). The horizontal directions are represented by *x* and *y*. Therefore, the coordinates of the center of loading plate is (0 inch, 0 inch, 77 inch) in the (*x*, *y*, *z*) Cartesian system. The list of instruments used in the Box experiment no. 3 is presented in **Table 6.13** along with the location of embedment in Cartesian and polar systems. The instrumentation of this test included the following:

- LVDT: At the pavement surface, installed diagonally, to measure surface deflections at various radial distances (0, 8, 12, 24, 36, 48, and 60 inch). These LVDTs are tagged by L1 to L7 in **Figure 6.38**.

- TEPC: The pressure cells were located in the middle of CAB, as well as at a depth of 6 inch below subgrade surface. Furthermore, one pressure cell was placed at the centerline of the load at a depth of 20 inch below subgrade. Four (4) pressure cells were placed at mid-depth CAB at the centerline of the load and at radial distances of 0, 12, 24, and 36 inch from the centerline of the load. Five (5) pressure cells were placed at the centerline of the load and at a radial distance of 12, 24, 48, and 60 inch from the centerline of the load.

- ACC: accelerometers were placed at the pavement surface, mid-depth CAB, and 6 inch below subgrade surface. The accelerometers were not used in the validation process of 3D-FAST.

The measured vertical surface displacement (measured by LVDTs) and vertical stress (measured by TEPCs) for different load levels are presented in **Table 6.14** and **Table 6.15**, respectively. These measurements are later used in the process of 3D-FAST validation. The measured pavement surface deflections by LVDTs for different load levels and at different radial distances are presented in **Figure 6.39**.

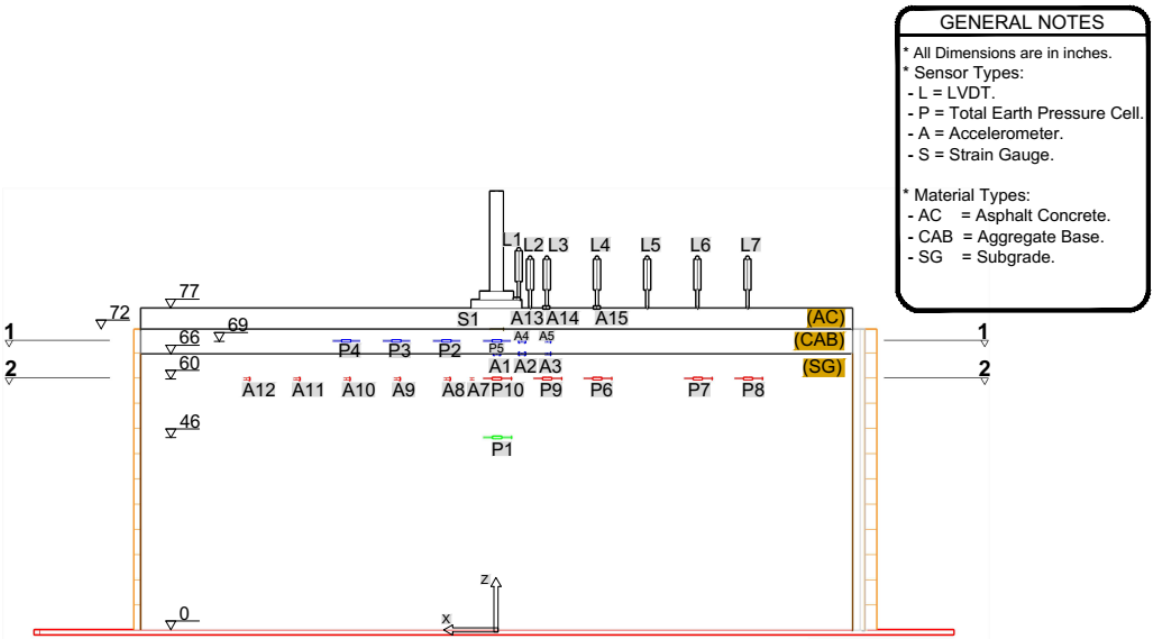

Figure 6.38. Illustration. Side view of experiment no. 3 and associated instrumentation.

Table 6.13. Instrumentation List of LVDTs, TEPCs, and ACCs Used in the Box Experiment No. 3.

Experiment No. 3 - Instruments List														
No.	Tag	Sensor Name	Brand	Capacity	Spec.	Coordinates						ID / SN	No. of Ch.	Notes
						r	θ	Z	X	Y	Z			
						in (mm)	°	in (mm)	in (mm)	in (mm)	in (mm)			
1	L1	$(L_{AC})_{77-0}$	Novotechnik	100 mm	TR-0100	0 (0)	228 °	77 (0)	0 (0)	0 (0)	77 (0)		1	Surface LVDT
2	L2	$(L_{AC})_{77-8}$	Novotechnik	100 mm	TR-0100	8 (203)	228 °	77 (0)	-5.3 (-135)	-6 (-152)	77 (0)		1	Surface LVDT
3	L3	$(L_{AC})_{77-12}$	Novotechnik	100 mm	TR-0100	12 (305)	228 °	77 (0)	-8 (-203)	-9 (-229)	77 (0)		1	Surface LVDT
4	L4	$(L_{AC})_{77-24}$	Novotechnik	100 mm	TR-0100	24 (610)	228 °	77 (0)	-15.9 (-404)	-17.9 (-455)	77 (0)		1	Surface LVDT
5	L5	$(L_{AC})_{77-36}$	Novotechnik	100 mm	TR-0100	36 (914)	228 °	77 (0)	-23.9 (-607)	-26.9 (-683)	77 (0)		1	Surface LVDT
6	L6	$(L_{AC})_{77-48}$	Novotechnik	100 mm	TR-0100	48 (1219)	228 °	77 (0)	-31.9 (-810)	-35.9 (-912)	77 (0)		1	Surface LVDT
7	L7	$(L_{AC})_{77-60}$	Novotechnik	100 mm	TR-0100	60 (1524)	228 °	77 (0)	-39.9 (-1013)	-44.8 (-1138)	77 (0)		1	Surface LVDT
8	P1	$(P_{SG})_{46-0}$	Geokon	600 kPa	4" cell	0 (0)	0 °	46 (787)	0 (0)	0 (0)	46 (787)	1404682	1	Pressure Cell (Vertical)
9	P2	$(P_{AB})_{69-12}$	Geokon	250 kPa	4" cell	12 (305)	228 °	69 (203)	-8 (-203)	-9 (-229)	69 (203)	1330825	1	Pressure Cell (Vertical)
10	P3	$(P_{AB})_{69-24}$	Geokon	250 kPa	4" cell	24 (610)	228 °	69 (203)	-15.9 (-404)	-17.9 (-455)	69 (203)	1330822	1	Pressure Cell (Vertical)
11	P4	$(P_{AB})_{69-36}$	Geokon	250 kPa	4" cell	36 (914)	228 °	69 (203)	-23.9 (-607)	-26.9 (-683)	69 (203)	1330827	1	Pressure Cell (Vertical)
12	P5	$(P_{AB})_{69-0}$	Geokon	2.5 MPa	4" cell	0 (0)	228 °	69 (203)	0 (0)	0 (0)	69 (203)	1533652	1	Pressure Cell (Vertical)
13	P6	$(P_{SG})_{60-24}$	Geokon	600 kPa	4" cell	24 (610)	48 °	60 (432)	15.9 (404)	17.9 (455)	60 (432)	1427206	1	Pressure Cell (Vertical)
14	P7	$(P_{SG})_{60-48}$	Geokon	600 kPa	4" cell	48 (1219)	48 °	60 (432)	31.9 (810)	35.9 (912)	60 (432)	1427204	1	Pressure Cell (Vertical)
15	P8	$(P_{SG})_{60-60}$	Geokon	600 kPa	4" cell	60 (1524)	48 °	60 (432)	39.9 (1013)	44.8 (1138)	60 (432)	1427205	1	Pressure Cell (Vertical)
16	P9	$(P_{SG})_{60-12}$	Geokon	600 kPa	4" cell	12 (305)	48 °	60 (432)	8 (203)	9 (229)	60 (432)	1404681	1	Pressure Cell (Vertical)
17	A1	$(A_{AB})_{66-0}$	Vernier	(± 5 g)	3-Axis	0 (0)	228 °	66 (279)	0 (0)	0 (0)	66 (279)		1	Accelerometer
18	A2	$(A_{AB})_{66-6}$	Vernier	(± 5 g)	3-Axis	6 (152)	228 °	66 (279)	-4 (-102)	-4.5 (-114)	66 (279)		1	Accelerometer
19	A3	$(A_{AB})_{66-12}$	Vernier	(± 5 g)	3-Axis	12 (305)	228 °	66 (279)	-8 (-203)	-9 (-229)	66 (279)		1	Accelerometer
20	A4	$(A_{AB})_{69-6}$	Vernier	(± 5 g)	3-Axis	6 (152)	228 °	69 (203)	-4 (-102)	-4.5 (-114)	69 (203)		1	Accelerometer
21	A5	$(A_{AB})_{69-12}$	Vernier	(± 5 g)	3-Axis	12 (305)	228 °	69 (203)	-8 (-203)	-9 (-229)	69 (203)		1	Accelerometer
22	A6		Vernier	(± 5 g)	3-Axis								1	Accelerometer
23	A7	$(A_{SG})_{60-6}$	Vernier	(± 5 g)	3-Axis	6 (152)	48 °	60 (432)	4 (102)	4.5 (114)	60 (432)		1	Accelerometer
24	A8	$(A_{SG})_{60-12}$	Vernier	(± 5 g)	3-Axis	12 (305)	48 °	60 (432)	8 (203)	9 (229)	60 (432)		1	Accelerometer
25	A9	$(A_{SG})_{60-24}$	Vernier	(± 5 g)	3-Axis	24 (610)	48 °	60 (432)	15.9 (404)	17.9 (455)	60 (432)		1	Accelerometer
26	A10	$(A_{SG})_{60-36}$	Vernier	(± 5 g)	3-Axis	36 (914)	48 °	60 (432)	23.9 (607)	26.9 (683)	60 (432)		1	Accelerometer
27	A11	$(A_{SG})_{60-48}$	Vernier	(± 5 g)	3-Axis	48 (1219)	48 °	60 (432)	31.9 (810)	35.9 (912)	60 (432)		1	Accelerometer
28	A12	$(A_{SG})_{60-60}$	Vernier	(± 5 g)	3-Axis	60 (1524)	48 °	60 (432)	39.9 (1013)	44.8 (1138)	60 (432)		1	Accelerometer
29	A13	$(A_{AC})_{77-6}$	Vernier	(± 5 g)	3-Axis	6 (152)	228 °	77 (0)	-4 (-102)	-4.5 (-114)	77 (0)		1	Accelerometer
30	A14	$(A_{AC})_{77-12}$	Vernier	(± 5 g)	3-Axis	12 (305)	228 °	77 (0)	-8 (-203)	-9 (-229)	77 (0)		1	Accelerometer
31	A15	$(A_{AC})_{77-24}$	Vernier	(± 5 g)	3-Axis	24 (610)	228 °	77 (0)	-15.9 (-404)	-17.9 (-455)	77 (0)		1	Accelerometer
32	A16	$(A_{RF})_{66+}$	Vernier	(± 5 g)	3-Axis	-	-	-	-	-	-		1	Frame Accelerometer

Table 6.14. Vertical Surface Displacement Measurements for Experiment No. 3 at Different Load Levels.

Load Level (lb)		Vertical Surface Displacements (inch)						
Target	Average Applied	LVDT1	LVDT2	LVDT3	LVDT4	LVDT5	LVDT6	LVDT7
9,000	8,971	0.01811	0.01117	0.00773	0.00475	0.00280	0.00281	0.00140
12,000	11,857	0.02683	0.01687	0.01179	0.00755	0.00342	0.00349	0.00171
16,000	15,860	0.04099	0.02729	0.02162	0.01274	0.00536	0.00392	0.00382
21,000	21,146	0.05772	0.04192	0.03305	0.02048	0.00880	0.00628	0.00458
27,000	27,087	0.07976	0.05763	0.04482	0.02908	0.01124	0.00697	0.00577

Table 6.15. Vertical Stress Measurements in Experiment No. 3 at Different Load Levels.

Load Level (lb)		Vertical Stress (psi)					
Target	Average Applied	TEPC1	TEPC3	TEPC5	TEPC6	TEPC9	TEPC10
9,000	8,971	2.9	1.5	11.1	1.9	3.9	6.9
12,000	11,857	4.0	2.0	15.3	2.5	5.2	9.6
16,000	15,860	5.6	2.7	22.0	3.4	7.1	13.7
21,000	21,146	7.7	3.6	32.4	4.6	9.8	19.3
27,000	27,087	10.4	4.4	46.5	5.7	12.7	26.5

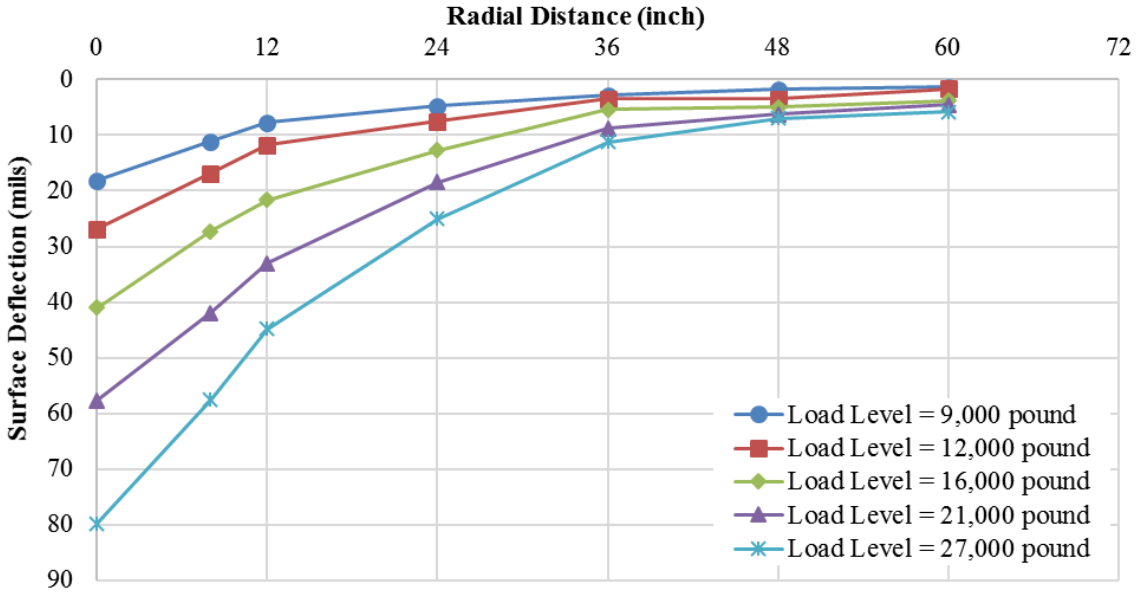

Figure 6.39. Graph. Vertical surface deflection at different load levels for different radial distances.

6.3.3 3D-FAST Inputs and Validation Data

3D-FAST validation was performed at the load level of 9,000 pound as it is typically used in pavement design and distress condition evaluation. Appropriate inputs must be considered in 3D-FAST including pavement structure, material characteristics, and dynamic surface loading. The pressure induced on the FWD plate was measured by the instrumentation mounted on the hydraulic ram. The applied dynamic load for load level of 9,000 pound is presented in **Figure 6.40**. The frequency of recording the applied load on the FWD plate was 1,024 data points per second. In 3D-FAST, the number of waves in the time domain was considered to be K = 128 to ensure that the details of the load are sufficiently captured, without a significant influence on the model runtime. **Figure 6.41** presents one loading pulse with a duration of 1.0 second, which consists of 0.1 second loading period and 0.9 second rest period. In this figure, the points at which 3D-FAST sampling was conducted is also shown.

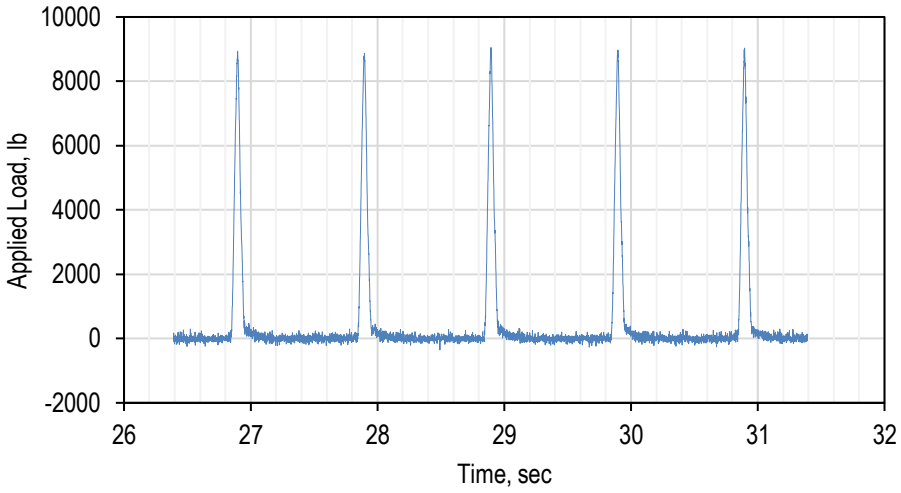

Figure 6.40. Graph. Applied dynamic load for load level of 9,000 pound.

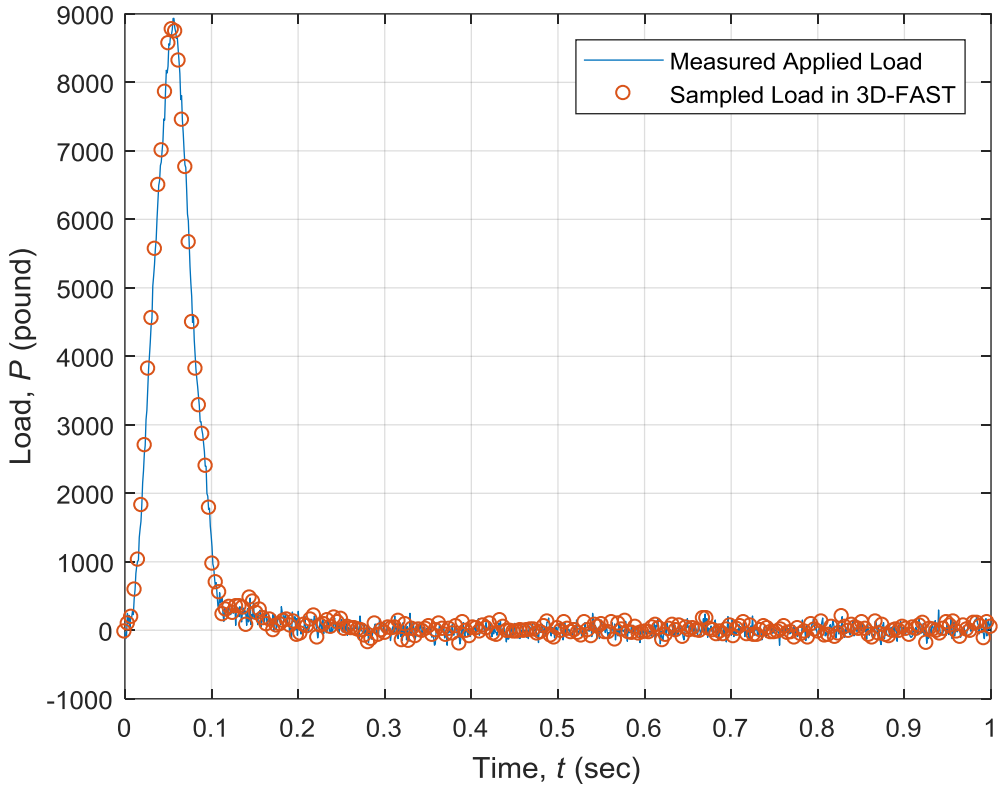

Figure 6.41. Graph. Applied dynamic load and sampled load in 3D-FAST for load level of 9,000 pound.

In 3D-FAST, AC layer was characterized as viscoelastic layer based on the complex modulus and phase angle data presented in **Table 6.11** and **Table 6.12**, respectively. The pavement surface temperature was about 75°F at the test time. The same analysis temperature was considered for AC layer, thus AC dynamic modulus master curve was shifted for this temperature. Other material properties needed for 3D-FAST analysis are presented in **Table 6.10**. CAB and SG were characterized as linear elastic with a modulus obtained from backcalculation process. Backcalculated moduli for CAB and SG is presented in **Table 6.16**. The backcalculated moduli presented in this

table reveals that CAB modulus was almost independent of load levels with a variation between 18,259 and 20,143 psi, while SG exhibited a stress-dependent behavior. For the load level of 9,000 pound used in 3D-FAST validation, a modulus of 20,143 psi and 18,453 psi were considered for CAB and SG, respectively.

Table 6.16. Backcalculated Moduli for CAB and SG at Different Load Levels.

	Moduli used in 3D-FAST based on the backcalculation at different load levels, E_{CAB}, E_{SG} (psi)				
Layer	**9,000 pound**	12,000 pound	16,000 pound	21,000 pound	27,000 pound
CAB	**20,143**	19,061	18,259	19,531	20,398
SG	**18,453**	16,860	13,098	10,000	7,529

The 3D-FAST runs were performed at three depths so that the results can be compared with those of LVDTs and pressure cells:

1. pavement surface to estimate vertical deflection
2. mid-depth CAB to estimate vertical normal stress at a depth of eight (8) inch from pavement surface
3. six (6) inch below subgrade surface to estimate vertical normal stress

For pavement surface deflections, scrutinizing the recorded LVDT data revealed that L1, L2, L3, and L4 with a radial distance of 8, 12, 24, and 36 inch, respectively, did not show much noise while the other LVDTs did. Therefore, only these LVDTs were used for 3D-FAST validation purposes. **Figure 6.42** presents the measured vertical displacement for these LVDTs corresponding to one (1) loading pulse.

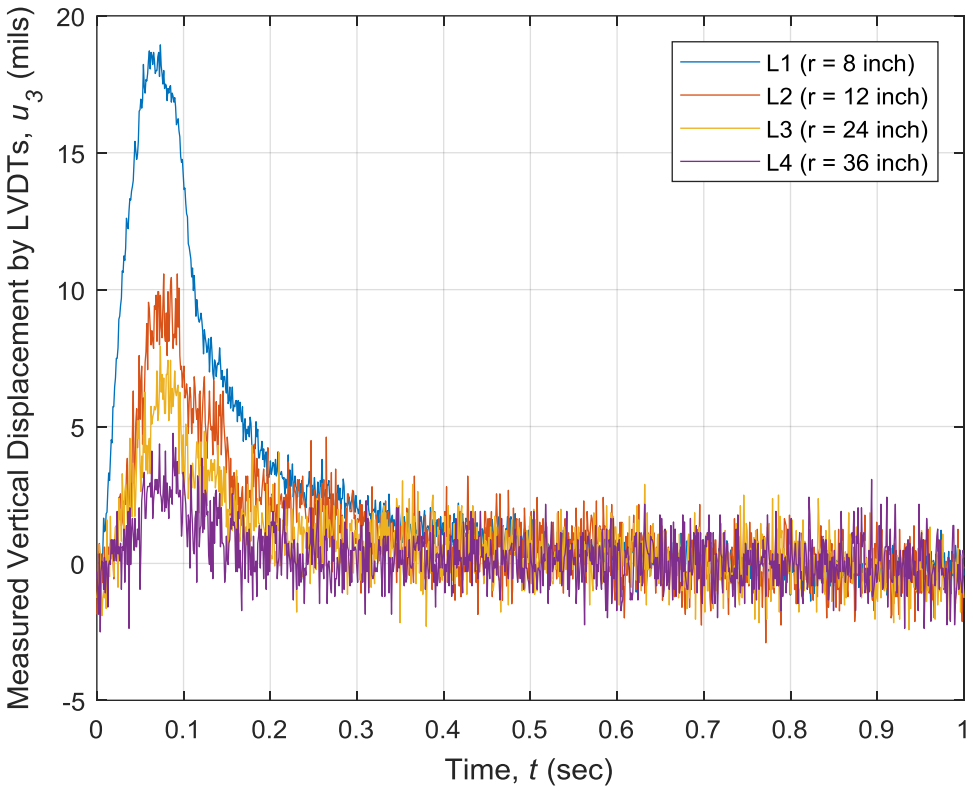

Figure 6.42. Graph. Measured vertical displacement by LVDTs for a loading pulse at the load level of 9,000 pound.

For mid-depth CAB, the recorded pressure cell data for P2, P3, P4, and P5 were used in the validation process. As previously mentioned, these pressure cells are at a depth of eight (8) inch below pavement surface at radial distances of 12, 24, 36, and 0 inch, respectively (see **Figure 6.38** and

Table 6.13). Data recorded by these pressure cells are presented in **Figure 6.43**.

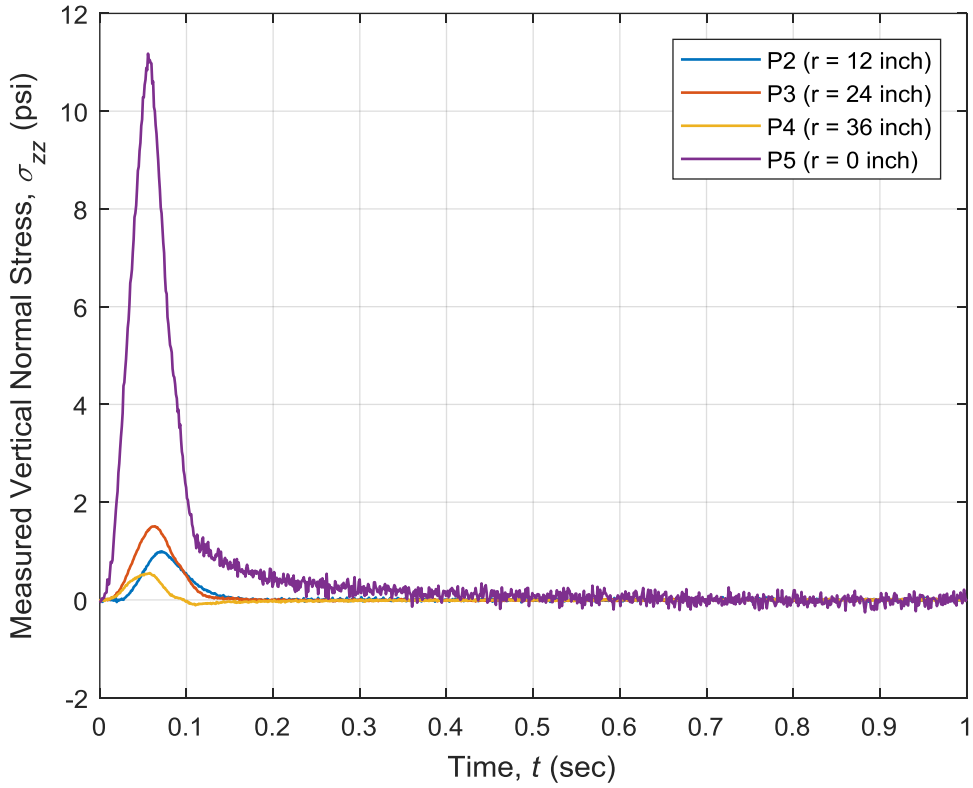

Figure 6.43. Graph. Measured vertical normal stress by pressure cells at mid-depth CAB for a loading pulse at the load level of 9,000 pound.

For six (6) inch below subgrade, the recorded pressure cells data for P6, P7, P9, and P10 were used in the validation process, and data recorded from pressure cell P8 was ignored because of observed noise. These pressure cells are embedded at a depth of 17 inch below pavement surface at a radial distance of 24, 48, 12, and 0 inch, respectively (see **Figure 6.38**). Data recorded by these pressure cells are presented in **Figure 6.68**.

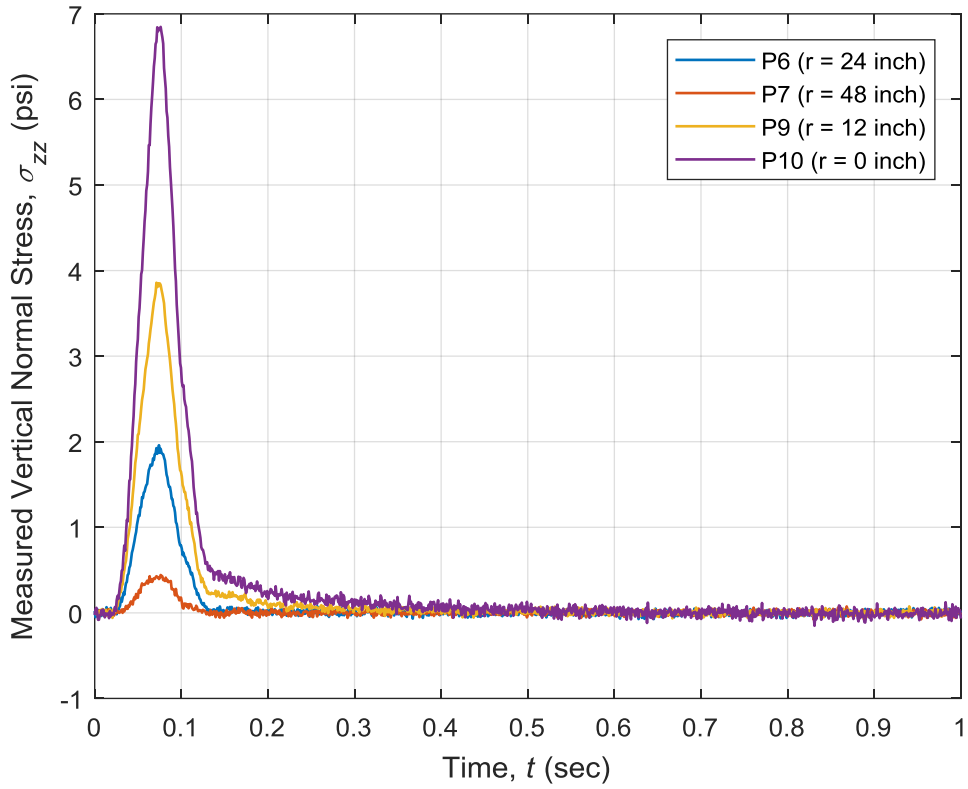

Figure 6.44. Graph. Measured vertical normal stress by pressure cells at six (6) inch below subgrade surface for a loading pulse at the load level of 9,000 pound.

6.3.4 Validation Results

The validation processes was performed by comparing responses computed by 3D-FAST and that of recorded by LVDTs and pressure cells in term of response pulse shape and peak values. **Table 6.17** summarizes the peak values for responses based on 3D-FAST, as well as data recorded by instrumentation (i.e., LVDTs and pressure cells) at respective response points.

Table 6.17. Peak Values Obtained by 3D-FAST and Instrumentation.

Instrumentation	Response Type	Tag	Unit	Depth from Pavement Surface (inch)	Radial Distance from Load Centerline, *r* (inch)	Peak Values	
						3D-FAST	Recorded Instrumentation Data
LVDT (AC Layer)	Vertical Displacement, u_3	L1	mils	0	8	16.31	18.94
		L2	mils	0	12	10.45	10.57
		L3	mils	0	24	8.51	7.93
		L4	mils	0	36	4.09	4.75
Pressure Cells (CAB Layer)	Vertical Normal Stress, σ_{zz}	P2	psi	8	12	5.23	0.99
		P3	psi	8	24	1.20	1.51
		P4	psi	8	36	0.42	0.55
		P5	psi	8	0	12.7	11.18
Pressure Cells (SG Layer)	Vertical Normal Stress, σ_{zz}	P6	psi	17	24	1.47	1.96
		P7	psi	17	48	0.32	0.44
		P9	psi	17	12	3.93	3.86
		P10	psi	17	0	6.02	6.85

For validation of pavement surface vertical displacement (u_3), 3D-FAST results were plotted against those measured by LVDTs. **Figure 6.45**, **Figure 6.46**, **Figure 6.47**, and **Figure 6.48** present this comparison for LVDTs L1, L2, L3, and L4 respectively. Furthermore, the surface plot of pavement surface vertical displacement is presented in **Figure 6.49** at time t = 0.05 second, which is obtained by inverse Fourier transformation. The results of predicted pavement surface vertical displacement by 3D-FAST versus that of the LVDT-measured are presenetd in **Figure 6.50**.

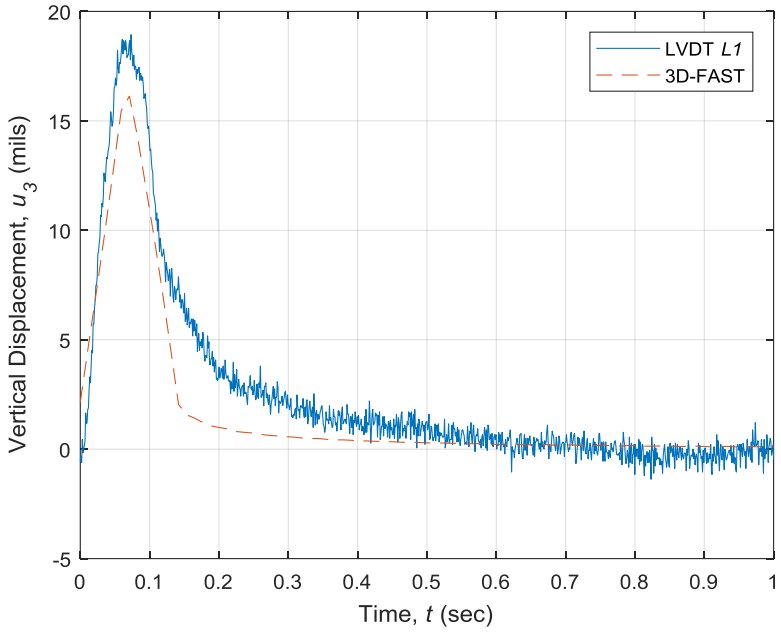

Figure 6.45. Graph. Validation of vertical displacement by comparing 3D-FAST results and measured data by LVDT L1 for one (1) loading pulse at the load level of 9,000 pound.

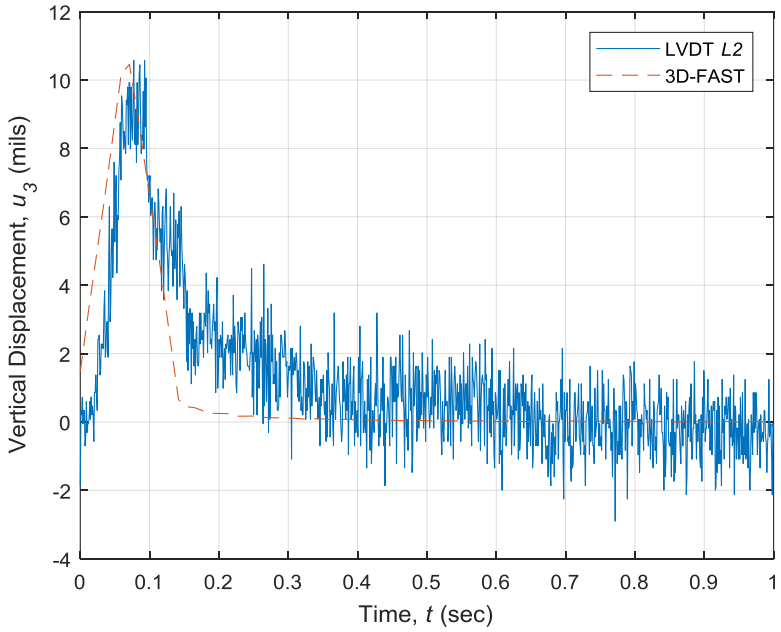

Figure 6.46. Graph. Validation of vertical displacement by comparing 3D-FAST results and measured data by LVDT L1 for one (1) loading pulse at the load level of 9,000 pound.

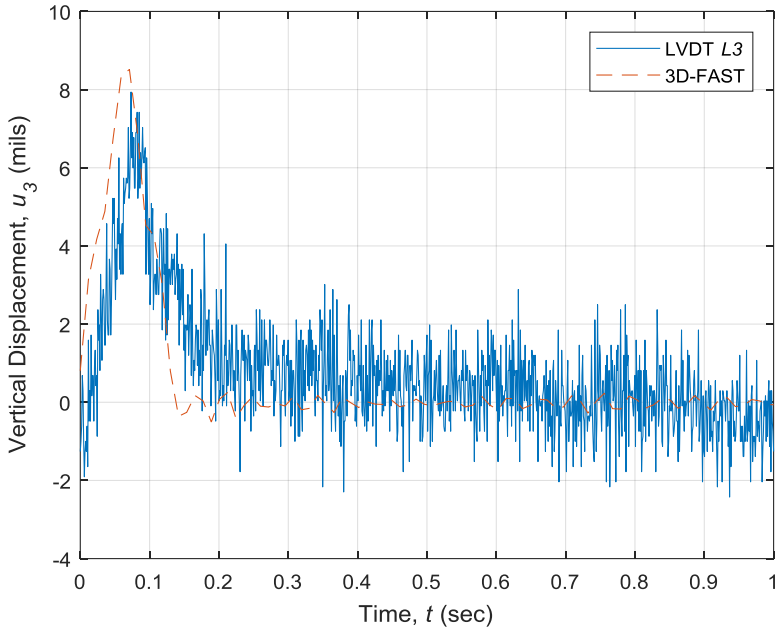

Figure 6.47. Graph. Validation of vertical displacement by comparing 3D-FAST results and measured data by LVDT L3 for one (1) loading pulse at the load level of 9,000 pound.

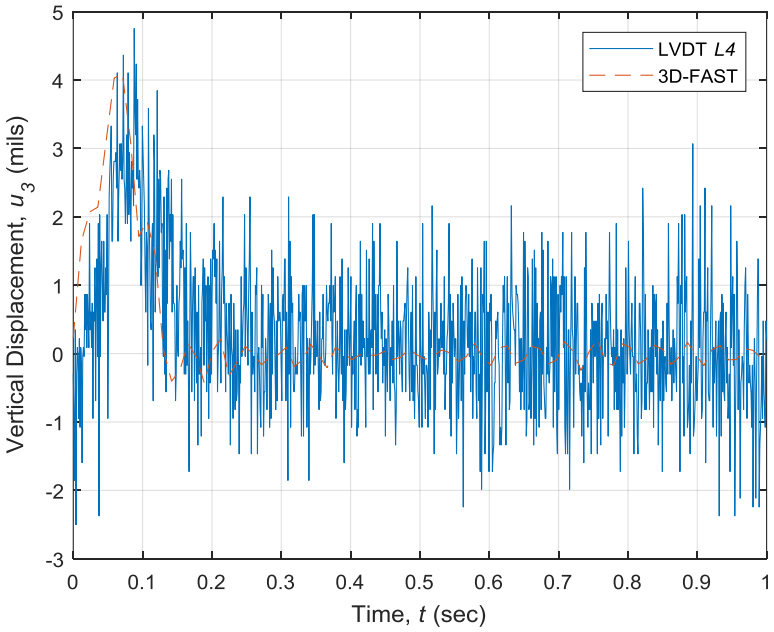

Figure 6.48. Graph. Validation of vertical displacement by comparing 3D-FAST results and measured data by LVDT L4 for one (1) loading pulse at the load level of 9,000 pound.

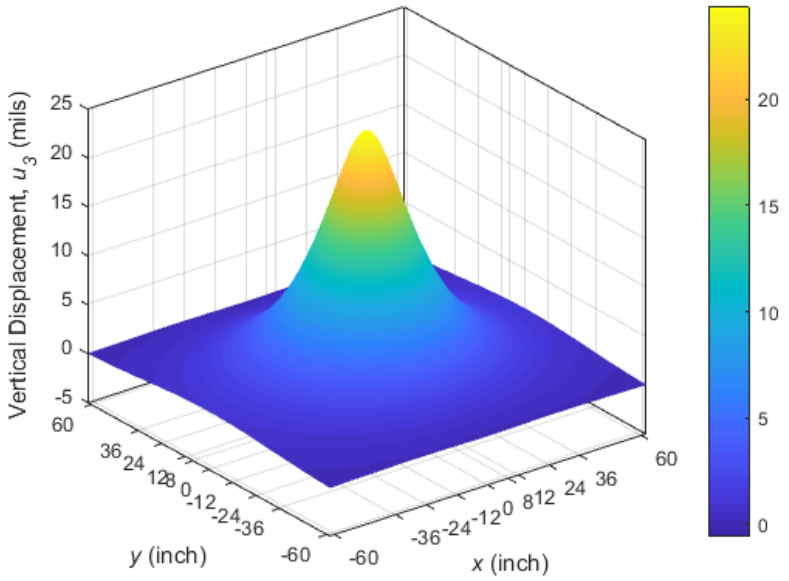

Figure 6.49. Plot. Surface plot for pavement surface vertical displacement at time *t* = 0.05 second computed by 3D-FAST at the load level of 9,000 pound.

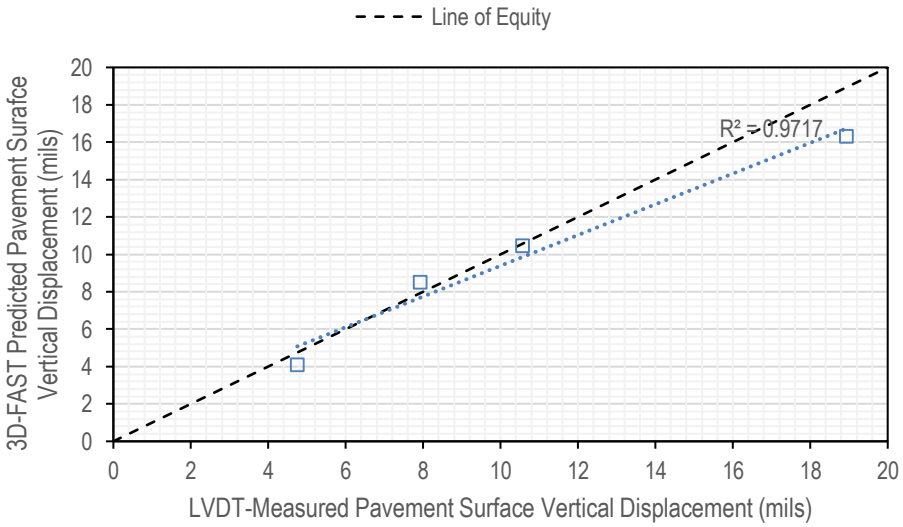

Figure 6.50. Graph. Measured vs. predicted pavement surface displacement at the load level of 9,000 pound.

At the mid-depth CAB, the vertical normal stress was measured by pressure cells placed at a depth of eight (8) inch below pavement surface. For validating pavement responses at mid-depth CAB, vertical normal stress (σ_{zz}) computed by 3D-FAST was plotted against that of recorded by pressure cells. **Figure 6.51**, **Figure 6.69**, **Figure 6.53**, and **Figure 6.54** present this comparison for pressure cells P2, P3, P4, and P5, respectively. Furthermore, the perspective, top, and side views of the surface plot of vertical normal stress is presented in **Figure 6.55**, **Figure 6.56**, and **Figure 6.57**, respectively. The results of predicted mid-depth CAB vertical normal stress computed by 3D-FAST versus that of measured by pressure cells are presented in **Figure 6.61**.

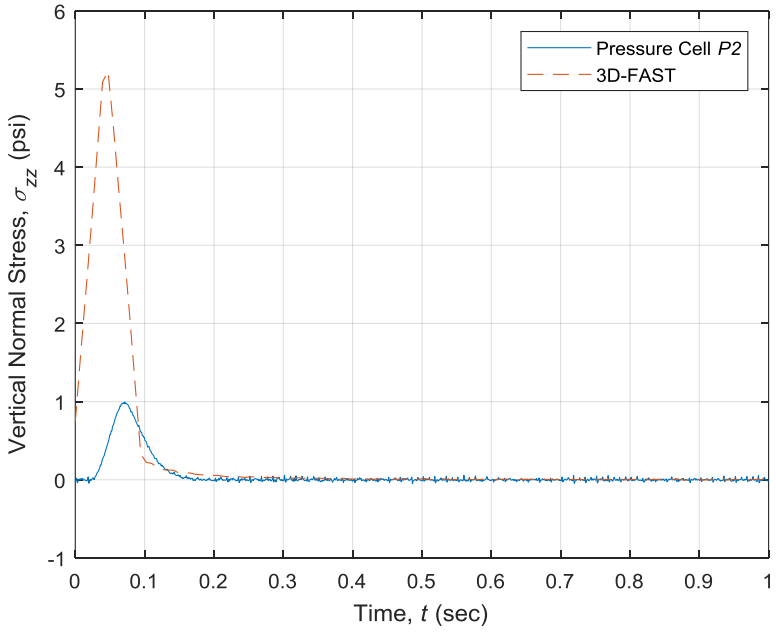

Figure 6.51. Graph. Validation of vertical normal stress at CAB by comparing 3D-FAST results and measured data by pressure cell P2 for one (1) loading pulse at the load level of 9,000 pound.

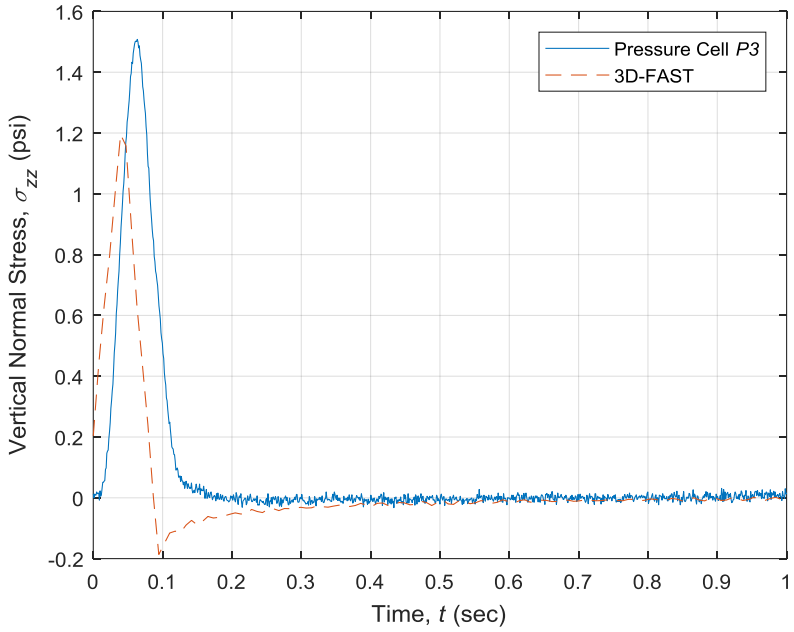

Figure 6.52. Graph. Validation of vertical normal stress at CAB by comparing 3D-FAST results and measured data by pressure cell P3 for one (1) loading pulse at the load level of 9,000 pound.

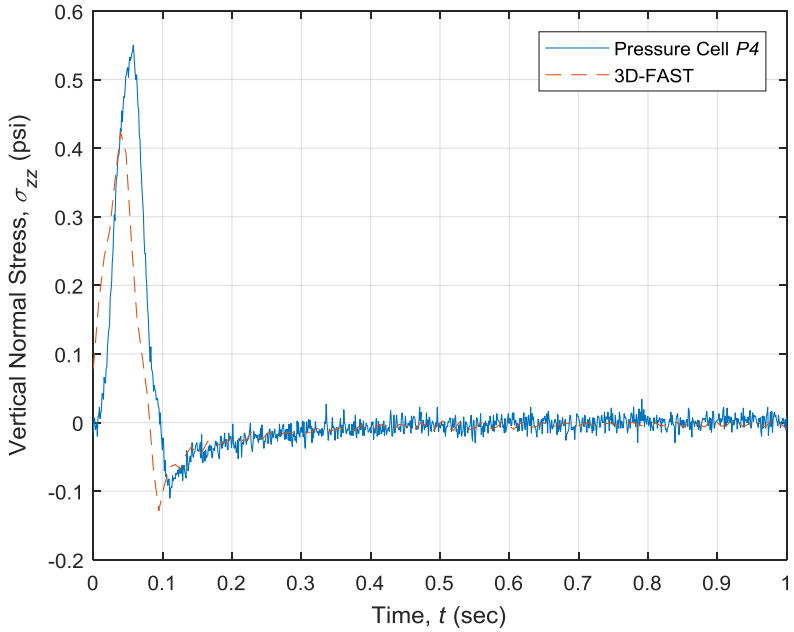

Figure 6.53. Graph. Validation of vertical normal stress at CAB by comparing 3D-FAST results and measured data by pressure cell P4 for one (1) loading pulse at the load level of 9,000 pound.

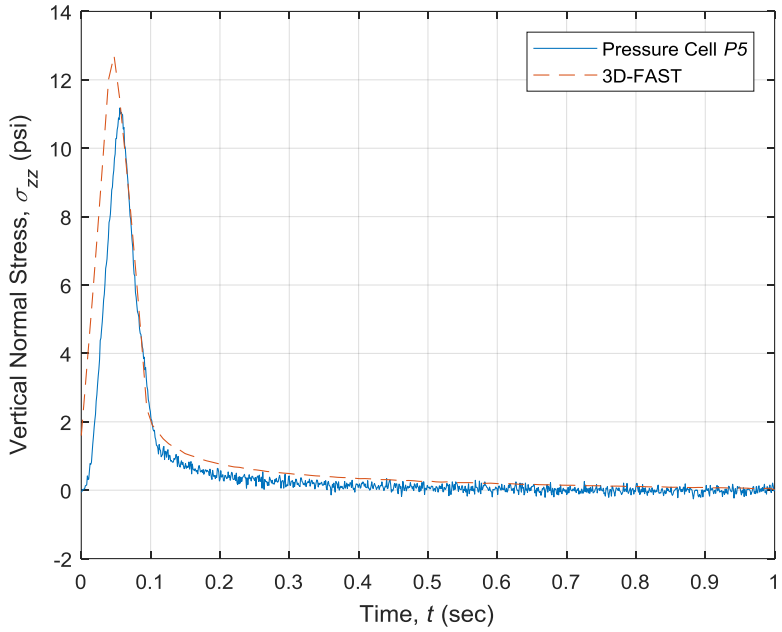

Figure 6.54. Graph. Validation of vertical normal stress at CAB by comparing 3D-FAST results and measured data by pressure cell P5 for one (1) loading pulse at the load level of 9,000 pound.

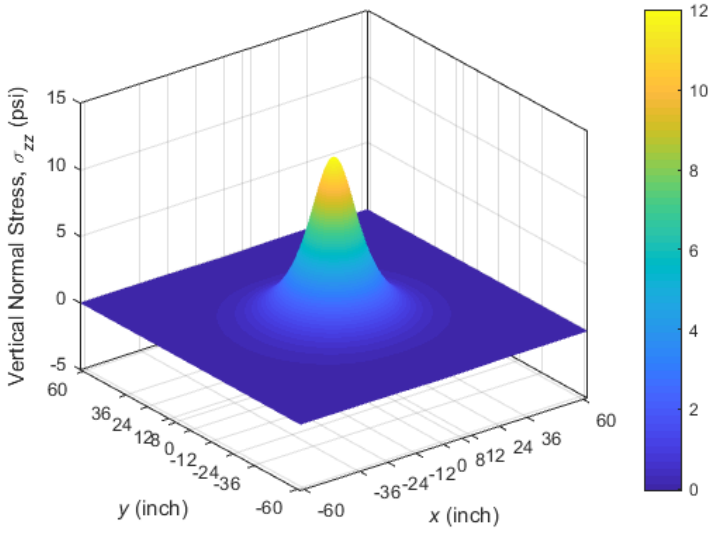

Figure 6.55. Plot. Surface plot (perspective view) for vertical normal stress at mid-depth CAB at time *t* = 0.05 second computed by 3D-FAST.

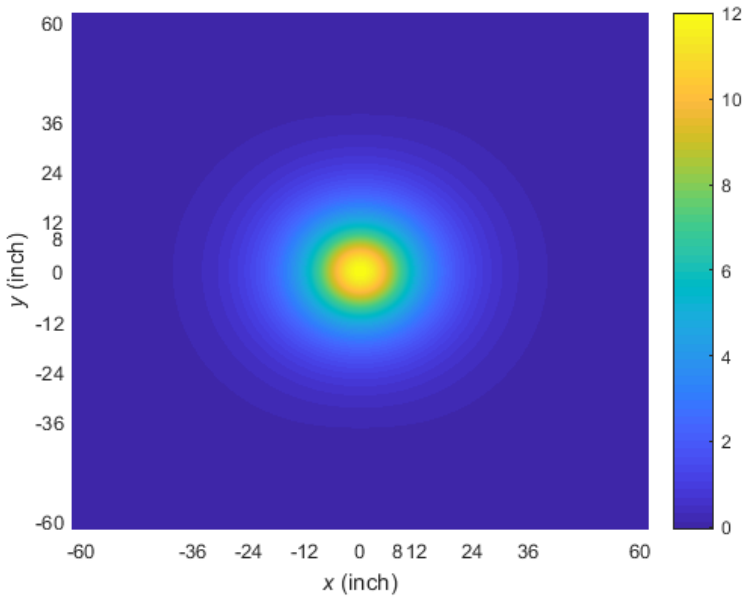

Figure 6.56. Plot. Surface plot (top view) for vertical normal stress at mid-depth CAB at time *t* = 0.05 second computed by 3D-FAST.

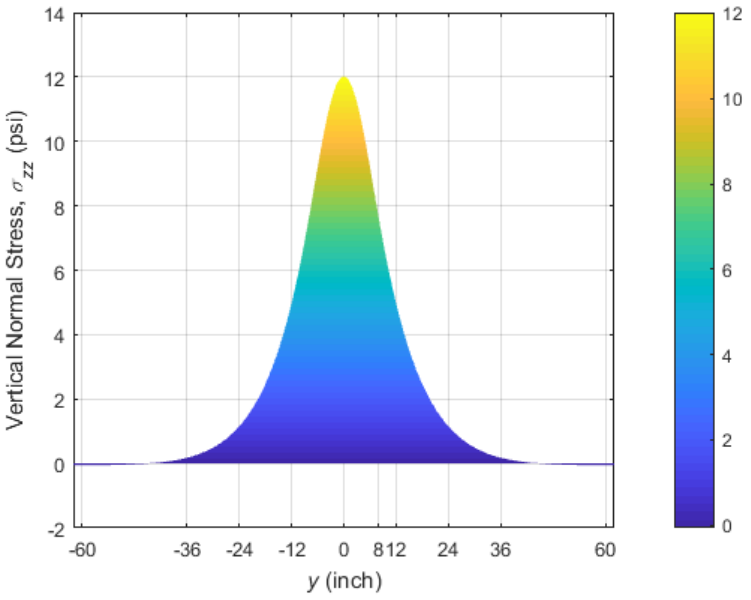

Figure 6.57. Plot. Surface plot (top view) for vertical normal stress at mid-depth CAB at time *t* = 0.05 second computed by 3D-FAST.

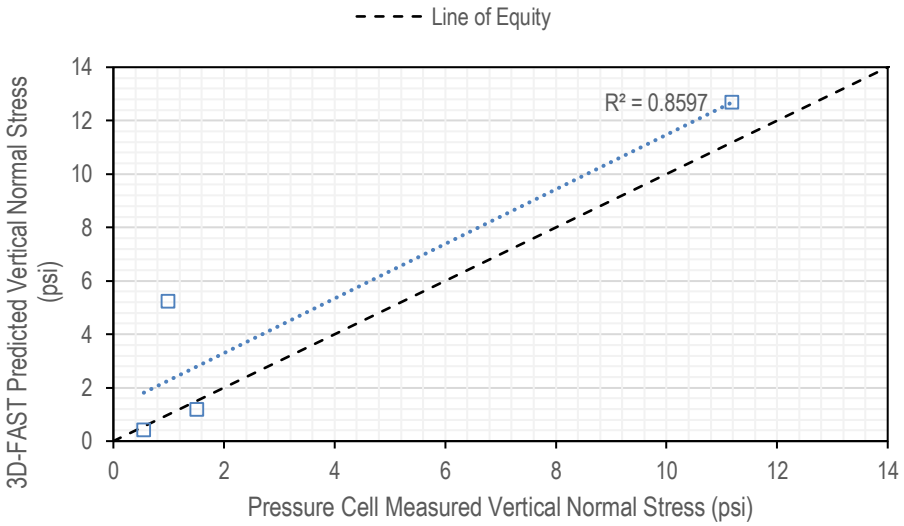

Figure 6.58. Graph. Measured vs. predicted mid-depth CAB vertical normal stress at the load level of 9,000 pound.

At six (6) inch below subgrade surface, again the vertical normal stress measured by pressure cells was used for validating pavement responses obtained by 3D-FAST for SG. Vertical normal stress (σ_{zz}) computed by 3D-FAST was plotted against that of recorded by pressure cells. **Figure 6.59**, **Figure 6.60**, **Figure 6.61**, and **Figure 6.62** present this comparison for pressure cells P6, P7, P9, and P10, respectively. Surface plots for vertical normal stress at six (6) inch below subgrade surface are presented in **Figure 6.69**, **Figure 6.70**, and **Figure 6.71** for perspective, top, and side views, respectively. The results of predicted vertical normal stress computed by 3D-FAST at this depth versus that of measured by pressure cells are presented in **Figure 6.66**.

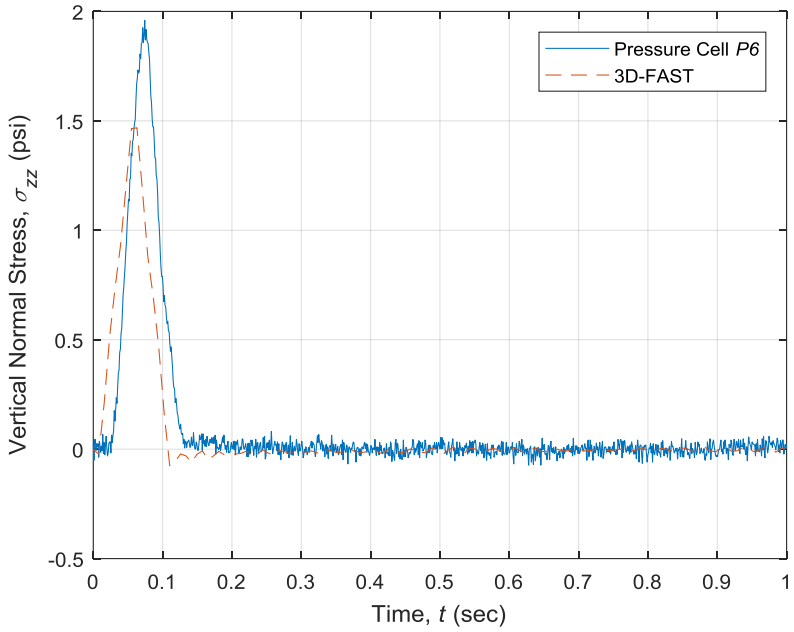

Figure 6.59. Graph. Validation of vertical normal stress at SG by comparing 3D-FAST results and measured data by pressure cell P6 for one (1) loading pulse at the load level of 9,000 pound.

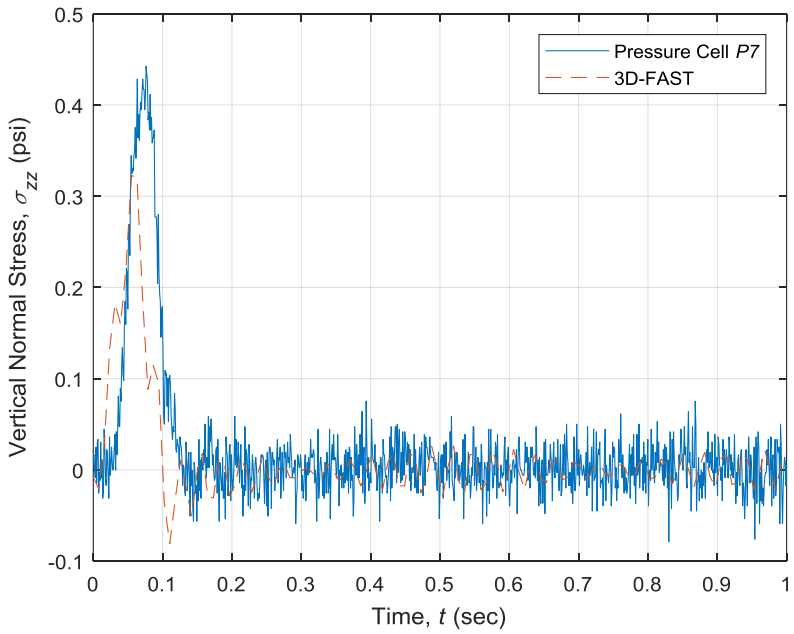

Figure 6.60. Graph. Validation of vertical normal stress at SG by comparing 3D-FAST results and measured data by pressure cell P7 for one (1) loading pulse at the load level of 9,000 pound.

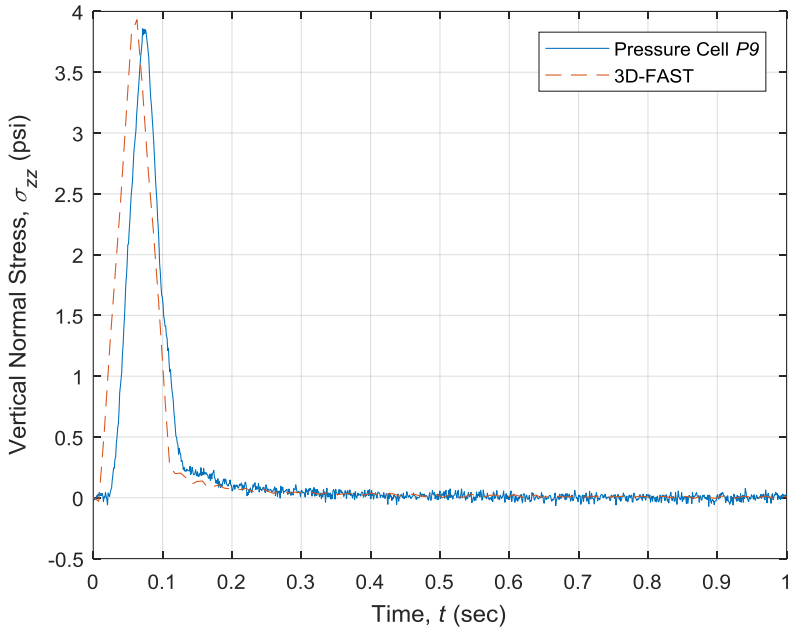

Figure 6.61. Graph. Validation of vertical normal stress at SG by comparing 3D-FAST results and measured data by pressure cell P9 for one (1) loading pulse at the load level of 9,000 pound.

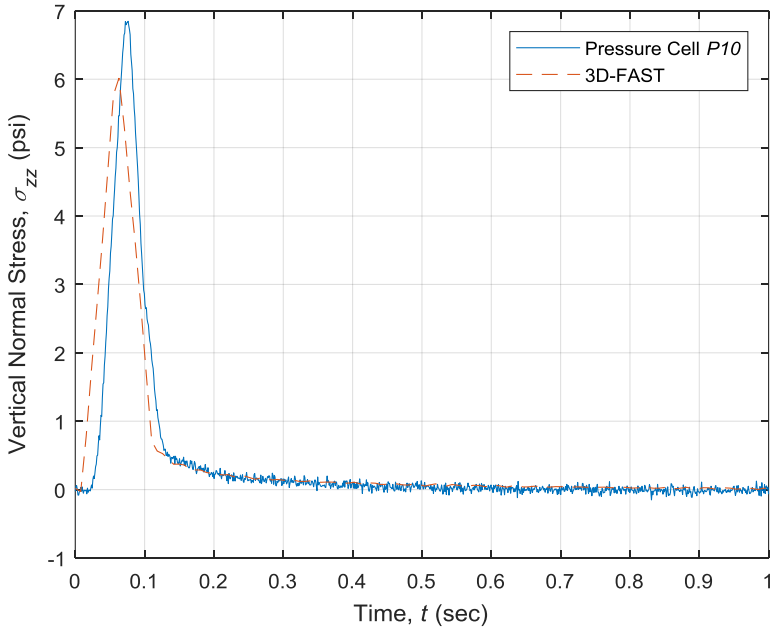

Figure 6.62. Graph. Validation of vertical normal stress at SG by comparing 3D-FAST results and measured data by pressure cell P10 for one (1) loading pulse at the load level of 9,000 pound.

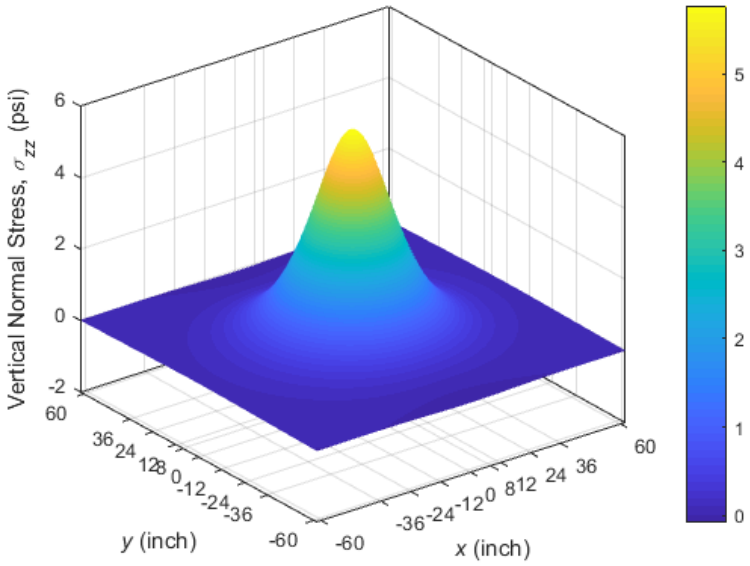

Figure 6.63. Plot. Surface plot (perspective view) for vertical normal stress at six (6) inch below subgrade surface at time *t* = 0.05 second computed by 3D-FAST.

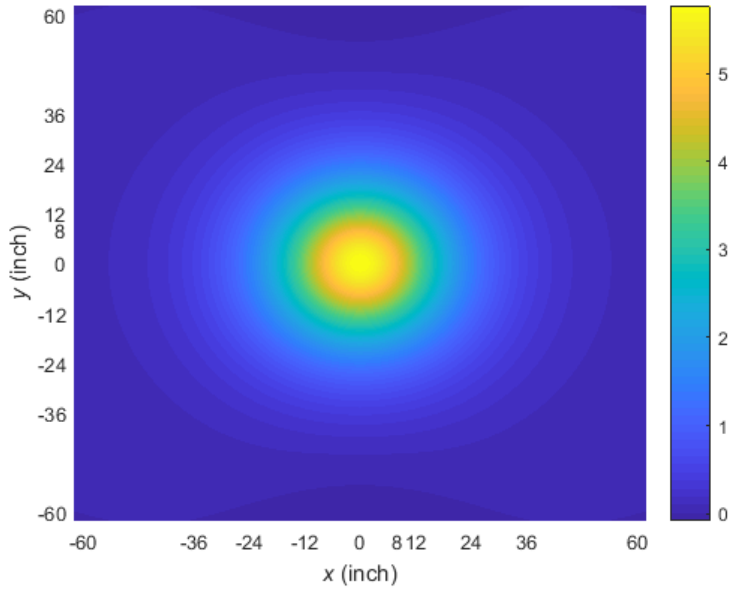

Figure 6.64. Plot. Surface plot (top view) for vertical normal stress at six (6) inch below subgrade surface at time *t* = 0.05 second computed by 3D-FAST.

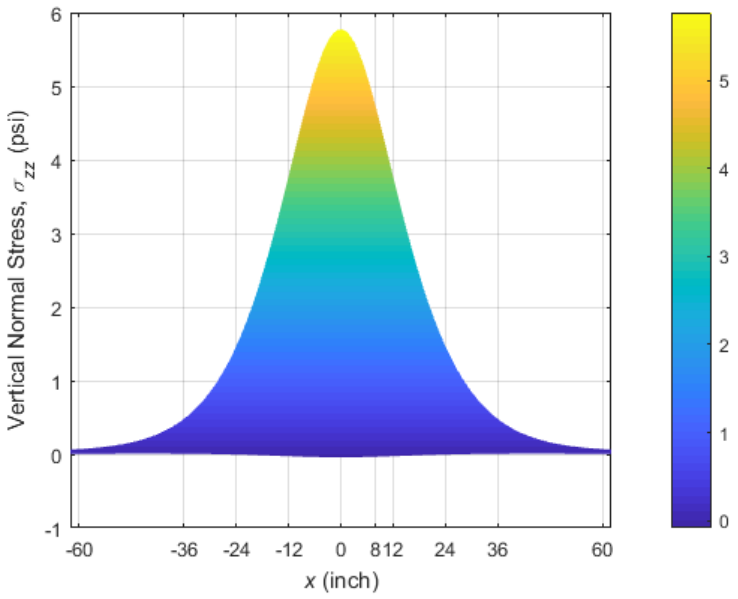

Figure 6.65. Plot. Surface plot (side view) for vertical normal stress at six (6) inch below subgrade surface at time *t* = 0.05 second computed by 3D-FAST.

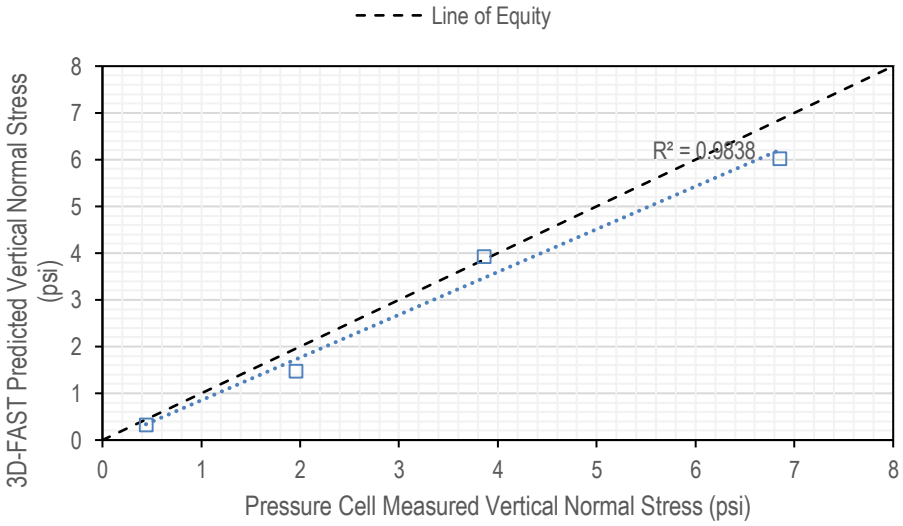

Figure 6.66. Graph. Measured vs. predicted vertical normal stress at six (6) inch below subgrade surface at the load level of 9,000 pound.

6.3.5 Discussion

The results presented for validation in the previous section shows a reliable match between the results computed by 3D-FAST and the results obtained from the instrumentation. LVDTs were placed at the pavement surface at a radial distance of 8, 12, 24, and 36 inch from the load centerline. The LVDT tags were L1, L2, L3, and L4, respectively. The match between 3D-FAST results and recorded instrumentation data was descent. The relative error between 3D-FAST results and LVDT measurement is between -13.9 and 7.3 percent based on the peak values. The pulse shape shows a good agreement between the 3D-FAST results and LVDT measurement. L5, L6, and L7 were not used in the validation.

Vertical normal stress at mid-depth CAB was used as another response type in the validation process. Four (4) pressure cells were placed at a depth of eight (8) inch from the pavement surface, tagged as P2. P3, P4, and P5, and at a radial distance of 12, 24, 36, and 0 inch, respectively, from the load centerline. There is a high level of agreement between 3D-FAST results and instrumentation data for response points at which P3, P4, and P5 are placed. However, data recorded by P2 does not seem to be correct, primarily because the stress recorded by P2 is less than that of P3, although P2 is closer to the load. Thus, it was concluded that P2 should not be considered in the validation process due to potential technical issues. Ignoring P2, the relative error between 3D-FAST results and pressure cell measurements is between -23.6 and 13.6 percent based on the peak values.

At a location of six (6) inch below subgrade surface, which is at a depth of 17 inch from pavement surface, Five (5) pressure cells were used, tagged as P6, P7, P9, and

P5, at radial distances of 24, 48, 12, and 0 inch from centerline of the load, respectively. Pressure cell tagged as P8 was not considered in the analysis because recorded data was very noisy. The relative error between 3D-FAST results and pressure cell measurements is between -27.3 and 1.8 percent based on the peak values noting that there is a phase shift between the two sets of predicted and measured data.

6.3.6 Parallel Processing

As previously described in 3D-FAST unique computational features (**Chapter 5**), parallel processing is a means of reducing model runtime in order to make it more efficient, without losing accuracy whatsoever. Since 3D-FAST was implemented in MATLAB, the MATLAB Parallel Computing Toolbox was used for incorporating parallel processing into 3D-FAST. The processing units in this toolbox are called *workers*. The 3D-FAST runtime is presented in **Table 6.18** using an Intel ® Core i7-4770 3.40 GHz processor with four (4) local processors (workers). This table presents the runtime when one (1), two (2), three (3), or four (4) processors are involved. Furthermore, speed-up factor and parallel efficiency are presented in this table, which are calculated by using the equations presented in **Figure 5.2** and **Figure 5.3**, respectively.

Table 6.18. 3D-FAST Runtime for Modeling Box Experiment No. 3 Using Parallel Processing.

Number of Processors, *n*	Runtime, *T*(n) (sec)	Speed-up Factor, *S(n)*	Parallel Efficiency, *E(n)*
One (1)	10,661	1.000	100.0%
Two (2)	6,430	1.658	82.9%
Three (3)	5,107	2.088	69.6%
Four (4)	4,489	2.375	59.4%

As can be seen in this table, the runtime decreased substantially by adding additional processing units, and subsequently the speed-up factor increased. The parallel efficiency is less than 100% as parallel processing is used (i.e., $n > 1$) and decreases with increasing number of processing units. Thus, 3D-FAST algorithm in not fully parallelizable, which was expected. The portion of algorithm that is serial (B in the equation presented in **Figure 5.4**) and the portion that is parallelizable (i.e., 1 - B) are presented in **Table 6.19** using the Amdahl's law (equation presented in **Figure 5.5**) if parallel processing is employed. Based on this figure, on average, the serial portion of 3D-FAST algorithm is $B = 0.218$. Amdahl's law can be used to predict 3D-FAST runtime if additional processing units are used. This prediction is conducted for up to ten (10) processing units, which is presented in **Table 6.20**. 3D-FAST runtime as a function of number of processing units is presented in **Figure 6.67**.

Table 6.19. Serial and Non-Serial Portions of 3D-FAST Modeling Algorithm.

Number of Processors, *n*	Serial Portion of Algorithm, *B*	Non-Serial (Parallelizable) Portion of the Algorithm, 1 - *B*
Two (2)	0.206	0.794
Three (3)	0.219	0.781
Four (4)	0.228	0.772

Table 6.20. Prediction of 3D-FAST Runtime Using Additional Processing Units.

Number of Processors, *n*	Predicted Runtime, *T*(n) (sec)	Speed-up Factor, *S(n)*	Parallel Efficiency, *E(n)*
Five (5)	3,988	2.673	53.5%
Six (6)	3,710	2.873	47.9%
Seven (7)	3,512	3.036	43.4%
Eight (8)	3,363	3.170	39.6%
Nine (9)	3,247	3.283	36.5%
Ten (10)	3,154	3.380	33.8%

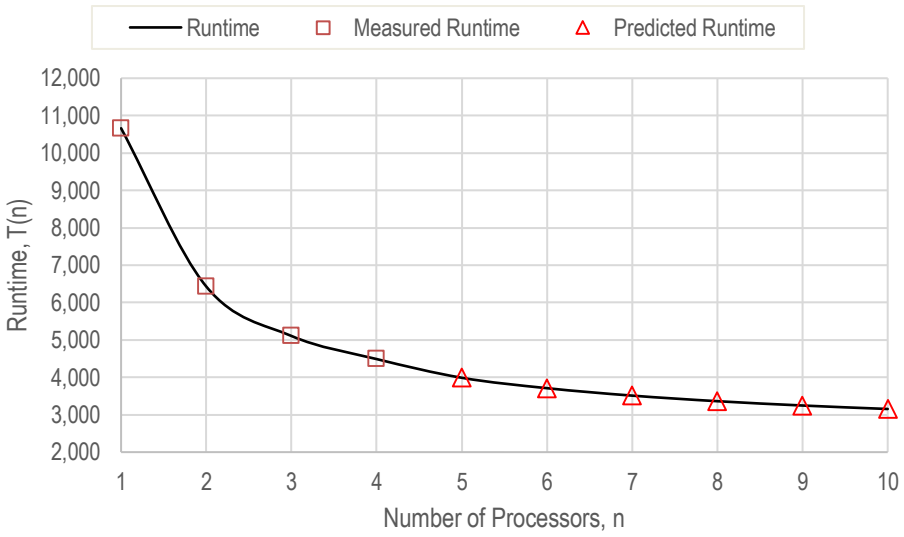

Figure 6.67. Graph. 3D-FAST runtime for different number of involved processing units using parallel processing.

6.4 3D-FAST Application: Roughness-Induced Dynamic Loading

In the previous sections, 3D-FAST verification and validation were carried out through using rheological models and measured data from the Box experiment no. 3, respectively. In the current section, analysis of a pavement system experiencing roughness-induced dynamic vehicle loading is presented as an application of 3D-FAST. After explaining the road roughness and surface irregularities, the quarter-car simulation (QCS) technique is presented to obtain vehicle dynamic loading. In the next step, the results of the simulation is used as the load input for 3D-FAST, and select pavement responses are presented for a typical pavement structure.

6.4.1 Road Roughness

In order to estimate pavement responses reliably, the dynamic loads induced by vehicles operating on a highway should be realistically identified. In the ideal case of an absolutely smooth road with no roughness, the traffic load would be equal to the vehicle static load. In reality, however, there is always a certain amount of roughness which induces dynamic load (i.e. load that varies with time) (S.-F. Kazemi, Sebaaly, et al., 2017). Road roughness is the deviation of pavement surface from a reference plate. Roughness-induced vehicle dynamic loads, as well as other types of dynamic loads, typically leads to higher pavement deformation compared to static loads (Shahin, 1994). Therefore, more rutting and damage are anticipated as the level of road roughness increases. From a pavement design prospective, variation in traffic load adversely affects the pavement service life, and causes noise and vibration (Hesami, Ahmadi, & Ghalesari, 2016; Lak, Degrande, & Lombaert, 2011).

International Road Roughness (IRI) is the most common measure for road roughness (Yang, Chen, & Li, 2015). To obtain IRI, the longitudinal road profile should be surveyed (e.g., by using a profilometer). The wavelengths in pavement longitudinal profile corresponding to road roughness is in the range of 10.0 m to 100.0 m while wavelengths smaller than 10.0 m and wavelengths larger than 100.0 m correspond to texture and topography, respectively (Andren, 2005). One approach to account for longitudinal profile is generating a random road profile. A random road profile can be generated based on ISO 8608, which considers a power function for Power Spectral Density (PSD) of the road profile (ISO, 1995). Details about generating random profile

can be found elsewhere (Sun, 2013; Tyan, Hong, Tu, & Jeng, 2009). Furthermore, details about generating a two-dimensional road surface is presented by Sun based on Gaussian processes (Sun, 2013). In the current section, an actual road profile surveyed by profilometer is used to obtain dynamic load and consequently pavement responses, rather than an artificial road profile generated randomly. This road profile was obtained from the LTPP (Long Term Pavement Program) database.

The computational capacity has always been a limitation for pavement response analysis models, specifically for models accounting for dynamic loads (e.g., 3D-FAST). The massive amount of calculations significantly increases the runtime, if not making the run impossible due to limitations in the random access memory (RAM). Thus, appropriate assumptions should be considered in order to efficiently use the computational resources. This means that after obtaining the dynamic load for a road section, a window stretch out of the entire section can be selected to be applied in 3D-FAST.

6.4.2 Quarter-Car Simulation (QCS)

Typically, the load applied by a specific vehicle on the pavement depends on the vehicle speed, vehicle characteristics (i.e. suspension type, axle loads, tire properties, etc.), and road roughness (Sun, 2002). The lumped models are widely used to simulate vehicle loading. Some of the well-known lumped models are quarter car model, half car model, and full car model (Mastinu & Plöchl, 2014). In the current section a quarter-car simulation (QCS) is used to calculate IRI and dynamic vehicle loading. A schematic of QCS is illustrated in **Figure 6.68**. QCS can be conducted at any speed, however, IRI is

standardized based on conducting the simulation at 80 km/h (50 mph). A quarter of the car is used in QCS, which consists of one (1) tire (unsprung mass) and quarter of the body (sprung mass). In **Figure 6.68**, mass is denoted by *m* and elevation is denoted by *x*. Additionally, the subscript *s* and *u* refer to unsprung mass and sprung mass, respectively. Therefore, m_s, m_u, x_s, and x_u represent sprung mass, unsprung mass, elevation of sprung mass, and elevation of unsprung mass, respectively. The spring constant and dashpot constant of the sprung mass are represented by k_s and c_s, respectively. It is assumed that there is no damping associated to unsprung mass, and the spring constant representing the tire is denoted by k_t. The road surface profile is denoted by $u(t)$, which is basically the elevation of the road as a function of time (t) as the vehicle travels the road. $u(t)$ is typically obtained by an equipment (e.g., profilometer, accelerometer, etc.) or can be generated using random algorithms. Based on the quarter-car model presented in **Figure 6.68**, this system has two degrees of freedom (DOF). These DOFs are x_s and x_u corresponding to sprung mass and unsprung mass, respectively. A second-order linear system of ordinary differential equations represents QCS as the equation presented in **Figure 6.69** (Chatti & Zaabar, 2012). In this system of differential equations, all the parameters are as previously defined. Furthermore, the dot operator represents derivation with respect to time. For instance, $\ddot{x}_u$ is the acceleration of unsprung mass.

Based on the field measurements of vehicle dynamic loading, there is a descent level of agreement between the roughness-induced dynamic load calculated by quarter-car simulation and field loads (Sun, 2001). There are more sophisticated lumped models such as half-car and full-car models to address a more realistic vehicle response to the

excitations induced by the road profile. However, quarter vehicle simulation provides an acceptable approximation of the full-car model (Mastinu & Plöchl, 2014).

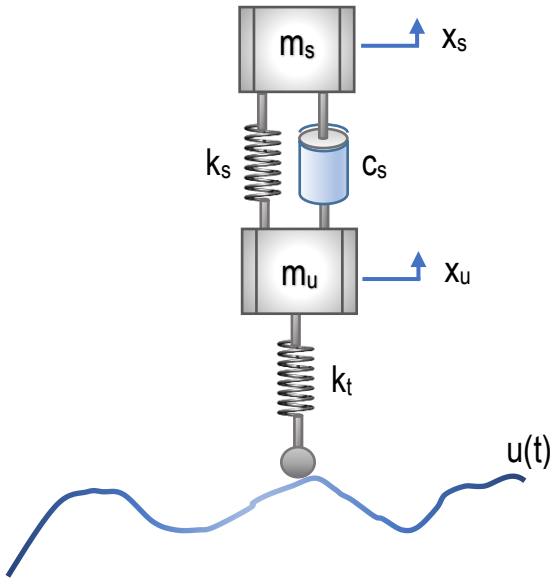

Figure 6.68. Illustration. Schematic of quarter-car simulation.

$$\begin{cases} m_u\ddot{x}_u - c_s(\dot{x}_s - \dot{x}_u) + k_t(x_u - u(\quad)) = 0 \\ m_s\ddot{x}_s + c_s(\dot{x}_s - \dot{x}_u) + k_s(x_s - x_u) = 0 \end{cases}$$

Figure 6.69. Equation. The system of differential equations corresponding to quarter-car simulation.

Based on the system of ODEs presented in **Figure 6.69**, the quarter-car model responds to the excitation caused by the road surface irregularities depending on the simulation parameters (i.e. spring and dashpot constants), road roughness, and vehicle speed. By solving this system of ODEs, displacement, velocity, and acceleration can be

obtained for sprung and unsprung masses. Sayers suggested using QCS at a constant speed of 80 km/h (22.22 m/s) to obtain IRI (Sayers, 1995). The procedure was widely accepted and has been standardized as ASTM E1926 (ASTM, 2015). IRI is the average of the absolute relative velocity between sprung mass and unsprung mass over the length of the traversed pavement section, which is obtained by the equation presented in **Figure 6.70**.

$$IRI = \frac{1}{L}\int_0^T (\dot{x}_s - \dot{x}_u)dt = \frac{1}{V \cdot N \cdot \Delta t}\sum_{i=0}^{N}|\dot{x}_s - \dot{x}_u|\,\Delta t = \frac{1}{V \cdot N}\sum_{i=0}^{N}|\dot{x}_s - \dot{x}_u|$$

Figure 6.70. Equation. International Roughness Index (IRI) formula.

In this equation, *IRI*, *L*, *T*, *N*, *V*, and Δt are International Roughness Index, length of traversed pavement section, total time to traverse pavement section at speed *V*, number of surveyed points, survey velocity (80 km/h for the sake of quarter-car simulation), and time interval between surveying two consequent points, respectively. Other parameters are as previously defined (see **Figure 6.68** and **Figure 6.69**). The common units for IRI are m/km or inch/mile (1 m/km = 63.36 inch/mile). The equation presented in **Figure 6.70** yields to no units for IRI. Therefore, one needs to multiply the result of this equation by 1,000 in order to obtain the IRI in m/km, or by 63,360 to convert it to inch/mile.

The mechanical parameters for the quarter-car model used in IRI calculations are presented in **Table 6.21** (Sayers, 1995). For simplicity, these parameters are normalized

with respect to the sprung mass (m_s). The quarter-car model associated with these model parameters is so-called *Golden Car*.

Table 6.21. Model Parameters for Quarter-Car Simulation (Golden Car).

Parameter	Value
$c = c_s/m_s$	6.0
$k_1 = k_t/m_s$	653
$k_2 = k_s/m_s$	63.3
$\mu = m_u/m_s$	0.15

In order to implement QCS, a Simulink model was developed based on the system of ODEs presented in **Figure 6.69**. This model is graphically demonstrated in **Figure 6.71**. This Simulink model basically solves that system of differential corresponding to QCS by employing numerical approaches (e.g., Runge-Kutta method). The model is integrated with a MATLAB® script to input road profile, vehicle speed, and quarter-car mechanical properties (see **Table 6.21**). The model results can be displayed using the *Scope* element in Simulink. Sample results of using the developed Simulink model are presented in **Figure 6.72**. In this figure, there are three (3) graphs. From top to bottom, these graphs show the elevation of road, sprung mass (i.e., quarter of the body), and unsprung mass (i.e., the tire) as a function of distance (or time) traveled by the vehicle. As can be seen in this figure, while the road surface has a considerable amount of irregularities, the vehicle body (unsprung mass) experiences much less vibration due to vehicle suspension system.

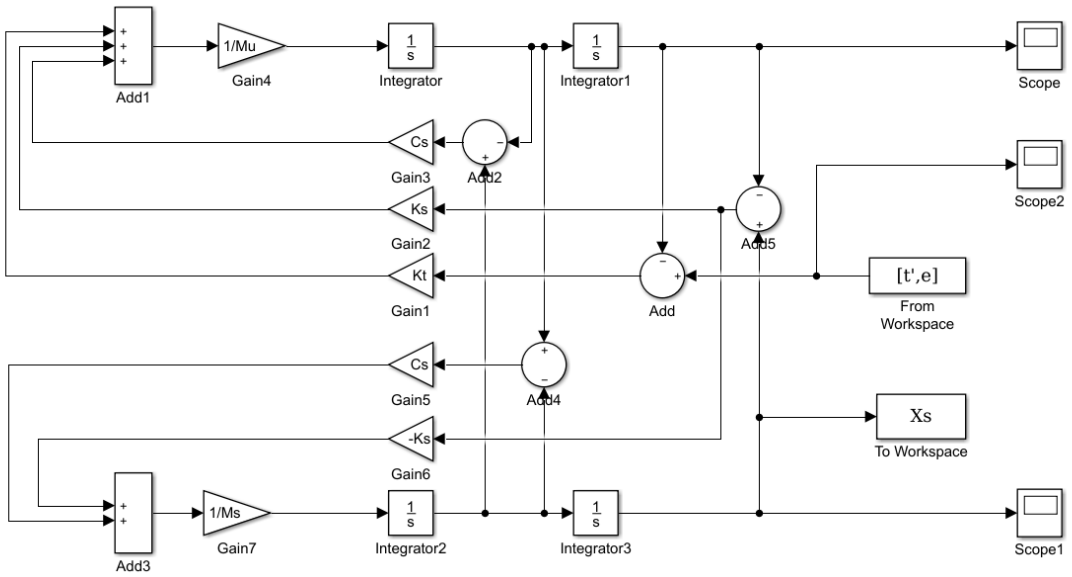

Figure 6.71. Illustration. Simulink model developed for quarter-car simulation.

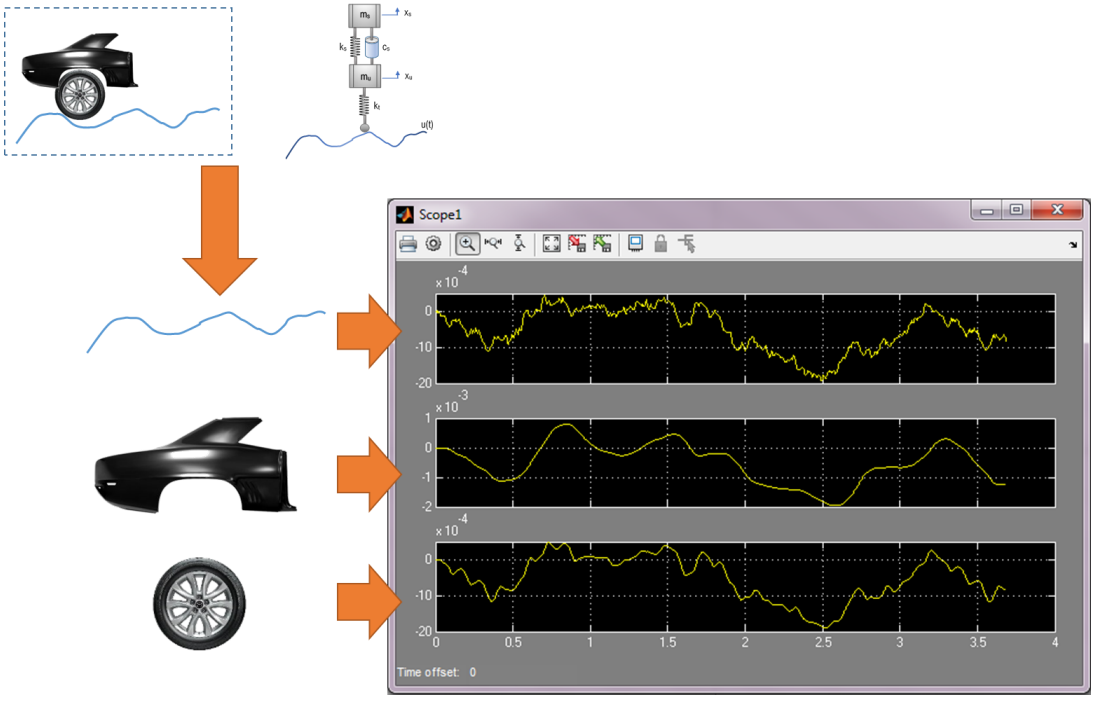

Figure 6.72. Photo. QCS results for a sample road profile using the developed Simulink model.

6.4.3 Selected Road Profile

A road profile was retrieved from the LTPP database to be used in estimating the pavement responses due to road roughness. This profile belongs to the LTPP section 32-1020 located in Nevada, Reno area and is shown in **Figure 6.73**. The solution for QCS is presented in **Figure 6.74**, which is basically the elevation of sprung and unsprung masses, as well as the road surface elevation. The simulation was conducted at a vehicle speed of 80 km/h. The roughness-induced dynamic load is presented in **Figure 6.81**. Details about the road section and roughness-induced dynamic loading are presented in **Table 6.22** and **Table 6.23**, respectively.

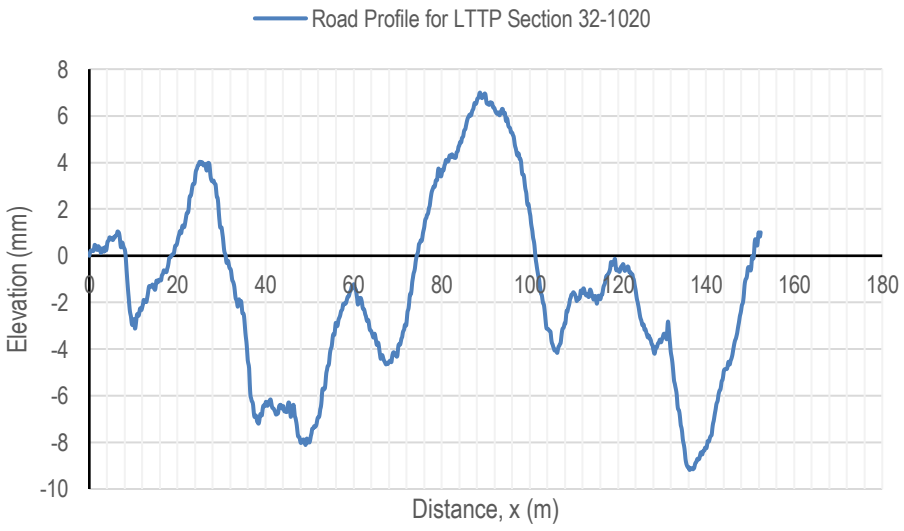

Figure 6.73. Graph. Road profile for LTPP section 32-1020 located in Nevada.

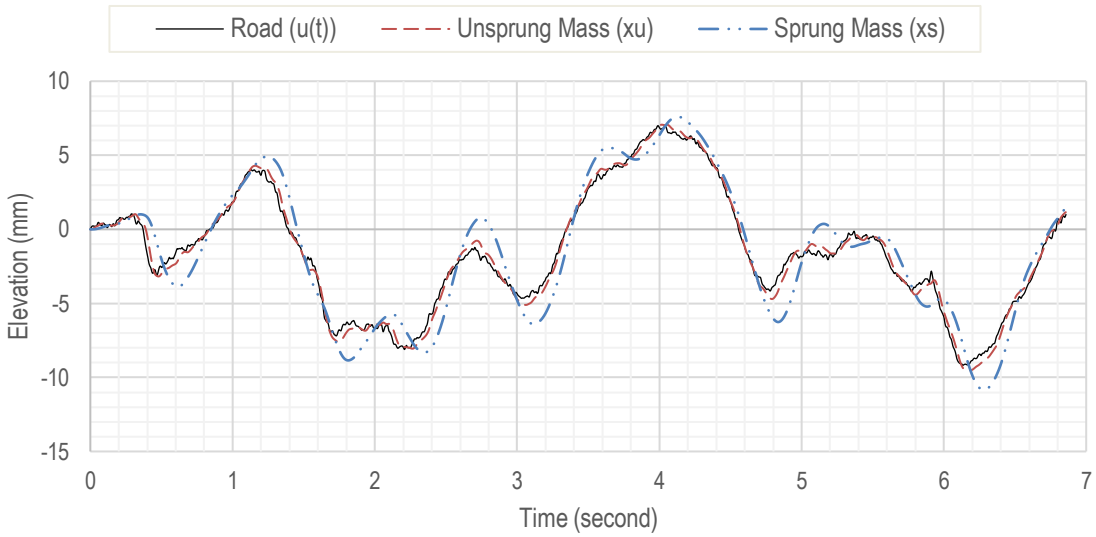

Figure 6.74. Graph. Solution for QCS for the selected road profile located in Nevada.

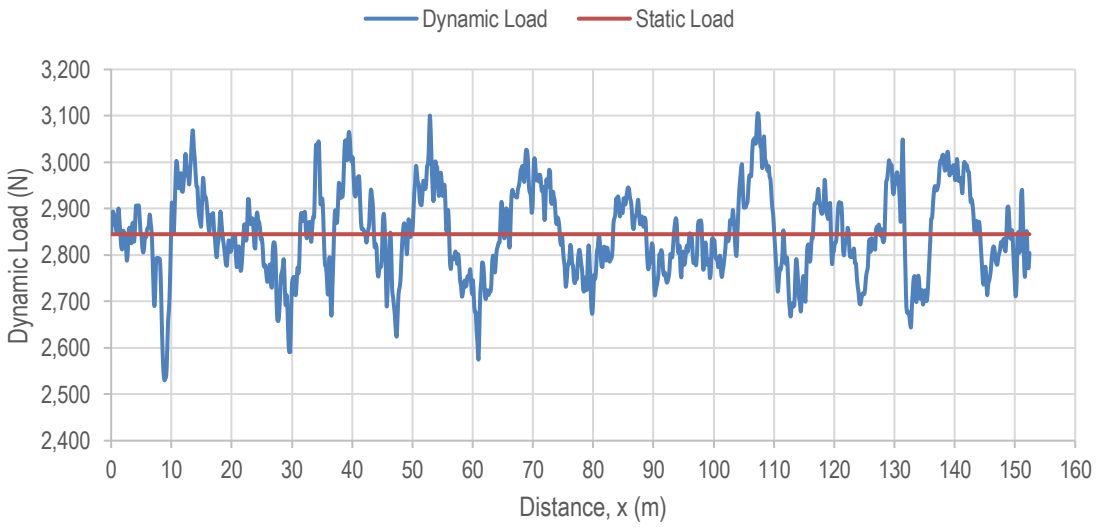

Figure 6.75. Graph. Roughness-induced dynamic load for the road section of interest.

Table 6.22. Details about the Road Profile.

Parameter	Value
LTPP Section SHRP ID	32-1020
Location	Nevada, Reno Area
GPS- Latitude, Longitude (Degrees)	38.53352, -118.61907
Route Direction	State-0362, South Bound
Number of Lanes	1
Climatic Zone	Dry, Non-Freeze
Section Length (m)	152.4
Surveying Frequency Interval (m)	0.1524
Highway Type	Rural Principal Arterial
Pavement Structure	0.175 m AC 0.120 m Unbound (Granular) Base Untreated Subgrade

Table 6.23. Details about the Roughness-Induced Dynamic Loading.

Parameter	Value
Vehicle Speed	80 km/h (22.22 m/s)
Static Load	2844.9 N
Maximum Dynamic Load	3105.4 N
Minimum Dynamic Load	2530.5 N
Average Dynamic Load	2845.8 N
IRI (m/km)	0.741 m/km
Dynamic Load Coefficient (DLC)	3.13 %

6.4.4 3D-FAST Inputs

The inputs used in 3D-FAST runs include pavement surface loading, pavement structure, and material characteristics. The pavement surface loading is as presented in **Figure 6.75**, however, since modeling the entire road profile shown in this figure is not computationally feasible, a stretch of 4.88 m (between x_1 = 0.00 m and x_2 = 4.88 m; see **Figure 6.73**) was modeled in 3D-FAST. The dynamic load is presented in **Figure 6.76** along with load sampling considering K = 128 number of waves in the time domain to

represent the load. A constant uniform tire pressure of 220.0 kPa was considered. The pavement structure and material properties are presented in **Table 6.24**. A master curve was used for AC viscoelastic material characterization according to **Figure 6.37**. The modulus of elasticity for base and subgrade was considered to be 200.0 MPa and 100.0 MPa, respectively.

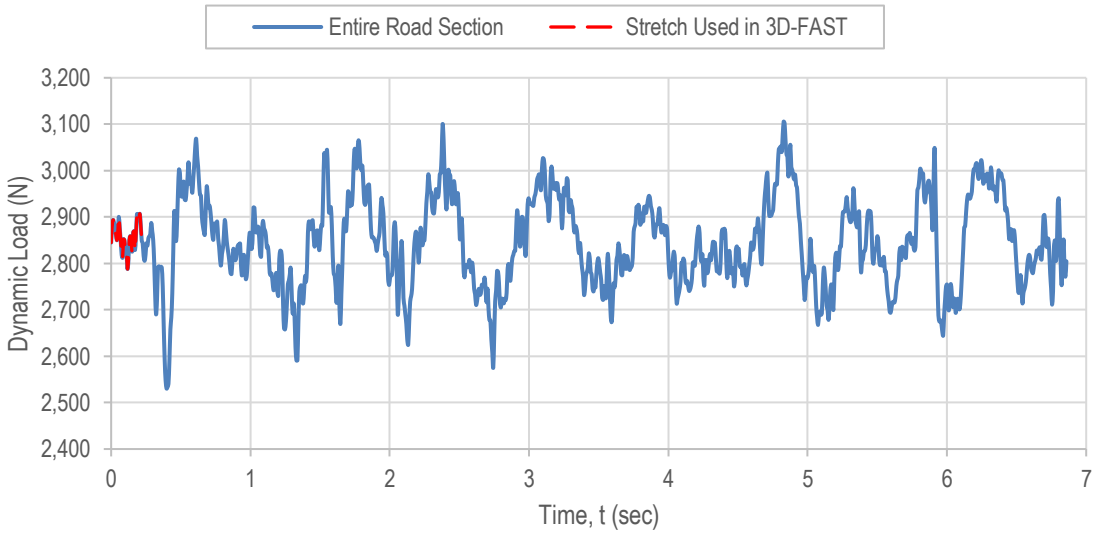

Figure 6.76. Graph. Roughness-induced dynamic load and associated 3D-FAST sampling for a stretch of 19.35 m extracted from the road section.

Table 6.24. Material Characterization and Parameters Needed for 3D-FAST Modeling of Roughness-Induced Dynamic Loading.

Layer Type	Thickness, h (m)	Material Characterization	Poisson's Ratio, ν	Unit Weight, γ (kg/m^3)
Asphalt Concrete (AC)	0.175 m	Viscoelastic	0.30	2,400
Crushed Aggregate Based (CAB)	0.120 m	Elastic	0.35	2,200
Subgrade (SG) Soil	Semi-infinite	Elastic	0.40	2,000

6.4.5 3D-FAST Results

3D-FAST results presented in this section include the following, for response type of interest as a function of time:

- Displacement in the three directions (u_1, u_2, and u_3) at pavement surface, presented in **Figure 6.77**, **Figure 6.78**, and **Figure 6.79**, respectively.
- Horizontal normal stress in the longitudinal and transverse directions (σ_{xx} and σ_{yy}) at pavement surface, presented in **Figure 6.80** and **Figure 6.81**, respectively.
- Horizontal normal strains in the longitudinal and transversedirections (ε_{xx} and ε_{yy}) at mid-depth of AC layer presented in **Figure 6.82** and **Figure 6.83**, respectively.
- Vertical normal strain (ε_{zz}) at the bottom of AC presented in **Figure 6.84**.
- Vertical normal stress (σ_{zz}) on top of subgrade presented in **Figure 6.85**.

Both minimum and maximum values of responses at the desired depth is presented in **Figure 6.77** to **Figure 6.85** as a function of time. The minimum and maximum values of responses for the entire time of analysis are presented in **Table 6.25**. It worth mentioning that in 3D-FAST formulation, the negative and positive values correspond to tension and compression, respectively.

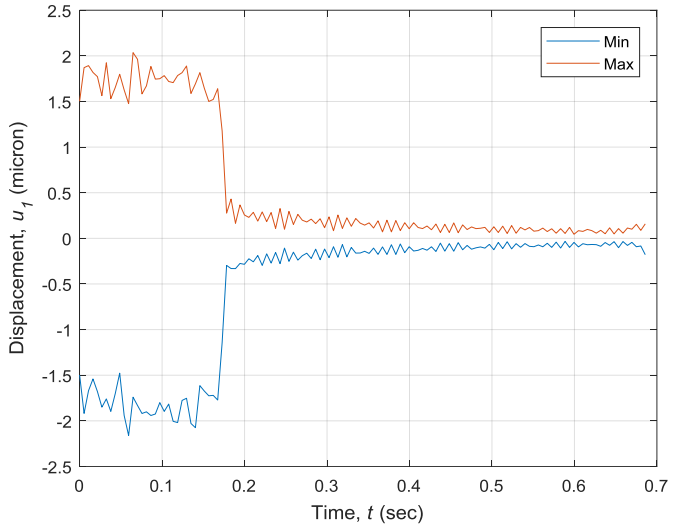

Figure 6.77. Graph. Minimum and maximum longitudinal displacement in *x*-direction (u_1) as a function of time at pavement surface.

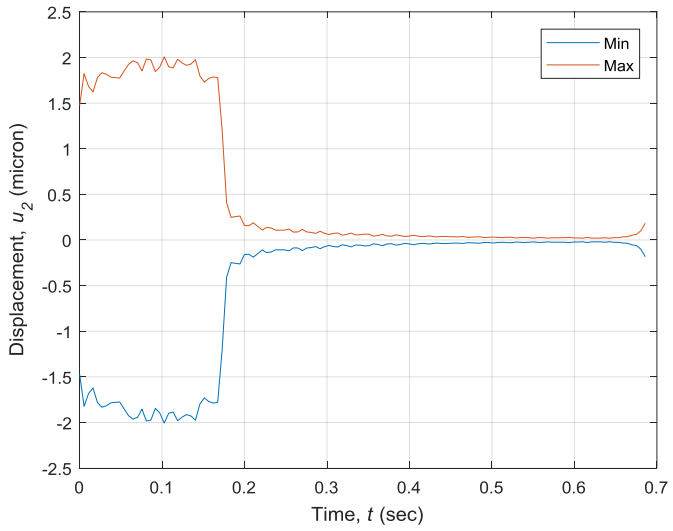

Figure 6.78. Graph. Minimum and maximum transverse displacement in *y*-direction (u_2) as a function of time at pavement surface.

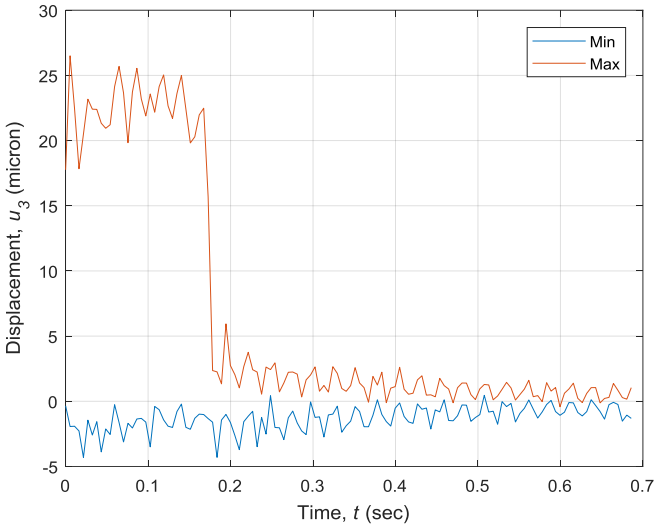

Figure 6.79. Graph. Minimum and maximum vertical displacement in *z*-direction (u_3) as a function of time at pavement surface.

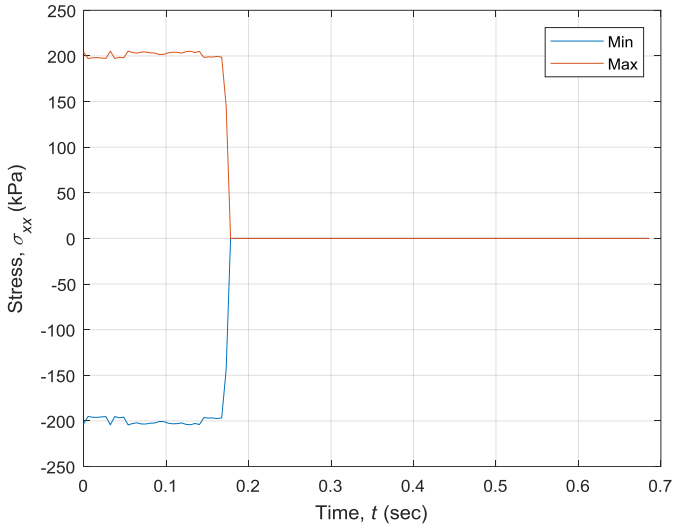

Figure 6.80. Graph. Minimum and maximum longitudinal normal stress in *x*-direction (σ_{xx}) at pavement surface.

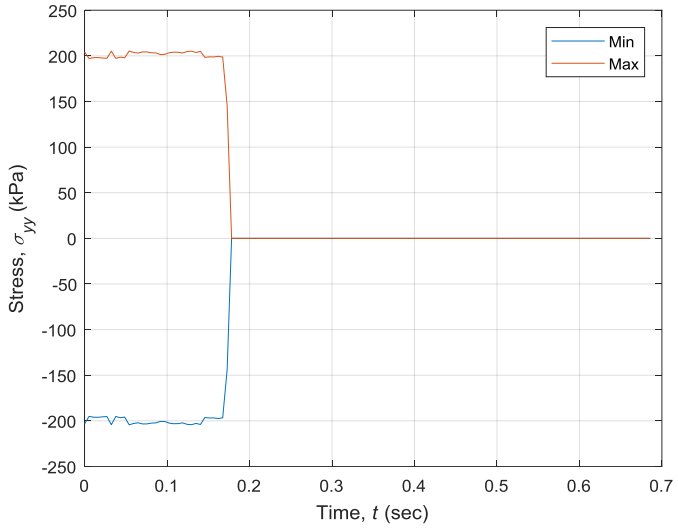

Figure 6.81. Graph. Minimum and maximum transverse normal stress in *y*-direction (σ_{yy}) at pavement surface.

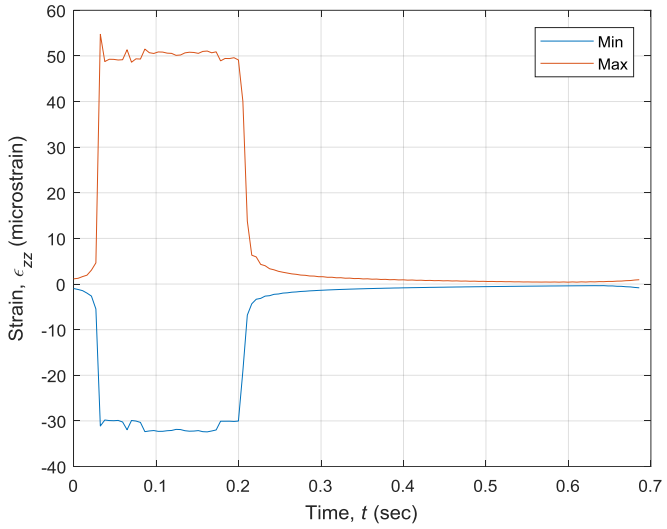

Figure 6.82. Graph. Minimum and maximum vertical normal strain (ε_{zz}) at mid-depth of AC.

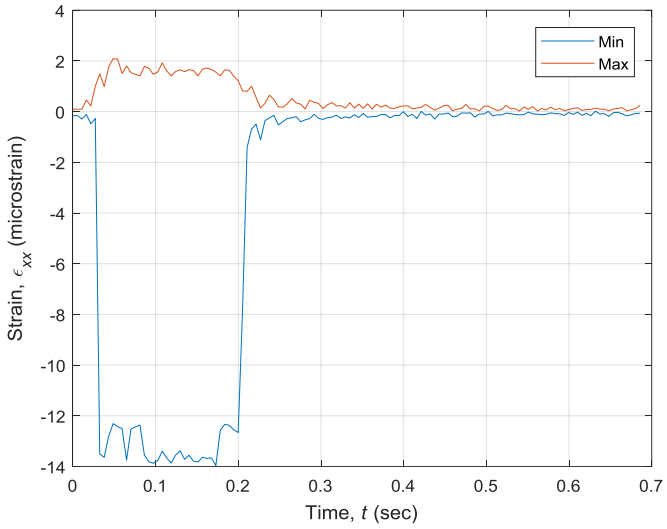

Figure 6.83. Graph. Minimum and maximum longitudinal normal strain in *x*-direction (ε_{xx}) at the bottom of AC.

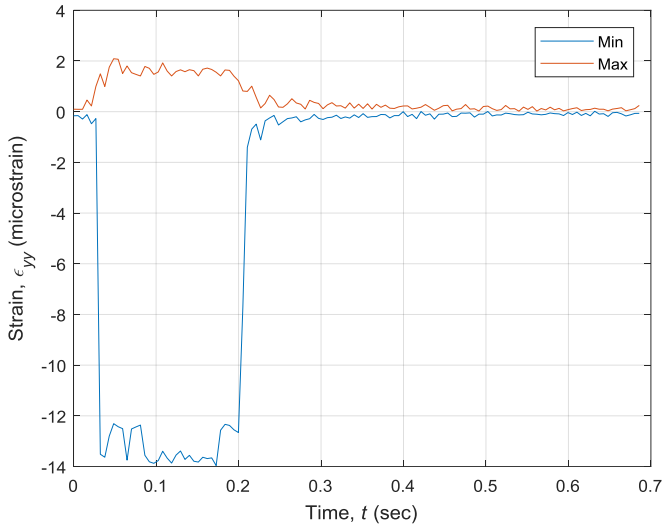

Figure 6.84. Graph. Minimum and maximum transverse normal strain in *y*-direction (ε_{yy}) at the bottom of AC.

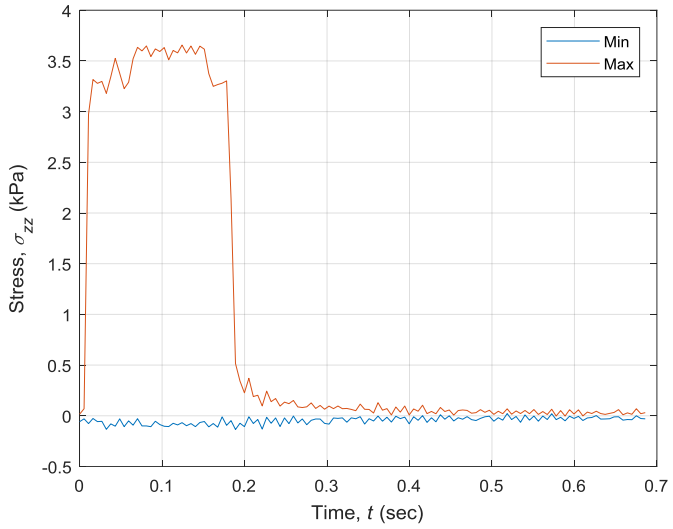

Figure 6.85. Graph. Minimum and maximum vertical normal stress (σ_{zz}) on top of subgrade.

Table 6.25. Minimum and Maximum Responses for Different Response Types at Different Locations for Roughness-Induced Dynamic Load Example.

Response Type	Symbol	Units	Depth from Pavement Surface, z (m)	Layer	Minimum Value	Maximum Value
Horizontal longitudinal displacement	u_1	micron	0 (Pavement Surface)	AC	-2.16	2.04
Horizontal transverse displacement	u_2	micron	0 (Pavement Surface)	AC	-2.01	2.01
Vertical displacement	u_3	micron	0 (Pavement Surface)	AC	-4.30	26.50
Horizontal longitudinal normal stress	σ_{xx}	kPa	0 (Pavement Surface)	AC	-204.3	205.3
Horizontal transverse normal stress	σ_{yy}	kPa	0 (Pavement Surface)	AC	-204.4	205.3
Vertical normal strain	ε_{zz}	microstrain	0.0875 (Mid-depth AC)	AC	-32.4	54.7
Horizontal longitudinal normal strain	ε_{xx}	microstrain	0.175 (Bottom of AC)	AC	-14.0	2.1
Horizontal longitudinal normal strain	ε_{yy}	microstrain	0.175 (Bottom of AC)	AC	-16.0	2.3
Vertical normal stress	σ_{zz}	kPa	0.295 (Top of SG)	SG	-0.1	3.7

CHAPTER 7 SUMMARY OF FINDINGS, CONCLUSIONS, AND RECOMMENDATIONS

7.1 Summary

In this study, a finite-layer model called *3D-FAST* was developed for estimating pavement mechanical responses (i.e., stresses, strains, and displacements). 3D-FAST stands for ***3-D***imensional ***F***ourier ***A***nalysis of pavement ***S***tructures under ***T***ransient loading. According to this acronym, 3D-FAST is a model to accurately analyze pavement structures under dynamic (transient) loading. The model is mathematically sophisticated and uses three-dimensional (3-D) Fourier transform so that all the respective calculations are conducted in the frequency domain.

3D-FAST is a finite-layer model which considers each layer as a separate element. The finite-layer has outstanding advantages compared to the common finite-element model. These advantages were comprehensively described in **Chapter 2**. For instance, with finite-layer method there is no concern with respect to meshing pavement structure, while meshing is a critical aspect of finite-layer method. Furthermore, finite-layer decomposes the load (e.g., stationary, dynamic, etc.) into a number of waves traveling in different domains (e.g., spatial and time domains), which incorporates considerable flexibility into the model. For instance, parallel processing can be used to accelerate the runtime. With finite-element method, most of the solving process is based on iteration schemes, thus such a flexibility does not exist.

3D-FAST does not have most of the limitations existing in many currently available models and software packages for analyzing pavement structures. The surface loading can be non-uniform and/or non-circular in 3D-FAST, because it uses Fourier transform rather than Hankel or Hankel-Laplace transform. In addition, there is no limitation (e.g., symmetry) with the dynamic load in 3D-FAST, and the shape of the load (e.g., vehicle tire load) can completely change from one time step to the next. Therefore, the load applied at the pavement surface does not have to necessarily operate at constant speed. One unique feature associated with 3D-FAST is that shear in both forms of longitudinal and transverse can be modeled, which does not have to be necessarily symmetric. Furthermore, surface shear loads can be also dynamic (i.e., varying with time). Another important aspect of 3D-FAST is that it is capable of viscoelastic material characterization by using a dynamic modulus master curve or rheological models. Viscoelastic material characterization has become available in 3D-FAST, because waves traveling at different velocities in the time domain will excite the viscoelastic material with different dynamic moduli values.

3D-FAST is an extension to its predecessor model: 3D-Move. 3D-Move uses a two-dimensional (2-D) Fourier transform to identify the load because it can only handle loads operating at constant speed. Therefore, the time domain and spatial domain representing the load travel direction are interconnected in 3D-Move. In 3D-FAST, however, this interconnectivity was overlooked and time was introduced as a separate Fourier variable. Therefore, in 3D-FAST the load has to be represented in spatial domains, as well as the domain time, leading to a three-dimensional (3-D) matrix, upon

which the Fast Fourier Transform (FFT) algorithm is applied. The mathematical formulation for 3D-Move and 3D-FAST was presented in **Chapter 3** in **Chapter 4**, respectively.

7.2 3D-FAST Enhancements

3D-FAST and 3D-Move/3D-Move ENHACED have substantial similarities in terms of modeling primarily because 3D-FAST is an extension to 3D-Move. In this study, a number of improvements were made to the original 3D-Move, leading to the genesis of 3D-Move ENHANCED. These improvements were potentially existing in 3D-Move, but were not explored or implemented until recently. Some of these improvements include modeling layer interface debonding, parallel processing, superposition principle, non-uniform Fourier transform, and inverse Fourier transform.

Some of the enhancements made to 3D-FAST are remarkable. These enhancements are primarily due to the finite-layer method and frequency domain calculations. 3D-FAST unique computational features were presented in **Chapter 5** in detail. These enhancement are both in terms of output visualization and model runtime. The inverse fast Fourier transform (IFFT) algorithm was employed to obtain animated surface plots at a certain depth for a specific response type. Parallel processing was successfully incorporated into 3D-FAST noting that the superposition principal allows for this feature. The non-uniform Fourier transform was also introduced as a means of reducing runtime, however, it introduces some approximations to the results.

7.3 3D-FAST Verification, Validation, and Application

In **Chapter 6**, 3D-FAST was verified, validated, and its application was presented through an example. Verification was carried out by comparing 3D-FAST results against the closed-form solutions for strain amplitude and phase angle of common rheological models including Kelvin model, Maxwell model, and Burger model, for a single wave that varies harmonically in the time domain. The mathematical solution for strain amplitude and phase angle of rheological models were derived and compared to 3D-FAST results. 3D-FAST was efficiently verified as this comparison revealed a descent match between 3D-FAST results and closed-form solutions for strain amplitude and phase angle.

3D-FAST validation was performed by comparing the computed results to that of collected by instrumentation for a full-scale test at the University of Nevada, Reno. The instrumented Box experiment no. 3 consisted of a full pavement structure. The recorded instrumentation data for this experiment were used to validate 3D-FAST. In this experiment, a dynamic load was applied on the FWD plate using a hydraulic ram, followed by a rest period. Data measured by LVDTs and pressure cells were used to validate 3D-FAST through comparing measured and predicted pavement displacements and stresses at different layers, and at different depths and radial distances from the load centerline. Same loading was sampled and used in 3D-FAST, and the representative dynamic modulus master curve was used for AC layer. CAB and SG were modeled as linear elastic. Though the experiment was conducted at different load levels, the 9,000 pound load level was used in 3D-FAST validation process. 3D-FAST validation was

considerably successful as the responses computed by 3D-FAST and that of recorded by the LVDTs and pressure cells were matching decently in terms of pulse shape and peak value.

3D-FAST can be applied to a wide range of problems to estimate pavement mechanical responses under dynamic loading, as long as superposition principal is applicable (i.e., linear viscoelastic conditions). In order to demonstrate 3D-FAST application, a pavement system experiencing roughness-induced dynamic loading was structurally analyzed. The pavement surface profile was obtained from LTPP database for a road section in Nevada, Reno area. The roughness-induced dynamic loading was calculated using a quarter-car solution (QCS) model for this road section. The pavement layer and material characteristics were also extracted from LTTP database for the same road section, and were considered as 3D-FAST inputs along with the simulated dynamic loading. 3D-FAST runs were conducted at different depths and for different response types, and the results were presented.

7.4 Conclusions

Some of the conclusions drawn from this study are presented in the following:

- 3D-FAST is a robust numerical model to structurally analyze pavement structures and obtain mechanical responses. 3D-FAST revealed the effectiveness of using finite-layer method for dynamic problems. 3D-FAST is capable of handling dynamic loads (i.e., load that varies with time) with no limitations. Specifically, the load can be of any shape and stress distributions

can be non-uniform and/or non-symmetrical. The surface dynamic shear stresses can also be modeled in 3D-FAST with no requirement for symmetry.

- 3D-FAST is computationally efficient in terms of model runtime. The runtime was further enhanced by employing parallel processing. 3D-FAST is relatively quick compared to its counterpart models. The efficiency of using parallel processing technique was demonstrated through the example used for validation.

- 3D-FAST is capable of viscoelastic material characterization, which is the direct outcome of using frequency domain for associated calculations. Since the top layer of flexible pavements are typically identified as viscoelastic, 3D-FAST can successfully handle the modeling by characterizing this layer properly.

- 3D-FAST was successfully verified by the closed-form solutions of rheological models (Kelvin model, Maxwell model, and Burger model). This verification was performed by comparing 3D-FAST results and closed-form solutions. This comparison was successfully carried out for strain amplitude and phase angle of a single wave with specific frequency of loading time.

- 3D-FAST was effectively validated using a full-scale laboratory experiment. This means that 3D-FAST can be applied to real-world examples including pavement analysis and non-destructive testing, and for a versatile range of applications and dynamic loading protocols.

- The superposition principle represented by Boltzmann's equation can be easily incorporated into 3D-FAST as this equation is in the form of convolution integral. Therefore, the superposition integral simplifies to multiplication in frequency domain. In that case, for a certain depth of a pavement system with the same structure and material characteristics, only one (1) run is needed, and the pavement response can be obtained for any dynamic loading (other than the unit load) by convolving the waves, rather than running 3D-FAST again and again. This feature leads to substantial savings in the runtime.

7.5 Future Enhancements

A number of improvement could be incorporated into 3D-FAST for the future development. First, a stand-alone version of the software can be released for public use. Currently, 3D-FAST is implemented in MATLAB® for both parallel and non-parallel versions. MATLAB® has the Graphical User Interface Development Environment (GUIDE) that allows for developing user-friendly stand-alone applications. GUIDE can be used to produce a stand-alone 3D-FAST software. In the next level, a web-based version of 3D-FAST can be developed so that users can register and create, edit, and save projects.

3D-FAST models the dynamic loading in order to lead to a more realistic pavement modeling. However, this modeling can be further enhanced by using actual tire contact pressure. Since 3D-FAST is capable of handling tire load with non-uniform

contact pressure of any shape (i.e., non-circular), a database of tire contact pressure can be incorporated into the model.

Another potential improvement of 3D-FAST is using it for conducting dynamic backcalculation. Since the backcalculation process is typically an iterative process, using 3D-FAST for this purpose is extremely time-consuming. Therefore, appropriate strategies should be considered to reduce the runtime. Undoubtedly, these strategies must include parallel processing and non-uniform Fourier transform. Furthermore, only waves that significantly contributing to the response of interest (e.g., surface displacement for FWD) should be considered in the backcalculation process to reduce the runtime.

CHAPTER 8 REFERENCES

Abbas, A., Masad, E., Papagiannakis, T., & Harman, T. (2007). Micromechanical modeling of the viscoelastic behavior of asphalt mixtures using the discrete-element method. *International Journal of Geomechanics, 7*(2), 131-139.

Ahlborn, G. (1972). ELSYM5, computer program for determining stresses and deformations in five layer elastic system. *University of California, Berkeley*.

Alavi, M., Pouranian, M., & Hajj, E. (2014). Prediction of asphalt pavement temperature profile with finite control volume method. *Transportation Research Record: Journal of the Transportation Research Board*(2456), 96-106.

Andren, P. (2005). Power spectral density approximations of longitudinal road profiles. *International Journal of Vehicle Design, 40*(1-3), 2-14.

Arabali, P., Sakhaeifar, M. S., Freeman, T. J., Wilson, B. T., & Borowiec, J. D. (2017). Decision-making guideline for preservation of flexible pavements in general aviation airport management. *Journal of Transportation Engineering, Part B: Pavements, 143*(2), 04017006.

Arabzadeh, A., Ceylan, H., Kim, S., Gopalakrishnan, K., & Sassani, A. (2016). Superhydrophobic Coatings on Asphalt Concrete Surfaces: Toward Smart Solutions for Winter Pavement Maintenance. *Transportation Research Record: Journal of the Transportation Research Board*(2551), 10-17.

ARC. (2013). *3D-Move Analysis software (version 2.1)*. Retrieved from

Ashtiani, R. S., Little, D. N., & Rashidi, M. (2018). Neural network based model for estimation of the level of anisotropy of unbound aggregate systems. *Transportation Geotechnics, 15*, 4-12.

ASTM. (2015). Standard Practice for Computing International Roughness Index of Roads from Longitudinal Profile Measurements. In.

Batioja-Alvarez, D., Kazemi, S.-F., Hajj, E. Y., Hand, A. J., & Siddharthan, R. V. Case study for overweight vehicle pavement damage associated costs.

Batioja-Alvarez, D., Kazemi, S.-F., Hajj, E. Y., Siddharthan, R. V., & Hand, A. J. T. (2017). Statistical Distributions of Pavement Damage Associated with Overweight Vehicles: Methodology and Case Study (Accepted for publication). In: Transportation Research Record.

Batioja-Alvarez, D. D., Kazemi, S.-F., Hajj, E. Y., Siddharthan, R. V., & Hand, A. J. (2018). Probabilistic Mechanistic-Based Pavement Damage Costs for Multitrip Overweight Vehicles. *Journal of Transportation Engineering, Part B: Pavements, 144*(2), 04018004.

Bazzaz, M., Darabi, M. K., Little, D. N., & Garg, N. K. (2018). *A Straightforward Procedure to Characterize Nonlinear Viscoelastic Response of Asphalt Concrete at High Temperatures*. Retrieved from

Bozorgzad, A. (2017). Consistent distribution of air voids and asphalt and random orientation of aggregates by flipping specimens during gyratory compaction process. *Construction and Building Materials, 132*, 376-382.

Bozorgzad, A., Kazemi, S.-F., & Moghadas Nejad, F. (2018). Finite-Element Modeling and Laboratory Validation of Evaporation-Induced Moisture Damage to Asphalt

Mixtures. In. 97th Transportation Research Board Annual Meeting: National Academy of Science.

Bozorgzad, A., Kazemi, S.-F., & Nejad, F. M. (2018). Evaporation-induced moisture damage of asphalt mixtures: Microscale model and laboratory validation. *Construction and Building Materials, 171*, 697-707.

Chatti, K., & Zaabar, I. (2012). *Estimating the effects of pavement condition on vehicle operating costs* (Vol. 720): Transportation Research Board.

Coleri, E., & Harvey, J. T. (2011). Evaluation of laboratory, construction, and performance variability by bootstrapping and monte carlo methods for rutting performance prediction of heavy vehicle simulator test sections. *Journal of Transportation Engineering, 137*(12), 897-906.

DAGHIGHI, A., & NAHVI, A. (2014). Effect of different additives on fatigue behavior of asphalt mixtures.

De Jong, D. L., Peutz, M. G. F., & Korswagen, A. R. (1972). *Computer Program, Layered System Under Normal and Tangential Surface Loads: BISAR (bitumen Structures Analysis in Roads)*: The Laboratorium.

El-Desouky, M. (2003). *Further developments of 3DMOVE and its engineering applications.* University of Nevada, Reno,

FHWA. (February 5, 2017). Oversize/Overweight Load Permits.

Hajj, E., Siddharthan, R., Nabizadeh, H., Elfass, S., Nimeri, M., Kazemi, S.-F., . . . Piratheepan, M. (2018). *Analysis Procedures for Evaluating Superheavy Load Movement on Flexible Pavements*. Retrieved from Federal Highway Administration:

Hand, A., & Epps, A. (2000). Effects of test variability on mixture volumetrics and mix design verification. *ASPHALT PAVING TECHNOLOGY, 69*, 635-674.

Harichandran, R. S., Yeh, M.-S., & Baladi, G. Y. (1990). MICH-PAVE: A nonlinear finite element program for the analysis of flexible pavements. In (pp. 123-131). Transportation Research Record.

Hasany, R. M., Shafahi, Y., & Kazemi, S. F. (2013). *A Comprehensive Formulation For Railroad Blocking Problem.* Paper presented at the ECMS.

Hesami, S., Ahmadi, S., & Ghalesari, A. T. (2016). Numerical modeling of train-induced vibration of nearby multi-story building: A case study. *KSCE Journal of Civil Engineering, 20*(5), 1701-1713.

Huang, Y. (1993). KENLAYER computer program. *Pavement Analysis and Design*, 100-167.

Huang, Y. H. (1993). *Pavement analysis and design*.

ISO, I. (1995). Mechanical vibration-Road surface profiles-Reporting of measured data. In: International Organization for Standardization (ISO) Geneva.

Kazemi, S.-F., Hand, A. J., Hajj, E. Y., Sebaaly, P. E., & Siddharthan, R. V. (2017). Modeling Interface Debonding between Asphalt Layers under Dynamic Aircraft Loading. In *Airfield and Highway Pavements 2017* (pp. 71-81).

Kazemi, S.-F., Sebaaly, P. E., Siddharthan, R. V., Hajj, E. Y., Hand, A. J. T., & Ahsanuzzaman , M. (2017). *Dynamic pavement response coefficient to estimate the impact of variation in dynamic vehicle load*. Paper presented at the Tenth International Conference on the Bearing Capacity of Roads, Railways and Airfields, Athens, Greece.

Kazemi, S. F., & Shafahi, Y. (2013). *An Integrated Model Of Parallel Processing And PSO Algorithm For Solving Optimum Highway Alignment Problem.* Paper presented at the ECMS.

Kenis, W. J. (1978). Predictive design procedures, VESYS users manual: An interim design method for flexible pavements using the VESYS structural subsystem. *Final Report Federal Highway Administration, Washington, DC.*

Khodabandehlou, H., & Fadali, M. S. (2017). *A quotient gradient method to train artificial neural networks.* Paper presented at the Neural Networks (IJCNN), 2017 International Joint Conference on.

Khodabandehlou, H., & Fadali, M. S. (2018). Nonlinear System Identification using Neural Networks and Trajectory-Based Optimization. *arXiv preprint arXiv:1804.10346*.

Khodabandehlou, H., Pekcan, G., Fadali, M. S., & Salem, M. (2018). Active neural predictive control of seismically isolated structures. *Structural Control and Health Monitoring, 25*(1).

Lak, M. A., Degrande, G., & Lombaert, G. (2011). The effect of road unevenness on the dynamic vehicle response and ground-borne vibrations due to road traffic. *Soil Dynamics and Earthquake Engineering, 31*(10), 1357-1377.

Lee, H. S. (2014). Viscowave–a new solution for viscoelastic wave propagation of layered structures subjected to an impact load. *International Journal of Pavement Engineering, 15*(6), 542-557.

Maina, J. W., De Beer, M., & Matsui, K. (2007). Effects of layer interface slip on the response and performance of elastic multi-layered flexible airport pavement systems.

Mastinu, G., & Plöchl, M. (2014). *Road and off-road vehicle system dynamics handbook*: CRC Press.

Mokhtari, A., & Nejad, F. M. (2012). Mechanistic approach for fiber and polymer modified SMA mixtures. *Construction and Building Materials, 36*, 381-390.

NCHRP. (2004). *Guide for mechanistic-empirical design of new and rehabilitated pavement structures*. Retrieved from Transportation Research Board of the National Academies, Washington, DC:

Nemati, R., & Dave, E. V. (2017). *Generalized Regression Approach to Develop Predictive Models for Dynamic Modulus and Phase Angle of Asphalt Mixtures*. Retrieved from

Oppenheim, A. V. (1999). *Discrete-time signal processing*: Pearson Education India.

Rauber, T., & Rünger, G. (2013). *Parallel programming: For multicore and cluster systems*: Springer Science & Business Media.

Sayers, M. W. (1995). On the calculation of international roughness index from longitudinal road profile. *Transportation Research Record*(1501).

Shahin, M. Y. (1994). *Pavement management for airports, roads, and parking lots*.

Shames, I. H. (1997). *Elastic and inelastic stress analysis*: CRC Press.

Siddharthan, R., Hajj, E., Sebaaly, P., & Nitharsan, R. (2015). *Formulation and Application of 3D-MOVE: A Dynamic Pavement Analysis Program* Retrieved from Federal Highway Administration:

Siddharthan, R. V., Yao, J., & Sebaaly, P. E. (1998). Pavement strain from moving dynamic 3D load distribution. *Journal of Transportation Engineering, 124*(6), 557-566.

Sun, L. (2001). Computer simulation and field measurement of dynamic pavement loading. *Mathematics and computers in simulation, 56*(3), 297-313.

Sun, L. (2002). Optimum design of "road-friendly" vehicle suspension systems subjected to rough pavement surfaces. *Applied Mathematical Modelling, 26*(5), 635-652.

Sun, L. (2013). An overview of a unified theory of dynamics of vehicle–pavement interaction under moving and stochastic load. *Journal of Modern Transportation, 21*(3), 135-162.

Thompson, M. R. (1982). *ILLI-PAVE Users Manual*: University of Illinois at Urbana-Champaign, Transportation Facilities Group.

Tirado, C., Gamez-Rios, K. Y., Fathi, A., Mazari, M., & Nazarian, S. (2017). Simulation of Lightweight Deflectometer Measurements Considering Nonlinear Behavior of Geomaterials. *Transportation Research Record: Journal of the Transportation Research Board*(2641), 58-65.

Tousi, S. R., & Aznavi, S. (2015). *Performance optimization of a STATCOM based on cascaded multi-level converter topology using multi-objective Genetic Algorithm*. Paper presented at the Electrical Engineering (ICEE), 2015 23rd Iranian Conference on.

Tyan, F., Hong, Y.-F., Tu, S.-H., & Jeng, W. S. (2009). Generation of random road profiles. *Journal of Advanced Engineering, 4*(2), 1373-1378.

Wang, Y., Keshavarzi, B., & Kim, Y. R. (2018). *Fatigue Performance Predictions of Asphalt Pavements Using FlexPAVE with the S-VECD Model and DR Failure Criterion*. Retrieved from

Wardle, L. (1977). *Program CIRCLY: User's Manual*: Commonwealth Scientific and Industrial Research Organization, Division of Applied Geomechanics.

Yang, S., Chen, L., & Li, S. (2015). *Dynamics of vehicle-road coupled system*: Springer.

You, T., Kim, Y.-R., Rami, K. Z., & Little, D. N. (2018). Multiscale Modeling of Asphaltic Pavements: Comparison with Field Performance and Parametric Analysis of Design Variables. *Journal of Transportation Engineering, Part B: Pavements, 144*(2), 04018012.

Zhu, Y., Dave, E. V., Rahbar-Rastegar, R., Daniel, J. S., & Zofka, A. (2017). Comprehensive evaluation of low-temperature fracture indices for asphalt mixtures. *Road Materials and Pavement Design, 18*(sup4), 467-490.